THE EFFECTS OF RESONANTLY ENHANCED FIELDS IN PICOSECOND LASER PRODUCED PLASMAS

by

Shigeaki Uchida

Submitted in Partial Fulfillment

of the

Requirements for the Degree

DOCTOR OF PHILOSOPHY

Supervised by Professor David D. Meyerhofer

Department of Mechanical Engineering

College of Engineering and Applied Science

University of Rochester

Rochester, New York

1992

CURRICULUM VITAE

Shigeaki Uchida was born on April 10, 1959 in Osaka, Japan. He attended Osaka University in 1979 where he received a Bachelor of Science degree in Electrical Engineering and a Master of Science in Electromagnetic Energy Engineering in 1983 and 1985, respectively. From 1986 to 1992 he attended the University of Rochester as a graduate student in the department of mechanical engineering where he was the recipient of an exchange student fellowship from Japanese Ministry of Education and a College Fellowship. After obtaining a Master of Science in May 1989, he was supported by a Research Fellowship of the Laboratory for Laser Energetics (LLE) and performed his thesis research under the supervision of David D. Meyerhofer.

Acknowledgements

I am deeply grateful to my thesis advisor, Professor David Meyerhofer for his insightful suggestions and guidance regarding to the experiments and the interpretation of the data. His continuous encouragement throughout the course of the research is very much appreciated.

I would like to thank Dr. Martin Richardson who initiated the ultra short laser plasma experiments at the LLE. He provided many useful suggestions and encouragement. I would also like to thank Dr. Leonard Goldman and Professor Albert Simon who I owe very much in my early period of graduate study in U of R and research at the LLE.

This project would not have been successful without the support and encouragement from my fellow (former) graduate students. My special thanks go to Dr. Yung-Ho Chuang who improved the laser system to desirable and stable condition, Dr. Steven Augst who coded an excellent data acquisition program and Hong Chen for numerous discussions and help on image data analysis. I appreciate the careful reading of this work by Steve Gutstein. The help and friendship of Justin Peatross, Chris Moore, Brian Buerke and Mark Adams are also greatly appreciated.

I would like to thank Dr. Jaque Delettrez for helpful discussion and simulations, Drs. Tom Boehly, Robert Kremens, Oscar Lopez-Raffo, Samuel Letzring, and Steve Batha for their supports regarding the plasma diagnostics and target chamber apparatus, and Dr. Hyo-gun Kim and the staff of Target Fabrication Laboratory at the LLE for providing high quality targets. I also acknowledge the technical support of Raymond Bahr, Gregory Pien, Charles Hestdalen, Dick Fellows, and G. Raffaele-Addamo and other staff at LLE.

Finally I would like to thank my thesis committee chair-person, Professor Joseph Eberly, for his various comments and suggestion. I would also like to thank the other

members of my thesis committee, Professor Adrian Melissinos and Professor Colin Mckinstrie.

Abstract

Picosecond laser-plasma interactions have been studied experimentally using a 1-ps, 1-μm laser interacting with solid targets. The experiments have been conducted with a detailed knowledge of the laser pulse shape. High intensity contrast laser pulses ensure that no preformed plasma exists before the arrival of the main picosecond pulse in an intensity range where nonlinear processes start to dominate the laser absorption namely from 10^{14} to 10^{16} W/cm^2.

When no preformed plasma exists, the resonantly oscillating field at the critical surface can be significantly enhanced and can accelerate plasma particles to superthermal energies. This field enhancement was studied in terms of the amplitude of p-polarized (laser electric field vector component parallel to the plane of incidence) component through an extensive characterization of the ion blowoff including the ion current, angular distribution, ion charge state as a function of velocity and velocity distribution. Two primary findings from this characterization are: 1) the ion blowoff characteristics depend entirely on the p-polarized component of laser and not on the laser energy, and 2) the nonthermal electrons driving the plasma expansion are highly monoenergetic. These findings are supported by several other plasma diagnostics which include laser energy absorption, continuum and K_α x-ray measurements.

It is suggested from the experimental observation that the electrons are accelerated by the ponderomotive force in the resonantly oscillating field. The intensity enhancement at the critical surface was calculated based on the ponderomotive picture using experimentally measured electron kinetic energy. The experimental values are compared with theoretical values that include plasma-wave dispersion effects on the resonantly oscillating field strength. The ponderomotive acceleration mechanism is compared to wavebreaking as an explanation for the nonthermal electron acceleration.

-

Table of contents

List of figures

Preface

When intense laser pulses (exceeding the breakdown threshold of solids) irradiate solid materials, the absorption of the laser energy creates a system of high temperature ionized matter. This system is called a plasma because the particles in the system respond to external or induced fields collectively depending on the temperature and density. This collective behavior of plasma is the source of a wide range of laser-plasma interaction phenomena such as the excitation of plasma waves and their instabilities, energy transport and hydrodynamic motion. These phenomena have been investigated primarily in the context of laser fusion feasibility research since the late 1960's.[1] Therefore, the interaction time scale at the focus of attention has been from a few tens of picoseconds to a few nanoseconds that is determined by the hydrodynamics of plasmas.

However, the recent development of ultra-short pulse (≤ 1 ps) laser systems [2-5] using techniques such as a chirped pulse amplification and compression (CPAC) [6] has opened the opportunities of studying laser-matter (plasma) interactions with time scales of order of or less than one picosecond. Much interest in studying short-pulse laser-plasma interactions has been driven by the possibility of producing ultra-short x-ray pulses.[7-11] These pulses can be used to study the structure and electronic states of matter with extremely high temporal resolution. These x-rays can also be used as a calibration source for temporal measurements.[7, 9, 12] The interaction of a short laser pulse with a plasma itself provides unique physical conditions such as high temperature solid density material, [13] steep density gradient plasmas, [14, 15] and recombination x-ray lasers [16] from a rapidly cooling plasma. The systematic development of the applications and study of these kinds of plasmas are based on understanding the mechanism of the ultra-short laser-plasma interaction.

Recent investigations have revealed that the absorption of a short-pulse laser is consistent with the Fresnel/Drude models for moderate laser intensities (up to mid 10^{14} W/cm^2). They have also inferred the scale length, $L_n \equiv (\nabla n_e/n_e)^{-1}$, of plasmas using the dependence of absorption on laser incident angle and polarization. On the other hand, the occurrence of non-linear processes at higher intensities, which has been indicated by several authors,[17, 18] remains to be explored. The present work deals with this intensity regime. In particular, it has been found that resonantly enhanced laser electric fields play a significant role in the absorption processes at the critical surface where the electron plasma frequency equals the incident laser frequency. It is shown that the field enhancement is determined by plasma-wave dispersion effects [19, 20] by comparing the experimental results and theoretical calculations. The concomitant high energy electron acceleration by the enhanced ponderomotive force is consistent with the experimental observations presented in this thesis.

This investigation is based on a series of experimental observations of plasmas created by 1-μm, 1-ps laser pulses incident on solid Al planar targets. Since it is desirable to incorporate as many plasma diagnostics as possible to investigate the interaction processes in detail, extensive plasma characterizations have been carried out on laser absorption and the emission of ions, electrons and x-rays. The important results are the measurement of the laser intensity enhancement at the critical surface and the characterization of concomitant high energy electron and ion production. The experimental results are interpreted by a theory that couples electromagnetic wave propagation in a short scale length plasma with resonantly oscillating plasma waves at the critical density. The resulting ponderomotive potential is used to explain the generation of high energy electrons ($\leq$6 keV) and ions ($\leq$100 keV). The picture of ponderomotive acceleration is examined against the conventional wavebreaking mechanism for high energy particle production and found to be consistent with the present experimental conditions.

In studying ultra-short laser interaction, it is very important to control the level of prepulse or satellite emission. Several improvements have been made for the CPAC system in the Laboratory for Laser Energetics to suppress the prepulse to an intensity below 10^{-5} of the main pulse.[21] Having control over the intensity contrast allows comparison of interaction characteristics with and without the existence of preformed plasmas. In the present work, the temporal laser pulse shape is measured with a dynamic range of the five orders of magnitude ensuring that a high contrast 1-ps pulse interacts with solid material. In fact significant changes in interaction characteristics from the low contrast to the high contrast pulse interaction have been observed and particular emphasis is put on the characterization of the high contrast interactions.

The thesis consists of six chapters. An overview of previous work on plasma interactions with short-pulse lasers as well as long pulse lasers is given in chapter I to define and clarify the boundary of the present work in the context of existing work. Chapter II contains a review of theoretical work that is vital to this work such as electromagnetic wave propagation in plasma, laser electric field enhancement at the resonance point (critical surface) and its limiting mechanisms, and an isothermal plasma expansion model on which the ion measurements are based. Experimental procedures and diagnostics are described in chapter III followed by the experimental results in chapter IV. Chapter V covers further discussion of the results and comparison with theoretical models. Finally, chapter VI summarizes the work.

REFERENCES

1   W. Kruer, *The Physics of Laser Plasma Interactions* (Addison-Wesley, Redwood City, 1987).

2   R. L. Fork, C. V. Shank and R. T. Yen, "Amplification of 70-fs optical pulses to gigawatt powers," Appl. Phys. Lett. **41**, 223 (1982).

3   C. Rolland and P. B. Corkum, "Generation of 130-fsec midinfrared pulses," J. Opt. Soc. Am. B **3**, 1625 (1986).

4   J. H. Glownia, J. Misewich and P. P. Sorokin, "160-fsec XeCl excimer amplifier system," J. Opt. Soc. Am. B **4**, 1061 (1987).

5   N. Sarukura, Y. Ishida, H. Nakano and Y. Yamamoto, "cw passive mode locking of a Ti:sapphire laser," Appl. Phys. Lett. **56**, 814 (1990).

6   D. Strickland and G. Mourou, "Compression of amplified chirped optical pulses," Optics Comm. **56**, 219 (1985).

7   D. Kühlke, U. Herpers and D. von der Linde, "Soft x-ray emission from subpicosecond laser-produced plasmas," Appl. Phys. Lett. **50**, 1785 (1987).

8   O. L. Landen, E. M. Campbell and M. D. Perry, "X-ray characterization of picosecond laser plasmas," Optics Comm. **63**, 253 (1987).

9   D. G. Stearns, O. L. Landen, E. M. Campbell and J. H. Scofield, "Generation of ultrashort x-ray pulses," Phys. Rev. A **37**, 1684 (1988).

10 J. A. Cobble, G. A. Kyrala, A. A. Hauer, A. J. Taylor, C. C. Gomez, N. D. Delamater and G. T. Schappert, "Kilovolt x-ray spectroscopy of a subpicosecond-laser-excited source," Phys. Rev. A **39**, 454 (1989).

11 J. D. Kmetec, C. L. Gordon, I. J. J. Macklin, B. E. Lemoff, G. S. Brown and S. E. Harris, "MeV x-ray generation with a femtosecond laser," Phys. Rev. Lett. **68**, 1527 (1992).

12 M. M. Murnane, H. C. Kapteyn and R. W. Falcone, "X-ray streak camera with 2 ps response," Appl. Phys. Lett. **56**, 1948 (1990).

13 H. M. Milchberg, R. R. Freeman, S. C. Davey and R. M. More, "Resistivity of a simple metal from room temperature to 10^6 K," Phys. Rev. Lett. **61**, 2364 (1988).

[14] J. C. Kieffer, et al., "Short-pulse laser absorption in very steep plasma density gradients," Phys. Rev. Lett. **62**, 760 (1989).

[15] O. L. Landen, D. G. Stearns and E. M. Campbell, "Measurement of the expansion of picosecond laser-produced plasmas using resonance absorption profile spectroscopy," Phys. Rev. Lett. **63**, 1475 (1989).

[16] G. J. Pert and S. A. Ramsden, "Population inversion in plasmas produced by picosecond laser pulses," Optics Comm. **11**, 270 (1974).

[17] R. Fedosejevs, R. Ottmann, R. Sigel, G. Kühnle, S. Szatmári and F. P. Schäfer, "Absorption of subpicosecond ultraviolet laser pulses in high-density plasma," Appl. Phys. B **50**, 79 (1990).

[18] M. Chaker, J. C. Kieffer, J. P. Matte, H. Pépin, P. Audebert, P. Maine, D. Strickland, P. Bado and G. Mourou, "Interaction of a 1 psec laser pulse with solid matter," Phys. Fluids B **3**, 167 (1991).

[19] V. L. Ginzburg, "Section 20. A special characteristic of an electromagnetic wave field propagating in an inhomogeneous isotropic plasma. The interaction of electromagnetic and plasma waves," in *Propagation of Electromagnetic Waves in Plasma*, edited by W. L. Sadowski and D. M. Gallik. (Gordon and Breach, 1961) p. 377-403.

[20] D. D. Meyerhofer, "The interaction of high intensity lasers with short scale-length plasmas," in the Abstracts of *21st Annual Anomalous Absorption Conference*, (Banff, Alberta, Canada, 1991).

[21] Y.-H. Chuang, D. D. Meyerhofer, S. Augst, H. Chen, J. Peatross and S. Uchida, "Suppression of the pedestal in a chirped-pulse-amplification laser," J. Opt. Soc. Am. B **8**, 1226 (1991).

CHAPTER I

Short and long pulse laser-produced plasmas

I-1 Introduction

Because of the transient nature of laser produced plasmas, the basic parameters such as temperature and density have significant spatial variations within an expanding plasma. This variation is usually represented by scale lengths such as the density- and temperature-scale length of the plasma. For example the electron density scale length is defined $L_n \equiv (\nabla n_e/n_e)^{-1}$. The temperature scale length is usually longer than that of electron density due to the long electron heat conduction range. Of the two scale lengths, the density scale length L_n plays an important role in the interaction of light with plasmas since, for example, it controls the rate of light absorption or dispersion of unstable modes of plasma instabilities. Earlier work has dealt mostly with plasmas with L_n longer than the interacting laser wavelength, λ_L. For the short-pulse plasmas, on the other hand, the scale length is expected to be shorter than λ_L. This is the new feature of the short-pulse laser-plasma interaction.

Although the interaction mechanisms in the short-pulse plasmas are expected to be different from those of long-pulse plasmas, much about short-pulse plasmas can be learned from the comparison of these two kinds of plasmas. There have been a number of studies done for short-pulse laser-plasma interactions covering a wide range of laser intensity ($10^{11} - 10^{16}$ W/cm^2) and pulse width (160 fs − 1 ps) as well as laser wave length (0.25 µm − 1 µm).[1-13] The interaction characteristics of these studies vary depending on the experimental conditions. It is helpful to know what has been learned about short-pulse interactions to clarify the present work boundary. Therefore, the present chapter is devoted to a review of recent short-pulse plasma investigations as well as previous work on long-pulse plasmas.

I-2 Overview of previous work

I-2-a Short-pulse laser interaction studies

Previous experimental work of short-pulse laser-plasma interaction can be divided into four categories: 1) absorption (reflectivity) measurements, 2) plasma expansion characterizations, 3) interaction of solid state matter with intense laser light and 4) short x-ray pulse generation and its characterization. They are further divided into two groups in terms of laser pulse width used for the experiments: 1 ps and less than 0.5 ps.

Absorption measurements have been done at 1 ps [13] and 250 fs [10, 11] with 1-μm and 0.25-μm pulses, respectively, incident on metal targets such as Al, Cu and Au. With 250 fs pulses and intensity $< 10^{14}$ W/cm^2, the measured absorption has been found to be consistent with the Fresnel/Drude model or linear metal optics.[10] The model is valid in the limit of no hydrodynamic motion (expansion) of the plasma that causes a significant penetration of the incident laser field into the overdense or solid density plasma. The absorption is attributed to electron-ion collisions driven by laser electric fields. A very steep (<1 μm) but finite density gradient has been found from 1-ps pulse interactions with a similar intensity. When the laser intensity exceeds 10^{15} W/cm^2, preformed plasma effects and/or nonlinear processes began to be observed. In the present work it has been found that the interaction characteristics change at this intensity.

Plasma expansion characterizations (plasma scale length measurements) have been done by measuring the Doppler shift of light reflected from the expanding plasma [9, 14] or by the comparison of experimental results and the calculations of absorption dependence on laser incident angle and polarization.[4, 7, 8, 10, 11, 14] The scale length inferred from these measurements ranges from 0.01 to 0.2 μm at 10^{14} W/cm^2

depending on the laser pulse width. These numbers will be compared with the results of the present work.

Unique experiments have been done on high temperature solid matter interactions with short-pulse lasers.[2] The resistivity of Al up to 10^6 °K has been obtained by measuring the temperature rise of the laser heated surface. The resistivity saturates at temperatures above $T_e = 40$ eV corresponding to a minimum electron mean free path. The thermal response of metals has been investigated in terms of electron thermal conductivity and electron-lattice energy exchange.[3,15] The relaxation time for which thermal conductivity dominates the relaxation process and the optical damage threshold of metals is determined. Since the response of metals to ultra-short pulses determines the initial formation of plasma on targets, the results of these investigations are of fundamental importance for short-pulse laser-plasma interaction studies.

There have been a number of studies of x-ray conversion efficiency both for continuum[16] and line emission.[17] Kühlke's explanation for the low x-ray conversion efficiency in higher density plasmas is the weaker coupling efficiency. However, this doesn't seem to be the case because high absorption has been observed in a high contrast interaction. The simulations performed by Chaker et al.[13] suggest that a high plasma temperature (higher than 1keV) lasts for a shorter period without a prepulse because of the expansion cooling of higher density plasmas. A recent experiment[18] with $I_L \sim 10^{18}$ W/cm^2 of 120 fs pulses irradiating heavy metals has observed beyond 1 MeV of x-ray photons with energy conversion efficiencies up to 0.3%. The radiation is attributed to the bremsstrahlung emission of very energetic electrons traveling through a solid target resulting in unique short-pulse duration and small source size. However, the mechanism producing the energetic electrons has not been clarified.

From a theoretical viewpoint, four mechanisms are considered to be important to the absorption of short-pulse laser light by matter: 1) collisional absorption[2,8,10,13], 2) "vacuum heating,"[19-21] 3) skin effects[22,23], and 4) resonance absorption.

Any parametric instabilities,[24] which occur in long-scale-length plasma interactions, can not be supported by a short-pulse generated plasma because of the small spatial extent of the plasma. Most of the existing experimental studies have been performed with intensities up to 10^{15} W/cm^2 and are compatible with the collisional (classical) models. In the range of intensity above 10^{16} W/cm^2 and for small scale lengths, L_n/λ ≤ 0.1, the vacuum heating starts dominating the absorption of p-polarized light. This mechanism was first described by Brunel[19] and further investigated by Gibbon $et\ al.$ for an extensive range of plasma parameters.[20] This process is most efficient when the electron quiver amplitude is larger than the plasma scale length so that the electrons acquire the oscillating energy in the vacuum electric field. If the interacting pulse is sufficiently short so that the plasma can be considered as homogeneous within a skin depth in terms of density and temperature, the skin effect might play an important role in absorption.[22, 23] However, in a light material such as Al with a picosecond pulse duration, Rozmus $et\ al.$[22] have showed that the occurrence of a skin effect is prevented by hydrodynamic expansion. When the plasma scale length is longer than the electron quiver amplitude, the resonantly oscillating electric field at the critical density is expected to be important. Much of the theoretical work on resonance absorption can be found in the context of long-scale-length plasma interaction studies that are reviewed in the next section since the mechanism is most relevant to the present investigation.

I-2-b Long pulse laser interaction studies

Laser interactions with plasmas have been the primary focus of laser fusion feasibility research because these processes influence the energy coupling between the laser and fusion targets. These processes include inverse bremsstrahlung, resonance absorption and parametric instabilities among which the latter two have been studied in conjunction with high energy particle production. Inverse bremsstrahlung is significant

when the electron temperature is not very high. This process entirely depends on electron-ion collisions and exhibits no polarization dependence nor high energy particle production. Parametric instabilities require relatively long-scale-length plasmas to be efficient and are expected not to be supported by ultra-short laser produced plasmas. Resonance absorption, on the other hand, depends on the density scale length and the polarization of the interacting pulse so it is most relevant to the present study.

As the laser power increases, the oscillatory electron energy increases and the density gradient around the critical surface steepens, which leads to a short distance between the turning point and the critical surface. These two effects together lead to a stronger resonance field and more efficient resonance absorption. Therefore, resonance absorption becomes a crucial coupling mechanism at higher laser intensity ($I_L\lambda^2 > 10^{16}$ $\mu m^2 W/cm^2$ where I_L and λ are the intensity and wavelength of laser). Since the electron oscillatory energy is proportional to laser wavelength, this is especially the case for relatively long wavelength lasers ($\lambda = 1 \sim 10$ μm) for which most extensive studies have been done.

Numerous experimental and theoretical studies have been done on CO_2-laser-plasma interactions ($\lambda = 10$ μm) with a primary focus being paid to the connection between resonance absorption and high energy electron generation. Since the electron oscillatory energy is proportional to $I_L\lambda^2$, the long wavelength CO_2 laser has been a preferable system for resonance absorption studies. The CO_2 laser systems had been one of the candidates for an ICF driver because of their high conversion efficiency from electric to light energy. However, the high yield hot electrons from CO_2 laser plasmas cause preheat of the fusion target (fuel) making target compression to a desirable density difficult. Therefore, the clarification of the characteristics and mechanisms of hot electron production were the primary focus of investigation to assess the feasibility of CO_2 laser ICF. Since the hot electron production depends on the laser intensity, a glass laser (1 μm) system might also be problematical especially when the laser

intensity exceeds 10^{16} W/cm2.[25] Therefore, hot electrons generated from glass-laser produced plasmas have also been studied extensively.

$I\lambda^2$ scaling of hot electron temperature has been an important signature for the identification of nonlinear processes occurring in the laser-plasma interaction. For instance, theories based on a flux limitation with stochastically heated electrons at the critical surface [26, 27] predict $T_H \sim (I_L\lambda^2)^{2/3}$, whereas resonance absorption is shown to depend on either $(I_L\lambda^2)^{1/2}$ [28, 29] or $(I_L\lambda^2)^{1/3}$.[30] Experimentally obtained T_H by x-ray measurements is compatible with resonance absorption showing an $(I_L\lambda^2)^{1/3}$ dependence.[30-33] Similar results of x-ray measurements also have been found with glass laser systems ($\lambda = 1$ μm) where the dependence varies: $(I_L\lambda^2)^{0.25-0.41}$.[25, 34, 35] These results are further supported by fractional absorption measurements,[36] bremsstrahlung emission dependence on the polarization and incident angle,[37, 38] and the studies of the energy and angular anisotropy of the fast ions.[35, 39, 40] These studies show the incident angle dependence of absorption on p-polarized light, which is particular for resonance absorption, as well as the enhancement of absorption, x-ray bremsstrahlung, and fast ion emission in the case of p-polarized light interaction.

Other characteristics of long-pulse-laser produced plasmas that are relevant to the present investigation include (1) density steepening at the critical region, and (2) self-generated azimuthal coronal magnetic fields due to the currents induced by hot electrons.

In those plasmas, a scale length less than the laser wavelength, $L_n/\lambda_L < 1$, occurs near the critical surface even for relatively long pulse duration (typically subnanosecond to a few nanoseconds) due to the ponderomotive forces in the critical region.[41, 42] However, this steep density step is accompanied by an extended expanding underdense plasma [43] giving raise to parametric instabilities such as SRS (Stimulated Raman Scattering), which needs to be distinguished from the processes occurring at the critical surface. A longer pulse duration leads to a hydrodynamic modification of density

profile [42] and makes simple interpretation of phenomena difficult. Ultra-short-pulse experiments, on the other hand, can make this point clearer since the critical surface with a steep density gradient is directly adjacent to vacuum and the number of processes is reduced. For instance, parametric instabilities whose thresholds are determined by the balance between the incident pumping and plasma wave convection cannot grow in the steep density gradient. Furthermore, the short distance between the laser turning point (reflecting point) and the critical surface results in the large enhancement of resonantly oscillating laser electric fields because the decay of p-polarized field is minimized. Thus the resonantly oscillating fields and resulting phenomena are expected to dominate the short-pulse interactions.

I-3 The novel aspects of the present work in ultra-short laser interaction studies

This thesis describes an experimental characterization of high intensity contrast 1-ps laser produced plasma at 1-μm wave length. Although there has been much work done for ultra-short laser-plasma interactions, very few reports have compared high contrast with low contrast interactions. Here high contrast interactions are those where the contrast between the main picosecond pulse and a prepulse is high enough that no preformed plasma exists before the arrival of the main pulse. In the case of the low contrast interaction condition the main picosecond pulse interacts with a preformed plasma. The dominant interaction mechanism among various processes depends on the size and scale length of plasma in which the laser light propagates. The present study has found significant changes in interaction phenomena between the low contrast and high contrast interactions. Although the primary focus of the investigation in this study is the high contrast picosecond laser-plasma interactions, a comparison between the two contrast cases makes the high contrast interaction characteristics clearer. Therefore,

experimental observations from low contrast pulse interactions are also presented as necessary to contrast the characteristics of high contrast pulse interactions.

Most of the previous work characterizing ultra-short laser-plasma interactions has been done by comparing measured absorption with the solutions of Maxwell's equations employing a phenomenological collision frequency (damping rate). This methodology becomes inadequate when detailed interaction mechanisms are to be explored and nonlinear processes begin to play an important role. As described in the previous section, the interaction processes in the range of laser intensity of the present interest ($10^{14}-10^{16}$ W/cm^2) are expected to be dominated by nonlinear mechanisms that produce high energy particles. Although the direct measurements of high energy particles have not previously been used as diagnostics in picosecond interaction experiments, these measurements become inevitable as the nonlinear processes begin to dominate. In this study, high energy electron and ion emissions as well as absorption and x-ray measurements are used to characterize the interaction mechanisms in the picosecond laser plasmas. In particular, ion blowoff has been extensively characterized and used to estimate various plasma parameters.

The target plasma is generated on smooth solid Al plates where the plasma has a strong inhomogeneity (density gradient) along the target normal. Under such plasma conditions, the laser electric field component along the density gradient (p-polarized field) can excite plasma waves resonantly while another component (perpendicular to the gradient) has no effects on the plasma wave excitation. The excitation of plasma waves by a p-polarized light is depicted in Fig. 1-1. The transverse electromagnetic waves have electric field components along the density gradient at the turning point and excite longitudinal electrostatic waves. Since electron plasma waves oscillate at the plasma natural frequency which is a function of plasma density, the electrostatic wave becomes resonant at the critical surface where the plasma frequency equals the laser

frequency. Thus the p-polarized transverse electromagnetic wave energy is converted to the longitudinal electrostatic wave energy.
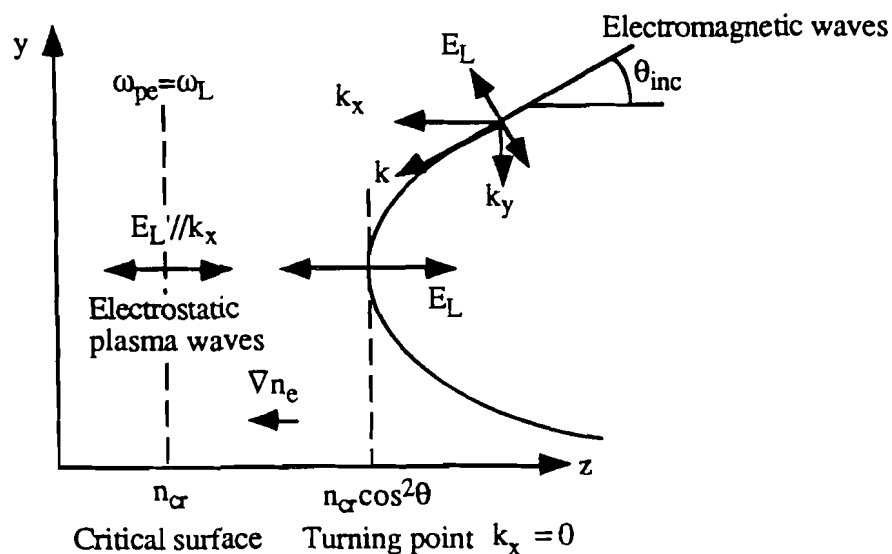
Fig. 1-1 The y-z plane defines the laser plane of incidence. For p-polarized EM waves, the electric field vector lies in this plane and it is in the z-direction (parallel to the density gradient) at the turning point.

Therefore, the polarization of obliquely incident laser electric fields has significant effects on the interaction characteristics and is chosen as one of the primary experimental parameters. The effects of polarization are examined by independently altering the total laser intensity and p-polarized electric field component (electric fields lying in the plane of incidence or along the density gradient). The characteristics of high energy electrons and ions have been found to depend on the p-polarized component alone.

Previously in long scale length plasmas the high energy electron generation from the critical surface has been attributed to wavebreaking acceleration or electron trapping in plasma waves. The high energy electrons produced from the short scale length

plasmas, on the other hand, exhibit a fairly monoenergetic spectrum and consist of almost the entire population of electrons in the resonance region. These features are not expected from wavebreaking or electron trapping. Therefore, a new mechanism for the observed electron acceleration from the resonance region has been introduced, that is, the ponderomotive acceleration.

The determining processes of enhanced p-polarized field that accelerates the high energy electrons by its ponderomotive force have been examined. Various processes are compared in terms of their limiting effects on the resonantly oscillating fields. The enhanced fields have been determined experimentally and found to be best described by plasma-wave dispersion effects.

Based on the experimental observations and comparisons with theoretical estimations, the following physical picture for high energy particle acceleration has been drawn. Figure 1-2 illustrates the process showing the enhanced laser field along with the plasma density profile. When an obliquely incident laser pulse has a p-polarized electric field component at the turning point in a plasma, the field penetrates to the critical surface and drives electrons resonantly. These oscillating electrons build an electrostatic wave and enhance the incident laser field. In a short scale-length plasma, the enhancement is limited by plasma-wave dispersion effects. Since the resonance field is highly localized, the ponderomotive force that is proportional to the gradient of the field is significant. This ponderomotive force mainly acts on the electrons in the resonance region and accelerates them to its potential energy. The electrons accelerated toward vacuum leave immobile ions behind and build up an ambipolar field. This ambipolar field then accelerates the ions. Eventually the ions catch up with the electron motion and expand together. During this process, almost the entire energy initially residing in the electrons is transferred to the ion kinetic energy.
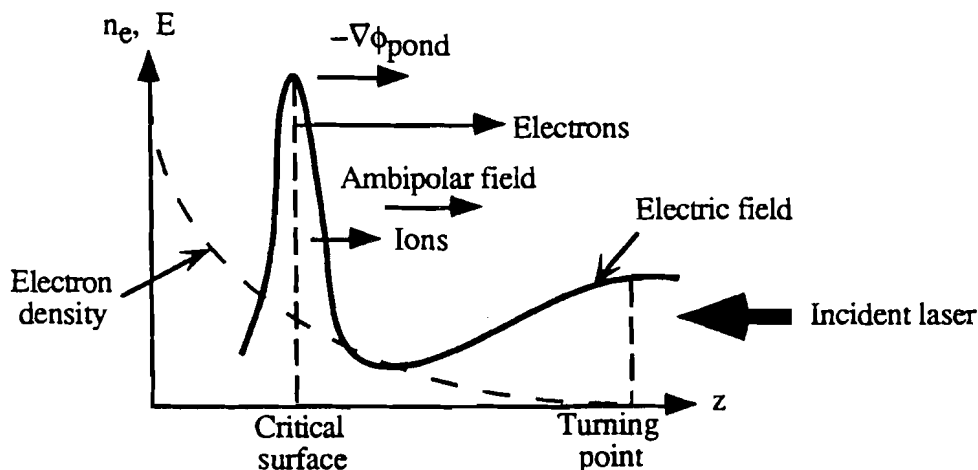
Fig. 1-2 Ponderomotive acceleration of high energy particles. The spatial profile of the laser electric field (solid line) and the electron density (broken line) are shown.

REFERENCES

[1] O. L. Landen, E. M. Campbell and M. D. Perry, "X-ray characterization of picosecond laser plasmas," Optics Comm. **63**, 253 (1987).

[2] H. M. Milchberg, R. R. Freeman, S. C. Davey and R. M. More, "Resistivity of a simple metal from room temperature to 10^6 K," Phys. Rev. Lett. **61**, 2364 (1988).

[3] P. B. Corkum, F. Brunel, N. K. Sherman and T. Srinivasan-Rao, "Thermal response of metals to ultrashort-pulse laser excitation," Phys. Rev. Lett. **61**, 2886 (1988).

[4] O. L. Landen, D. G. Stearns and E. M. Campbell, "Measurement of the expansion of picosecond laser-produced plasmas using resonance absorption profile spectroscopy," Phys. Rev. Lett. **63**, 1475 (1989).

[5] M. M. Murnane, H. C. Kapteyn and R. W. Falcone, "High-density plasmas produced by ultrafast laser pulses," Phys. Rev. Lett. **62**, 155 (1989).

6   M. M. Murnane, H. C. Kapteyn and R. W. Falcone, "Generation and application of ultrafast x-ray sources," IEEE J. Quantum Electron. **25**, 2417 (1989).

7   J. C. Kieffer, et al., "Short-pulse laser absorption in very steep plasma density gradients," Phys. Rev. Lett. **62**, 760 (1989).

8   J. C. Kieffer, et al., "Absorption of an ultrashort laser pulse in very steep plasma density gradients," IEEE J. Quantum Electron. **25**, 2640 (1989).

9   H. M. Milchberg and R. R. Freeman, "Expansion-induced Doppler shifts from ultrashort-pulse laser-produced plasmas," Phys. Rev. A **41**, 2211 (1990).

10 R. Fedosejevs, R. Ottmann, R. Sigel, G. Kühnle, S. Szatmári and F. P. Schäfer, "Absorption of subpicosecond ultraviolet laser pulses in high-density plasma," Appl. Phys. B **50**, 79 (1990).

11 R. Fedosejevs, R. Ottmann, R. Sigel, G. Kühnle, S. Szatmári and F. P. Schäfer, "Absorption of femtosecond laser pulses in high-density plasma," Phys. Rev. Lett. **64**, 1250 (1990).

12 T. Engers, W. Fendel, H. Schüler, H. Schulz and D. von der Linde, "Second-harmonic generation in plasmas produced by femtosecond laser pulses," Phys. Rev. A **43**, 4564 (1991).

13 M. Chaker, J. C. Kieffer, J. P. Matte, H. Pépin, P. Audebert, P. Maine, D. Strickland, P. Bado and G. Mourou, "Interaction of a 1 psec laser pulse with solid matter," Phys. Fluids B **3**, 167 (1991).

14 H. M. Milchberg and R. R. Freeman, "Light absorption in ultrashort scale length plasmas," J. Opt. Soc. Am. B **6**, 1351 (1989).

15 H. E. Elsayed-Ali and J. W. Herman, "Picosecond time-resolved surface-lattice temperature probe," Appl. Phys. Lett. **57**, 1508 (1990).

[16] D. Kühlke, U. Herpers and D. von der Linde, "Soft x-ray emission from subpicosecond laser-produced plasmas," Appl. Phys. Lett. **50**, 1785 (1987).

[17] J. A. Cobble, G. T. Schappert, L. A. Jones, A. J. Taylor, G. A. Kyrala and R. D. Fulton, "The interaction of a irradiance, subpicosecond laser pulse with aluminum: The effects of the prepulse on x-ray production," J. Appl. Phys. **69**, 3369 (1991).

[18] J. D. Kmetec, C. L. Gordon, I. J. J. Macklin, B. E. Lemoff, G. S. Brown and S. E. Harris, "MeV x-ray generation with a femtosecond laser," Phys. Rev. Lett. **68**, 1527 (1992).

[19] F. Brunel, "Not-so-resonant, resonant absorption," Phys. Rev. Lett. **59**, 52 (1987).

[20] P. Gibbon and A. R. Bell, "Collisionless absorption in sharp-edged plasmas," Phys. Rev. Lett. **68**, 1535 (1992).

[21] G. Bonnaud, P. Gibbon, J. Kindel and E. Williams, "Laser interaction with a sharp-edged overdense plasma," Laser Part. Beams **9**, 339 (1991).

[22] W. Rozmus and V. T. Tikhonchuk, "Skin effect and interaction of short laser pulses with dense plasmas," Phys. Rev. A **42**, 7401 (1990).

[23] E. G. Gamaliy and R. Dragila, "Interaction of ultrashort laser pulses at relativistic intensities with solid targets: Relativistic skin effect," Phys. Rev. A **42**, 929 (1990).

[24] C. S. Liu, "Parametric instabilities in an inhomogeneous unmagnetized plasmas," in *Advances in Plasma Physics*, edited by A. Simon and W. B. Thomson. (Wiley, New York, 1976) 6: p.121-176.

[25] K. R. Manes, H. G. Ahlstrom, R. A. Haas and J. F. Holzrichter, "Light-plasma interaction studies with high-power glass laser," J. Opt. Soc. Am. **67**, 717 (1977).

[26] R. L. Morse and C. W. Neilson, "Occurrence of high-energy electrons and surface expansion in laser-heated target plasmas," Phys. Fluids **16**, 909 (1973).

[27] H. H. Klein and W. M. Manheimer, "Effect of plasma inhomogeneity on the production of energetic electrons," Phys. Rev. Lett. **33**, 353 (1974).

[28] D. W. Forslund, J. M. Kindel, K. Lee, E. L. Lindman and R. L. Morse, "Theory and simulation of resonant absorption in a hot plasma," Phys. Rev. A **11**, 679 (1975).

[29] K. G. Estabrook, E. J. Valeo and W. L. Kruer, "Two-dimensional relativistic simulations of resonance absorption," Phys. Fluids **18**, 1151 (1975).

[30] D. W. Forslund, J. M. Kindel and K. Lee, "Theory of hot-electron spectra at high laser intensity," Phys. Rev. Lett. **39**, 284 (1977).

[31] G. D. Enright, N. H. Burnett and M. C. Richardson, "X-ray emission characteristics of plasmas created by a high-intensity CO_2 laser," Appl. Phys. Lett **31**, 494 (1977).

[32] G. D. Enright, M. C. Richardson and N. H. Burnett, "Superthermal x-ray emission from CO_2-laser-produced plasmas," J. Appl. Phys. **50**, 3909 (1979).

[33] H. Pépin, B. Grek and F. Rheault, "X-ray emission measurements from CO_2-laser-created plasmas," J. Appl. Phys. **48**, 3312 (1977).

[34] R. A. Haas, H. D. Shay, W. L. Kruer, M. J. Boyle, D. W. Phillion, F. Rainer, V. C. Rupert and H. N. Kornblum, "Interaction of 1.06-μm laser radiation with planar targets," Phys. Rev. Lett. **39**, 1533 (1977).

[35] B. Luther-Davies, "X-ray bremsstrahlung and fast-ion measurements from picosecond laser-produced plasmas," Optics Comm. **23**, 98 (1977).

[36] K. R. Manes, V. C. Rupert, J. M. Auerbach, P. Lee and J. E. Swain, "Polarization and angular dependence of 1.06-μm laser-light absorption by planar plasmas," Phys. Rev. Lett. **39**, 281 (1977).

[37] B. Luther-Davies, "Evidence of resonance absorption in laser-produced plasmas from the polarization and angular dependence of high-energy x-ray bremsstrahlung emission," Appl. Phys. Lett. **32**, 209 (1978).

[38] J. E. Balmer and T. P. Donaldson, "Resonance absorption of 1.06μm laser radiation in laser-generated plasma," Phys. Rev. Lett. **39**, 1084 (1977).

[39] J. S. Pearlman, J. J. Thomson and C. E. Max, "Polarization-dependent absorption of laser radiation incident on dense-plasma planar targets," Phys. Rev. Lett. **38**, 1397 (1977).

[40] P. Wägli and T. P. Donaldson, "Fast-ion emission and resonance absorption in laser-generated plasma," Phys. Rev. Lett. **40**, 875 (1978).

[41] R. Fedosejevs, M. D. J. Burgess, G. D. Enright and M. C. Richardson, "The electron density structure of the plasma produced on glass microballoons by 10.6 μm radiation," Phys. Fluids **24**, 537 (1981).

[42] D. R. Bach, et al., "Intensity-dependent absorption in 10.6-μm laser-illuminated spheres," Phys. Rev. Lett. **50**, 2082 (1983).

[43] A. Raven and O. Willi, "Electron-density structures in laser-produced plasmas at high irradiances," Phys. Rev. Lett. **43**, 278 (1979).

CHAPTER II

Theoretical background

II-1 Introduction

There are several physical concepts that need to be covered to characterize and understand the plasma conditions under investigation. These include,

1. Electromagnetic (EM) wave propagation in a short-scale-length plasma

2. Electric field enhancement at the critical surface by plasma oscillation

3. The ponderomotive potential in plasma

4. Isothermal plasma expansion

The behavior of an EM wave in an underdense plasma has been well characterized by the WKB approximation. This is valid when the fields vary slowly in space since the method solves the wave equations by each order of derivative assuming a higher order derivative is negligible compared to a lower order.[1] However, for picosecond laser plasmas where L_n is shorter distance than the laser wavelength or for sharply peaked resonance fields at the critical surface, the fields vary in distances shorter than wavelength and the slowly varying approximation breaks down. Maxwell's equations then have to be solved numerically.

When laser light has a p-polarized component, linear mode coupling of the EM wave to the electrostatic plasma wave takes place at the resonance region where the plasma frequency nearly equals the laser frequency (see Fig. 1-1). Such a mode conversion could be very efficient in a short-scale-length plasma where incident waves reach the resonance region before being strongly attenuated. The amplitude of the resonantly oscillating fields in short scale-length plasmas is then determined by the balance between the enhancement of the plasma wave through the mode conversion and convection of the wave out of the resonance region.

The enhanced electric field leads to the acceleration of plasma particles to suprathermal energies. The mechanism of the acceleration varies depending on the plasma temperature and driving laser electric field amplitude. In a cold plasma, the electron fluid oscillates harmonically in the driving field. As the oscillation develops, the plasma wave breaks when one fluid element overtakes another. The resonantly oscillating field can no longer keep electron harmonic motion thus the oscillation energy is abruptly converted to an electron random energy. The strength of the oscillation is then limited to the wavebreaking amplitude. When a plasma has a very steep density gradient, on the other hand, the plasma wave dispersion takes energy out of the resonance region and determines the steady state wave amplitude when the dispersion balances the input energy flux. The ponderomotive acceleration of the suprathermal electrons from the resonantly enhanced field is the consistent picture with the experimental results. This mechanism is examined against the wavebreaking mechanism. The amplitude of the resonantly enhanced field is inferred from the ion kinetic energy through the ponderomotive potential.

One proven technique to characterize the suprathermal electrons from the resonantly enhanced field is an ion measurement. An isothermal expansion model of ion (plasma) provides a means of estimating plasma temperature. The velocity distribution of ions exhibits a high energy tail that can be well described by the model and determines the plasma temperature. The velocity distribution of ions reflects the characteristics of electrons that accelerate ions through an ambipolar electric field. The ion kinetic energy is used to estimate the ponderomotive potential of the resonance fields and show that the accelerated electrons have a fairly monoenergetic spectrum.

II-2 EM wave propagation in a short scale length plasma

The understanding of EM wave propagation in a plasma is of primary importance for the investigation of short-pulse laser-plasma interactions. In short-pulse laser-

plasma interactions, the EM wave interacts with a highly inhomogeneous plasma where the plasma scale length,

$$L_n \equiv (\nabla n_e/n_e)^{-1}$$

is much shorter than the wavelength of laser. When laser light is obliquely incident on such plasmas, the interaction exhibits a strong dependence on the laser polarization and the angle of incidence.

When an EM wave propagates in plasma obliquely to the density gradient, two locations become important, turning point and the critical surface. Figure 2-1 depicts these two locations with the spatial variation of p-polarized laser electric field. Since plasmas are dispersive, EM waves propagating obliquely to the axis of inhomogeneity towards high density region deflect and eventually reflect from the plasma region. The point where the EM waves turn around is called the turning point. Beyond the turning point, the field strength decays exponentially and a finite amount of field penetrates through the higher density region, the electric field tunneling. If the tunneling field has a component along the density gradient, it excites electron plasma oscillations. These oscillations become resonant at the critical surface where the local plasma frequency ω_{pe} equals the laser frequency ω_0. Because of the resonant nature of the oscillation, the amplitude of electric fields can be driven to much larger values than that of driving electric fields and accelerate electrons to very high energies. To examine EM wave interaction with plasmas, the modification of the propagating EM fields in the plasma needs to be known. In this section the propagation of an EM wave in a plasma is reviewed [2] emphasizing the solution for p-polarized light to give a basis for an estimate of field structure in plasma.
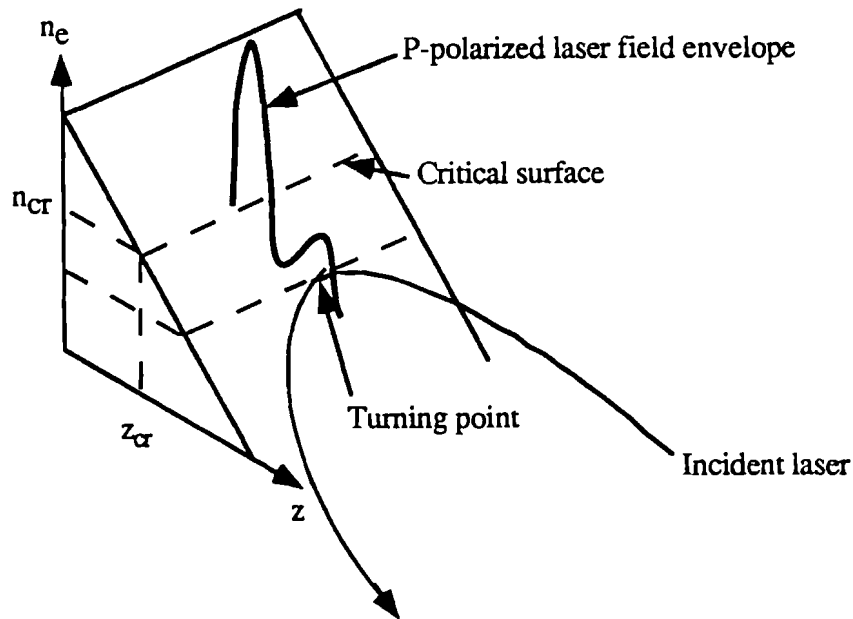
Fig. 2-1   An EM wave propagation obliquely incident in an inhomogeneous
plasma and two important locations, the turning point and the critical
surface. The spatial variation of p-polarized laser electric field is
also shown.

The wave equations of laser light with a frequency ω propagating in a plasma can
be developed from Faraday's law and Ampere's law,

$$\nabla \times E(\omega) = \frac{i\omega}{c} B(\omega) \qquad\qquad 2\text{-}1$$

$$\nabla \times B(\omega) = \frac{4\pi}{c} J - \frac{i\omega}{c} E(\omega). \qquad\qquad 2\text{-}2$$

The displacement current is neglected compared with the conduction current. The
conductivity of plasma σ ($J = \sigma E$) is calculated from a linearized force equation of
electron fluid,

$$\frac{\partial v_e}{\partial t} = \frac{e}{m_e} E - v_{ei} v_e$$

or

$$v_e = \frac{-ieE(\omega)}{m_e(\omega + iv_{ei})},$$

where v_e is the velocity of the electron fluid and v_{ei} is the collision frequency. The plasma current density is

$$J = -n_e e v_e = \frac{i\omega_{pe}^2}{4\pi(\omega + iv_{ei})} E(\omega),$$

where ω_{pe} is the plasma frequency, $\omega_{pe} = \sqrt{\frac{4\pi n_e e^2}{m_e}}$.

Ampere's law (2-2) becomes

$$\nabla \times B = \left[\frac{4\pi}{c}\sigma - \frac{i\omega}{c} \right] E$$

$$= -\frac{i\omega}{c} \varepsilon(z) E, \qquad\qquad 2\text{-}3$$

where $\varepsilon(z) = 1 - \frac{\omega_{pe}^2}{\omega(\omega + iv_{ei})}$ is the dielectric function of the plasma. From the

equations (2-1) and (2-3), the wave equations for E and B are

$$\nabla^2 E - \nabla(\nabla \cdot E) + \frac{\omega^2}{c^2} \varepsilon(z) E = 0 \qquad\qquad 2\text{-}4$$

$$\nabla^2 B - \frac{1}{\varepsilon(z)}\nabla\varepsilon(z) \times (\nabla\times B) + \frac{\omega^2}{c^2} \varepsilon(z) B = 0. \qquad\qquad 2\text{-}5$$

The second term of Eq. 2-4 leads to an important consequence of the resonantly enhanced laser field at the critical surface. When this term is zero, the wave is purely electromagnetic and no mode conversion from EM wave to electrostatic (ES) waves takes place. This term corresponds to an ES mode of the incident laser field and only

exists for the case of p-polarization. Poisson's equation gives $\nabla \bullet (\epsilon(z)E) = 0$ which can be expanded to yield

$$\nabla \bullet E = -\frac{1}{\epsilon}\frac{\partial \epsilon}{\partial z}E_z.$$

The divergence of E exhibits a resonant response at the critical surface where $Re(\epsilon) = 0$. The existence of this term introduces additional complexity in solving the wave equation and makes the B-field (Eq. 2-5) a preferable choice as described in the next section. Equations 2-4 and 2-5 are redundant and the choice between E and B depends on the polarization of the EM wave propagating in an inhomogeneous plasma. In short-pulse laser interactions, the plasma density profile can be considered as one dimensional (planar expansion), since the plasma expands a distance much less than its diameter ($\approx 1\%$). Therefore, without loss of generality, Cartesian coordinates can be defined as shown in Fig. 2-2.
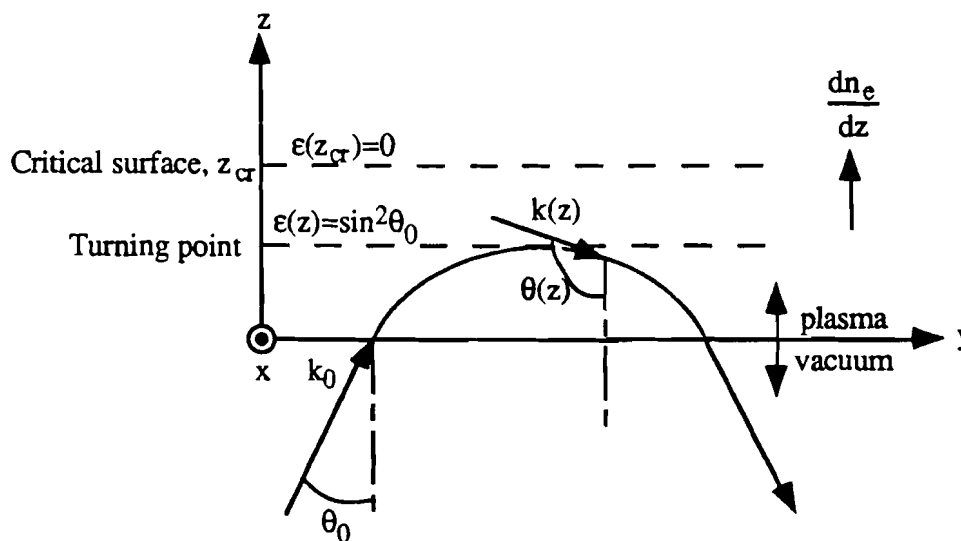
Fig. 2-2   Oblique incidence (angle of incidence θ_0) of an EM wave on a planar plasma density profile (density gradient parallel to the z-axis). Vacuum-plasma boundary is at z=0. Wave k-vector is a function of z and turns around at $\epsilon=\sin^2\theta_0$.

Here the z-axis is in the direction of the plasma density gradient ($dn_e/dz > 0$), i.e., target normal, and the y-z plane is the plane of incidence. The above assumption ensures that the wave is independent of x coordinate. The plasma-vacuum boundary is set to be at z=0 plane, i.e., n_e=0 for z<0. The angle of incidence θ_0 is defined as an angle between the wave k vector in vacuum and the z-axis perpendicular to target.

For p-polarized light, the electric field vector has two components that transform Eq. (2-4) into

$$\frac{\partial^2 E_y}{\partial y^2} + \frac{\partial^2 E_y}{\partial z^2} - \frac{\partial}{\partial y} \nabla \cdot E + \frac{\omega^2}{c^2} \varepsilon(z) \, E_y = 0$$

$$\frac{\partial^2 E_z}{\partial y^2} + \frac{\partial^2 E_z}{\partial z^2} - \frac{\partial}{\partial z} \nabla \cdot E + \frac{\omega^2}{c^2} \varepsilon(z) \, E_z = 0.$$

These are coupled equations for E_y and E_z so it is convenient to work with Eq. (2-5) which yields a single wave equation for p-polarized light where the **B** field has only the x-component B_x,

$$\frac{\partial^2 B_x}{\partial y^2} + \frac{\partial^2 B_x}{\partial z^2} - \frac{1}{\varepsilon(z)} \frac{\partial \varepsilon(z)}{\partial z} \frac{\partial B_x}{\partial z} + \frac{\omega^2}{c^2} \varepsilon(z) \, B_x = 0. \qquad 2\text{-}6$$

Equation (2-6) can be solved by expressing B_x as $\widetilde{B}(z)\exp(-ik\alpha y)$ where

$$k(z) = \frac{\omega}{c}\sqrt{\varepsilon(z)}$$

and

$$\alpha(z) = \sin\theta(z).$$

Here $\theta(z)$ is the instantaneous angle between k-vector and z-axis and $\widetilde{B}$ is the complex magnetic field along x. Substituting this expression into Eq. (2-6) yields

$$\frac{d^2\widetilde{B}}{dz^2} + k^2(1 - \alpha^2)\widetilde{B} - \frac{1}{\varepsilon}\frac{d\varepsilon}{dz}\frac{d\widetilde{B}}{dz}$$

$$= i \left\{ 2\frac{d(k\alpha)}{dz} y \frac{d\widetilde{B}}{dz} + 2\frac{d(k\alpha)}{dz} y \widetilde{B} + \frac{d^2(k\alpha)}{dz^2} y \widetilde{B} \right\} + y^2\widetilde{B}\left[\frac{d(k\alpha)}{dz}\right]^2$$

The fact that the left-hand side is independent of y requires both sides be equal to zero, i.e.,

$$\frac{d^2\widetilde{B}}{dz^2} + \frac{\omega^2}{c^2}\epsilon(z)(1 - \sin^2\theta(z))\widetilde{B} - \frac{1}{\epsilon}\frac{d\epsilon}{dz}\frac{d\widetilde{B}}{dz} = 0 \qquad 2\text{-}7$$

and letting the real and imaginary parts of the right hand side be independently zero gives

$$\frac{d(k\alpha)}{dz} = 0. \qquad 2\text{-}8$$

Here $v_{ei}/\omega \ll 1$, that is, a real value of $k(z)$ is assumed. Equation (2-8) leads to the law of refraction, $k(z)\sin\theta(z) = k_0\sin\theta_0$, where k_0 is the vacuum wave number of the laser.

Equation (2-7) has an analytical solution [6] for a linear plasma density profile; however, as shown in the next section and chapter IV, an exponential density profile is more physically relevant. An exponential profile requires a numerical integration of Eq. 2-7.[3, 4] To prepare Eq 2-7 for numerical treatments, $\widetilde{B}$ needs to be separated into $\widetilde{B} = B(z)\exp[-i\phi(z)]$, where B and ϕ are real. Substituting this expression into Eq. 2-7 and setting the real and imaginary parts to 0 separately gives the set of coupled equations for B and $u \equiv d\phi_B/dx$:

$$\frac{d^2B}{dx^2} - u^2B + k^2(\cos^2\theta - \zeta)B - \frac{1}{(1 - \zeta)^2+\left(\dfrac{v}{\omega}\right)^2\zeta^2}\left(F\frac{dB}{dx} + GBu\right) \qquad 2\text{-}9$$

$$\frac{du}{dx} + \frac{2u}{B}\frac{dB}{dx} - k^2\frac{v}{\omega}\zeta + \frac{1}{(1 - \zeta)^2+\left(\dfrac{v}{\omega}\right)^2\zeta^2}\left(G\frac{dB}{dx} - FBu\right). \qquad 2\text{-}10$$

Here,

$$F(x) = \frac{v}{\omega} \zeta \frac{d}{dx}\left(\frac{\zeta v}{\omega}\right) - (1 - \zeta)\frac{d\zeta}{dx},$$

$$G(x) = \frac{v}{\omega} \zeta \frac{d\zeta}{dx} + (1 - \zeta)\frac{d}{dx}\frac{\zeta v}{\omega},$$

and

$$\zeta = \frac{\omega_p^2/\omega^2}{1 + v^2/\omega^2}.$$

Equations 2-9 and 2-10 are integrated from the overdense region to the underdense region to calculate the value at the critical density. The overdense region was chosen as a starting point of integration to match the boundary condition of evanescent waves. The electric field at the critical surface is a sum of the electromagnetic driving field, E_d, and the resonantly enhanced electrostatic field supported by the plasma oscillations. The electrostatic field will be discussed in the next section. With Ampere's law and the law of refraction, the electric field E_d can be expressed in terms of vacuum electric field and decay factor through the critical surface,

$$E_d = B_d \sin\theta_0 = \eta_t E_0,$$ 2-11

where B_d is the corresponding magnetic field penetrating through the critical surface. Note that E_d is not the resonantly oscillating electric field but the laser electric field that tunnels through from the turning point to the resonance point and drives the plasma wave resonantly at the critical density. The resonantly oscillating field at the resonance surface is derived in next section by coupling this field with plasma oscillations.

Figure 2-3 shows the example of laser electric field profile calculated, according to Eqs. 2-9 and 2-10, for $n(z) = n_0 e^{z/L_n}$ where $L_n = 1500$Å that is assumed to be constant

across the region. The laser electric field strength is normalized to its maximum value (at 5000Å) and the distance is measured relative to the critical density. In this example the laser electric field decays to ~20% of its vacuum value at the critical density. The decay factor η_t varies from 23% to 17% as the scale length increases from 1000Å to 2000Å.
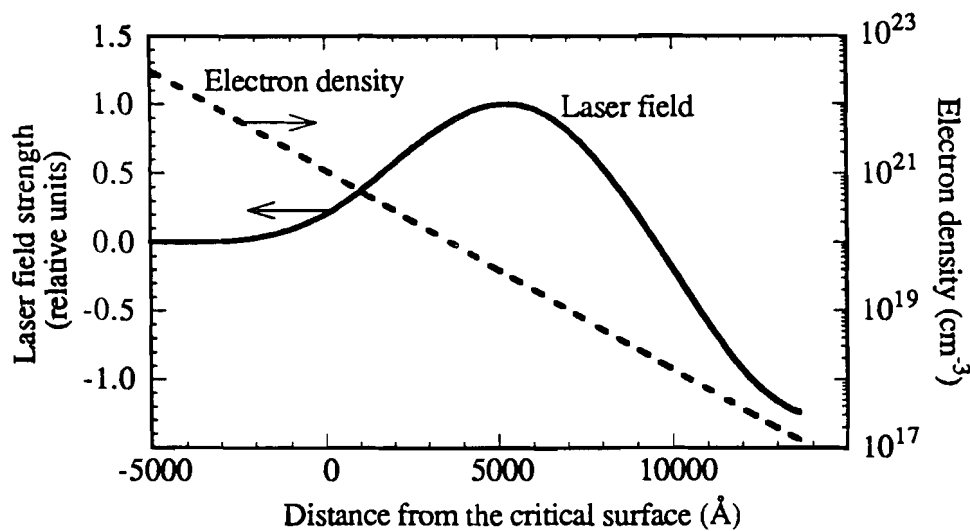
Fig. 2-3   Laser electric field profile around the critical surface. The field strength is normalized to the maximum value and the distance is relative to the critical surface. The broken line indicates the plasma density profile used in the calculation.

II-3 Electric field enhancement at the critical surface

The tunneling electric fields of p-polarized light at the critical surface drive the electrons along the density gradient and resonantly drives electron plasma wave. This leads to the enhancement of electric field strength as shown in Fig. (2-4). There are two types of field "swelling" appearing in this figure near the resonance surface. One of them is so called Airy swelling [5] whose cause can be understood by noting that the

energy flux of light is conserved and the group velocity of light, $v_g = c\varepsilon(n_e)^{1/2}$, becomes minimum at the turning point.[1] Since this swelling is due to the conservation of energy alone, it can exist for either s- or p-polarization. Another swelling, which is the primary interest in this thesis, is the field enhancement at the critical surface caused by the resonance response of plasma oscillation to incident fields. When the laser electric field oscillates the plasma electrons along the density gradient the laser light has a p-polarized component, it creates a charge separation because ions are immobile. This charge separation then drives the plasma oscillation at a plasma frequency depending on the local density. The driving is resonant where the local plasma frequency matches the incident laser frequency. This oscillation does not occur for an s-polarized field component.
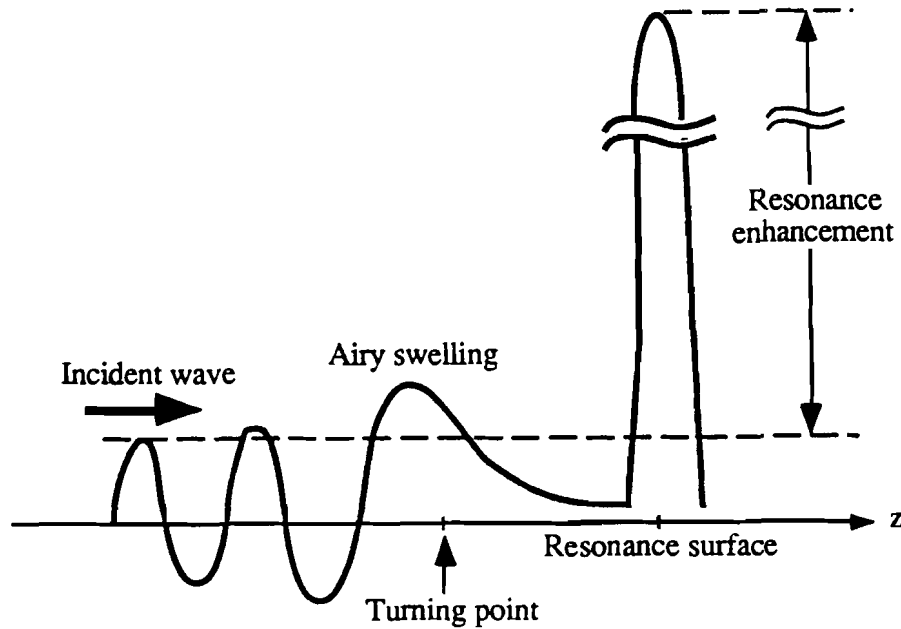
Fig. 2-4   Laser electric field profile obliquely incident on an expanding plasma
showing an Airy swelling and a resonance enhancement. The Airy
swelling is due to the decrease of group velocity whereas the
resonance enhancement is due to the resonance response of plasma
at the critical surface. The horizontal and vertical scale do not
necessary reflect the real scaling.

Because of the resonance feature of this oscillation the enhancement could be
infinite if no process takes energy out of the region or broadens the resonance region.
In the long scale length plasma, electron-ion collisions determine the width of the
resonant region and thus the maximum enhancement. As the scale length becomes
shorter, the width of the resonant region becomes narrower and the enhancement
further develops. When the width becomes smaller than electron oscillation amplitude
or the Debye length, either one of these dimensions determines the width of the
resonance. The electron oscillation in the resonant field averages the field strength and
broadens the width; thus the enhancement is lower than that predicted by collisional
effects. The Debye length determines the range in which collective plasma response
has an effect, i.e., the width of resonantly oscillating field when limited by a plasma

wave convection.[6] These two limiting processes can be related to wavebreaking[7] and the ponderomotive acceleration of electrons and are described in some detail in this section.

When the resonant field width is larger than the Debye length or electron oscillating amplitude, the field enhancement is determined by the ratio of the laser frequency, ω_0 and the electron-ion collision frequency, ν_c at the critical surface. This is derived by solving EM wave equations for p-polarized case and calculates the electric field at the critical surface.[6, 8] The laser intensity enhancement is given by

$$\frac{\omega_0{}^2}{\nu_c{}^2} \sin^2\theta_{inc} \exp(-2kL_n),$$

where θ_{inc} and k are an angle of incidence and a laser wave vector. The width of the field, δ is then given by $\frac{\nu_c}{\omega_0} L_n$. When the plasma scale length is short enough so that the field width becomes shorter than the electron oscillating amplitude, χ_{osc} or the Debye length, λ_{De}, the resonant field begins to be broadened by the field averaging effects due to the electron oscillation or the plasma pressure perturbation (plasma wave dispersion).

Wavebreaking is a process in which neighboring electron fluid elements overtake each other in a harmonic motion driven by an external field.[9, 10] Through this process, the oscillating electron energy is abruptly transferred to electron kinetic energies and accelerates electrons out of the resonance region. The mechanism of wavebreaking can be examined by considering the equation of electron motion and Poisson's equation. When external electric field, E_d, drives plasma electrons around its critical density in the direction of density inhomogeneity, the charge separation between electrons and immobile ions induces a resonance field which in turn drives the electron oscillation and enhances itself. The enhancement is strongest at the exact resonance (or critical density), whereas neighboring oscillations are dephased from the driver due to

their different natural frequency. Therefore, the amplitude of electron oscillation is largest at the resonance surface leading to the overtaking between the neighboring fluid component as the oscillation develops. This process is illustrated in Fig. 2-5 where the abscissa and ordinate correspond to the initial and present positions of electrons, respectively. The fluid overtaking occurs where $dz/dz_0 = 0$ the region indicated by the square. It has been shown that the electron fluid elements satisfying this overtaking condition that consists of a few percent of electron population traverse the resonance region in phase with the field and escape it.[7, 11]
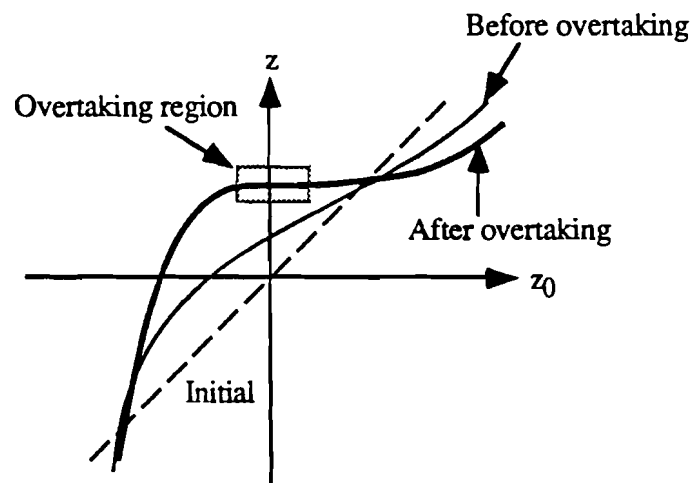
Fig. 2-5. Overtaking of electron fluid oscillation in resonance field. z_0 and z correspond to initial and present positions, respectively. Overtaking occurs when more than two fluid components occupy the same position. Only the fluid components in the overtaking region are accelerated and escape the region.

The maximum energy that electrons can obtain from the resonance field is estimated by analyzing the electron plasma wavebreaking. The dynamics of wavebreaking was first analyzed by Dawson [9] and further developed by Albritton and Koch.[7, 10, 12] Before wavebreaking takes place, the electron motion can be described by a harmonic

oscillation equation with Poisson's equation. This description is valid as long as the fluid elements do not cross each other. As the oscillation develops, one can impose an overtaking condition to the electron fluid trajectory and calculate the electron energy at that moment. This energy gives the estimate of the accelerated electron energy and thus energy dissipation through wavebreaking.

The motion of an oscillating electron near the critical density is conveniently described via Lagrangian variables where the position z of a electron fluid is expressed in terms of its initial position z_0 and time t,

$$z(z_0, t) = z_0 + \sigma(z_0, t). \qquad \text{2-12}$$

The analysis assumes that 1) the ion fluctuations are negligible, 2) the driving electric field E_d is uniform over the oscillation, 3) density gradient, L_n around the resonance is linear, and 4) $\sigma \ll L_n$. Using conservation of electron number, $n(z, t)dz = n(z_0, 0)dz_0$ and Poisson's equation, $\partial E/\partial z = 4\pi e(N_i - n_e)$, the force equation of an electron is

$$\left.\frac{\partial^2 \sigma}{\partial t^2}\right|_{z_0} = -\frac{eE(x, t)}{m_e} \cong -\omega_{pe}^2(z_0, 0)\sigma - \frac{eE_d}{m_e}\sin(\omega_0 t)$$

whose solution is

$$\sigma = \frac{\chi L_n}{(2 + \delta)(1 + \delta)}\left[\sin(\omega_0 t) - \omega_0 t\frac{\sin(\delta\omega_0 t/2)}{\delta\omega_0 t/2}\cos(1 + \delta/2)\omega_0 t\right]. \qquad \text{2-13}$$

Here $\delta(z_0) \equiv \dfrac{\omega_{pe}(z_0)}{\omega_0} - 1$ is the detuning from resonance and $\chi \equiv -\dfrac{eE_d}{m_e\omega_0^2 L_n}$. Since only the secular growth of σ near the resonance (δ=0) is important for the maximum energy calculation, the fluid velocity at the exact resonant point $\delta = 0$ is

$$v = \frac{\partial \sigma}{\partial t} \to \frac{eE_d}{m_e}\frac{\sin(\omega_0 t)}{2}t \text{ as } \delta \to 0$$

Referring to Fig. 2-30 and Eq.2-12, the overtaking (or orbit crossing) occurs when fluid elements from different initial positions take the same position simultaneously, that is, $\partial z/\partial z_0 = 1 + \partial \sigma/\partial z_0 = 0$. With Eq.2-13, the overtaking time is $t_b \approx (8/\chi)^{1/2}/\omega_0$ and thus the maximum velocity is

$$v_p = (2v_d\omega_0 L_n)^{1/2}, \qquad\qquad\qquad 2\text{-}14$$

where $v_d \equiv eE_d/m_e\omega_0$ the electron quiver velocity in the driving field. This velocity is used to determine the maximum electron energy from overtaking.

When a plasma has a steep density gradient, the plasma dispersion relation obtains an additional convective term. This can be seen by solving equations of continuity and motion of electrons with keeping a derivative of the unperturbed electron density. Since it suffices to consider an electron motion in the direction of the density gradient (in the z direction) alone, the governing equations are

$$\frac{\partial n_e}{\partial t} + \frac{\partial n_e V_e}{\partial z} = 0 \qquad\qquad\qquad 2\text{-}15$$

and

$$\frac{\partial n_e V_e}{\partial t} + \frac{\partial n_e V_e^2}{\partial z} = -\frac{n_e eE}{m_e} - \frac{1}{m_e}\frac{\partial P_e}{\partial z}. \qquad\qquad\qquad 2\text{-}16$$

All the quantities have a standard meaning regarding to electrons. Assuming that only the density has an unperturbed term, that is, $n_e = n_0 + \tilde{n}_e$, $V_e = \tilde{V}_e$, $E = \tilde{E}$, and $P_e = \tilde{P}_e$ linearizes Eqs. 2-15 and 2-16.

$$\frac{\partial \tilde{n}_e}{\partial t} + \frac{n_0}{L_n}\tilde{V}_e + n_0\frac{\partial \tilde{V}_e}{\partial z} = 0 \qquad\qquad\qquad 2\text{-}17$$

$$n_e\frac{\partial \tilde{V}_e}{\partial t} = -\frac{n_0 e\tilde{E}}{m_e} - \frac{1}{m_e}\frac{\partial \tilde{P}_e}{\partial z}. \qquad\qquad\qquad 2\text{-}18$$

where the products of the perturbed terms are neglected. Using $\tilde{P}_e = T_e \tilde{n}_e$, Eq. 2-18 becomes,

$$n_e \frac{\partial \tilde{V}_e}{\partial t} = -\frac{e \, n_0 \tilde{E}}{m_e} - \frac{1}{m_e} T_e \frac{\partial \tilde{n}_e}{\partial z} .$$

2-19

Equations 2-18, 2-19 and Poisson's equation give a complete set of coupling equations,

$$i \, \omega \tilde{n}_e = n_0 \tilde{V}_e \left(\frac{1}{L_n} + i \, k \right)$$

$$n_e \omega^2 \tilde{V}_e = - k\omega \frac{T_e}{m_e} \tilde{n}_e + i \, \omega \frac{e \, n_0}{m_e} \tilde{E}$$

$$\partial \tilde{E} / \partial z = -4\pi e \tilde{n}_e.$$

Combining these three equations yields

$$\omega^2 = \omega_{pe}^2 + k^2 \frac{T_e}{m_e} + \frac{\omega_{pe}^2}{i \, kL_n}.$$

$\frac{i \, kT_e}{L_n m_e}$ term has been dropped compared to $k^2 \frac{T_e}{m_e}$ since $L_n > \frac{1}{k}$.

At the critical surface, $\omega = \omega_{pe}$, k gives the plasma wave decay factor due to the steep density gradient,

$$k = i \left(\frac{1}{\lambda_{De}^2 L_n} \right)^{1/3} ,$$

2-20

the result given by Ginzburg.[6] Here λ_{De} is the electron Debye length defined as $\sqrt{\frac{T_e}{4\pi n_e e^2}}$

. This decay factor gives an estimate of the spatial width of the resonantly enhanced field at the critical surface, $(\lambda_{De}^2 L_n)^{1/3}$. Comparing this width with the scale length yields the field enhancement factor of $\left(\frac{L_n}{\lambda_{De}} \right)^{2/3}$. As discussed in the next paragraph, the energy deposited into the resonance region is dissipated by the wave convection.

A similar result can be obtained by estimating the electric field amplitude of the harmonic oscillation of the electrons at the critical density driven by the p-polarized component of the incident laser electric field. As discussed in the previous section the z component of electric field E_z can be estimated by Ampere's law, Eq. 2-3 and the law of refraction, Eq. 2-8: $k(z)\sin\theta(z) = k_y = \dfrac{\omega}{c}\sin\theta_0$.

$$E_z = \frac{\sin\theta_0 B(z)}{\varepsilon(z)} \cong \frac{E_d(z)}{\varepsilon(z)} \ .$$

Here E_d is the component of laser field that drives electrons along the density gradient. From the result of the previous section, $E_d = \eta_t E_0$, the electric field of laser in vacuum. The penetration strength η is approximately 0.2 (see Fig. 2-3). Without a limiting mechanism E_z could grow infinitely at the critical surface where $Re(\varepsilon) = 0$. Since the driven electric field E_z is proportional to electron displacement, E_z can replace the plasma electron density in a forced harmonic (plasma wave) equation. E_z can then be calculated by solving a plasma wave equation.

$$\left[\frac{\partial^2}{\partial t^2} + \omega_0^2\left(1 - \frac{(z - z_{cr})}{L_\eta}\right) - 3v_e^2\frac{\partial^2}{\partial z^2}\right] E(z, t) = -\omega_0^2 E_d \sin\omega_0 t. \qquad 2\text{-}21$$

Wave convection is particularly important in the case of short scale length plasmas. Here v_e is the electron thermal velocity and the plasma density gradient is approximated to be locally linear. The left and right hand sides correspond to a natural harmonic oscillation of the plasma and the driving force due to the incident laser field, respectively. As can be seen from the plasma wave dispersion relation, Eq. 2-20, plasma waves decay as they propagate out of the resonance region. Therefore, a physically acceptable solution [18] is evanescent as $z \to \pm \infty$ and given by

$$E(z, t) = \left(\frac{\omega_0^2 L_\eta^2}{3v_e^2}\right)^{1/3} E_d \, Re[I\exp(i\omega_0 t)],$$

with

$$I(\chi) = \int_0^\infty d\xi \exp(i\xi^3/3 - i\chi\xi),$$

where $\chi \equiv z(\omega_0^2/3v_e^2 L_n)^{1/3}$ and $\chi = 2.6$ gives the maximum value of $I = 1.7$. Thus the peak electric field E_p is

$$E_p = 1.2\left(\frac{\omega_0 L_n}{v_e}\right)^{2/3} E_d = 1.2\left(\frac{L_n}{\lambda_{De}}\right)^{2/3} E_d. \qquad 2\text{-}22$$

The Eq. 2-22 gives the amplitude of the enhanced electrostatic field that is limited by the plasma wave dispersion and can be compared with the field strength given by wavebreaking, Eq. 2-14. Comparing Eqs. 2-14 and 2-22 and using the driving field amplitude in terms of the vacuum field amplitude obtained in the previous section, $E_d = \eta_t E_0$, the criterion for the cold plasma wavebreaking is

$$\frac{v_0}{v_e} \geq 1.4\left(\frac{\lambda_e}{L_n \eta_t^3}\right)^{1/3}. \qquad 2\text{-}23$$

Equation 2-23 gives the threshold laser intensity of the plasma wave convection limit at a given electron temperature. When the plasma wave convection limits the amplitude of enhanced field, the ponderomotive force due to the sharp field gradient accelerates the electrons to its potential. The number of electron accelerated in the processes also distinguishes the mechanism. The ponderomotive force accelerated the entire population of electrons to its potential energy, while wavebreaking only accelerated those electrons in the overtaking region.

II-4 The ponderomotive potential and wavebreaking for energetic electron acceleration

In the study of laser-plasma interactions, two types of forces are of interest and important to various phenomena in plasma. They are thermokinetic forces due to

gasdynamic pressure of plasmas and electrodynamic forces of a nonlinear type. The latter has direct importance to laser-plasma interactions. This nonlinear electrodynamic force is, when exerted on plasmas, commonly called ponderomotive force and exists, either for an electromagnetic or electrostatic field, whenever the field has gradient. Physically this force depends on the spatial variation of the amplitude of the electron oscillations within the field, that is, the $(E \bullet \nabla)E$ term for electrostatic field or $V \times B$ term for electromagnetic field.

When an electron oscillates in a nonuniform electromagnetic or electrostatic field, it acquires a net drift during many oscillations. Physically the electron is accelerated more in the strongest field region than in weaker field region and does not return to the original position during one oscillation. This displacement accumulates over many oscillations and results in net drift. The driving force for the drift is proportional to the gradient of the field and expressed in terms of the potential, ϕ_{pond}, by

$$\nabla \phi_{pond} = - \frac{e^2}{4m\omega^2} \nabla E_s^2 .$$

The electron eventually acquires a kinetic energy equal to the oscillation energy in the field. This drift is called ponderomotive acceleration. The electrons oscillating in the resonantly enhanced field are accelerated by this process because of the steep gradient of the field structure.

The ponderomotive acceleration of plasma [13] due to the resonantly oscillating field at the critical density contrasts with wavebreaking heating in terms of the spectra and number of electrons produced through the processes. The ponderomotive force accelerates an electron to a definite velocity determined by its potential during many oscillations of the fields; therefore, the electron spectrum due to this process is expected to be a shifted Maxwellian (beam-like) distribution. The beam-like distribution or a bulk acceleration of plasma has been observed in a series of microwave plasma

interaction experiments [14, 15] and numerical simulations using a particle code on EM wave conversion to ES wave. The wavebreaking process, on the other hand, randomly distributes the collapsing wave energies among electrons.[16] The number of electrons accelerated in the ponderomotive potential, as the second distinctive point, is much larger than that of wavebreaking process since all the particles in the resonance region can participate in the process when $E^2/8\pi n_e k_B T_e > 1$, the condition for which the oscillatory energy is larger than the thermal energy.

The ponderomotive force can be derived from an electron force equation,[17]

$$m_e \frac{dv_e}{dt} = -e\left\{ E(x, t) + v \times B(x, t) \right\}, \qquad \text{2-24}$$

where $E(x, t)$ is assumed to have a time dependence, $E_s(x)\cos\omega t$ with E_s bearing the spatial variation of E. The first order solution of Eq 2-24 is

$$m_e \frac{dv_{e1}}{dt} = -eE_s(x_0)\cos\omega t,$$

and thus

$$v_{e1} = -\frac{e}{m\omega}E_s(x_0)\sin\omega t, \qquad \text{2-25}$$

$$\delta x_1 = \frac{e}{m\omega^2}E_s(x_0)\cos\omega t. \qquad \text{2-26}$$

B_1 is given by Faraday's law,

$$B_1 = -\frac{1}{\omega}\nabla \times E_s(x_0)\sin\omega t. \qquad \text{2-27}$$

E_s is expanded, up to second order, about $x = x_0$,

$$E_s(x) \approx E_s(x_0) + (\delta x_1 \bullet \nabla)E_s(x_0).$$

The second order of Eq 2-24 is then

$$m_e \frac{dv_{e2}}{dt} = -e \left\{ (\delta x_1 \bullet \nabla) E_s(x_0) + v_{e1} \times B_1 \right\}.$$

Substituting Eqs 2-25, 2-26, and 2-27 and averaging over one period $1/\omega$ yield

$$m \left\langle \frac{dv_{e2}}{dt} \right\rangle = \frac{e^2}{2m\omega^2} \left\{ (E_s \bullet \nabla) E_s + E_s \times (\nabla \times E_s) \right\} = -\frac{e^2}{4m\omega^2} \nabla E_s^2 \qquad 2\text{-}28$$

This is the ponderomotive force per electron that is eventually transferred to ions through ambipolar fields.

The ponderomotive acceleration of electrons, in the present work, is shown to be a dominant mechanism in the present plasma condition whereas wavebreaking (electron overtaking) in a resonantly oscillating plasma wave has been regarded as a mechanism for high energy electron generation from the critical surface in long scale length plasmas.[7, 18] Therefore, it is necessary to examine some of the features of the electrons produced by the wavebreaking process to distinguish wavebreaking from the ponderomotive acceleration.

A resonantly oscillating plasma wave at the critical surface accelerates an electron to superthermal energies. This acceleration is determined by the electric field amplitude of the plasma wave. The plasma temperature has important effects on the amplitude of the field as shown in the previous section. When a plasma is cold, the plasma wave amplitude can grow until wavebreaking occurs and the breaking wave can abruptly give energies to electrons and ejects them out of the resonance region. The electrons that participate in wavebreaking take energy away from the resonance region and the growth of the field saturates. The plasma wave amplitude is thus determined by the wavebreaking amplitude, and the number of electrons accelerated is limited to a small fraction of electrons in the critical region because, as soon as overtaking occurs, wave energy is taken away by those accelerated electrons and growth of wave saturates (see Fig. 2-10). When a plasma is warm, on the other hand, thermal convection extends the spatial width of resonantly oscillating field and reduces the field amplitude.[11, 19]

Electrons are then accelerated by the ponderomotive force of the plasma wave field. Since electrons are accelerated in the ponderomotive potential as they oscillate in the resonance field, a larger portion of electrons is expected to participate in the process. Therefore, the measurement of the number of electrons accelerated from the resonance region can distinguish between wavebreaking and the ponderomotive acceleration.

A number of numerical and theoretical studies [16, 18-20] have shown that wavebreaking produces near Maxwellian electron distribution superimposed on a cold electron distribution and so is measured by a continuum x-ray spectroscopy.[21-24] On the other hand, the ponderomotive force accelerates particles during many oscillations and thus every electron is accelerated to a given energy.

II-5 Isothermal expansion of Plasma

Accelerated electrons lose their energy either by collisional or noncollisional processes. The efficiency of the collisional process decreases as the electron energy increases due to the v_e^{-3} (v_e is the electron velocity) dependence of the collision frequency. Therefore, the high energy electrons tend to leave stationary ions before losing energies collisionally and create an ambipolar field due to the charge separation. As this field builds up, the ions are accelerated and energy transfer from the electrons to ions occurs. Thus the high energy electrons tend to lose more energy by accelerating ions than by collisions. Through this process, the accelerated ions (so-called fast ions) obtain large fraction of absorbed energy that has been initially absorbed by the high energy electrons. This ion blowoff can be detected as an ion current (density) and serves as an important plasma diagnostic.

An ion current trace can provide information about the target plasma such as total particle number and energy, and the temperature of the electrons that accelerate ions. Estimating the total number and energy is rather straight forward; although, the estimation of electron temperature requires the analysis of the ion-velocity distribution

based on an isothermal plasma expansion model. The model assumes: (1) isothermal electron distribution, (2) charge neutrality, (3) two fluid components made of hot electrons and relatively cold ions ($T_i \approx 0$), (4) planar one dimensional expansion, (5) negligible collisions, and (6) Boltzman equilibrium. An isothermal expansion model is physically plausible because (1) thermal conduction in the plasma is sufficiently rapid to suppress large temperature gradients and (2) heat conduction into the cold dense plasma above critical surface can be significant on the picosecond time scale.[25, 26] The scale length of plasma is expected to be longer than Debye length and charge between electrons and ions always balances. The effect of cold electrons on the fast ion acceleration can be neglected since their pressure is much smaller than that of the hot electrons. The temperature of the ions is also assumed to be low so that their pressure can be neglected. In the collisionless limit, the analysis is very simple and the plasma is expected to be collisionless for the high electron energies in present work. Since electron response time $1/\omega_{pe}$ is much shorter than the time scale of plasma expansion, the electron fluids are always in equilibrium with the electrostatic potential, i.e., a Boltzmann equilibrium.[27]

The isothermal expansion model was first developed by Gurevich $et.al.$[28] and has been a basic model in various studies.[29-32] The analysis uses a set of three equations: continuity and force equations of ion fluids and Boltzmann equation,

$$\frac{\partial n_i}{\partial t} + \frac{\partial}{\partial x}(n_i V_i) = 0 \qquad\qquad 2\text{-}29$$

$$\frac{\partial V_i}{\partial t} + V_i \frac{\partial V_i}{\partial x} = \frac{Z_i e}{M_i} E \qquad\qquad 2\text{-}30$$

$$n_e = n_0 \exp\left(- \frac{e\phi}{kT_e}\right) \qquad\qquad 2\text{-}31$$

Here V_i, E (ϕ) and T_e are ion velocity, the electric field (potential) and electron temperature. Using $E = -(\partial\phi/\partial x)$, Eqs. 2-30 and 2-31 can be combined, yielding

$$\frac{\partial V_i}{\partial t} + V_i \frac{\partial V_i}{\partial x} = \frac{-Z_i k T_e}{n_e M_i} \frac{\partial n_e}{\partial x} .$$

2-32

The Eqs 2-29 and 2-32 are transformed by introducing a similarity variable $\xi = x/t$ and using charge neutrality $n_e = Z n_i$

$$(V_i - \xi)\frac{\partial n_i}{\partial \xi} + n_i \frac{\partial V_i}{\partial \xi} = 0$$

$$(V_i - \xi)\frac{\partial V_i}{\partial \xi} = \frac{-Z_i k T_e}{n_i M_i} \frac{\partial n_i}{\partial \xi} .$$

2-33

Eliminating $\partial n_i/\partial \xi$ and $\partial V_i/\partial \xi$ gives

$$\frac{x}{t} - V_i = -C_s ,$$

where $C_s \equiv (Z_i k T_e/M_e)^{1/2}$ and a solution for outward expansion has been chosen. Substituting this expression into Eq.2-33 yields

$$\frac{\partial V_i}{\partial \xi} = -\frac{C_s}{n_i} \frac{\partial n_i}{\partial \xi} ,$$

which can be integrated to give

$$V_i(\xi) = -C_s \ln\left(\frac{n_i}{n_{i0}}\right) \text{ or}$$

$$n_i(\xi) = n_{i0} \exp\left(-\frac{V_i}{C_s}\right) ,$$

where n_{i0} corresponds to unperturbed ion density that assumes infinite number of ions are provided by the bulk target. To relate this equation to observable quantity, the ion velocity distribution, it is differentiated in terms of V_i,

$$\frac{dn_i}{dV_i} = -\frac{n_{i0}}{C_s} \exp\left(-\frac{V_i}{C_s}\right).$$

2-34

Thus the slope of velocity distribution (when plotted in a semilog scale) gives an estimate of electron temperature through C_s.

REFERENCES

1   W. Kruer, *The Physics of Laser Plasma Interactions* (Addison-Wesley, Redwood City, 1987).

2   V. L. Ginzburg, "Section 19. Oblique incidence of waves on a layer," in *Propagation of Electromagnetic Waves in Plasma*, edited by W. L. Sadowski and D. M. Gallik. (Gordon and Breach, 1961) p. 364-376.

3   H. M. Milchberg and R. R. Freeman, "Light absorption in ultrashort scale length plasmas," J. Opt. Soc. Am. B **6**, 1351 (1989).

4   J. C. Kieffer, et al., "Absorption of an ultrashort laser pulse in very steep plasma density gradients," IEEE J. Quantum Electron. **25**, 2640 (1989).

5   R. J. Faehl and N. F. Roderick, "Swelling effects of electromagnetic waves near the critical density," Phys. Fluids **20**, 1279 (1977).

6   V. L. Ginzburg, "Section 20. A special characteristic of an electromagnetic wave field propagating in an inhomogeneous isotropic plasma. The interaction of electromagnetic and plasma waves," in *Propagation of Electromagnetic Waves in Plasma*, edited by W. L. Sadowski and D. M. Gallik. (Gordon and Breach, 1961) p.377-403.

7   J. Albritton and P. Koch, "Cold plasma wavebreaking: Production of energetic electrons," Phys. Fluids **18**, 1136 (1975).

8   D. D. Meyerhofer, "The interaction of high intensity lasers with short scale-length plasmas," in the Abstracts of *21st Annual Anomalous Absorption Conference*, (Banff, Alberta, Canada, 1991).

[9] J. M. Dawson, "Nonlinear electron oscillations in a cold plasma," Phys. Rev. **113**, 383 (1959).

[10] P. Koch, "Lagrangian description of phase space flow: Turbulent heating," Phys. Fluids **16**, 651 (1973).

[11] D. W. Forslund, J. M. Kindel, K. Lee, E. L. Lindman and R. L. Morse, "Theory and simulation of resonant absorption in a hot plasma," Phys. Rev. A **11**, 679 (1975).

[12] P. Koch and J. Albritton, "Electron and ion heating through resonant plasma oscillations," Phys. Rev. Lett. **32**, 1420 (1974).

[13] H. Hora, "The nonlinear force of electromagnetic laser-plasma interaction," in *Laser Interaction and Related Phenomena*, edited (1977) 4B: p.841.

[14] R. L. Stenzel, A. Y. Wong and H. C. Kim, "Conversion of electromagnetic waves to electrostatic waves in inhomogeneous plasmas," Phys. Rev. Lett. **32**, 654 (1974).

[15] A. Y. Wong and R. L. Stenzel, "Ion acceleration in strong electromagnetic interactions with plasmas," Phys. Rev. Lett. **34**, 727 (1975).

[16] B. Bezzerides, S. J. Gitomer and D. W. Forslund, "Randomness, Maxwellian distribution, and resonance absorption," Phys. Rev. Lett. **44**, 651 (1980).

[17] F. F. Chen, *Introduction to Plasma Physics*, (Plenum Press, New York, 1974).

[18] K. Estabrook and W. L. Kruer, "Properties of resonantly heated electron distributions," Phys. Rev. Lett. **40**, 42 (1978).

[19] K. G. Estabrook, E. J. Valeo and W. L. Kruer, "Two-dimensional relativistic simulations of resonance absorption," Phys. Fluids **18**, 1151 (1975).

[20] K. A. Brueckner, "Fast-electron production in laser-heated plasmas," Nucl. Fusion 17, 1257 (1977).

[21] J. F. Kephart, R. P. Godwin and G. H. McCall, "Bremsstrahlung emission from laser-produced plasmas," Appl. Phys. Lett. 25, 108 (1974).

[22] V. W. Slivinsky, H. N. Kornblum and H. D. Shay, "Determination of superthermal electron distributions in laser-produced plasmas," J. Appl. Phys. 46, 1973 (1975).

[23] P. G. Burkhalter, F. C. Young, B. H. Ripin, J. M. McMahon, S. E. Bodner, R. R. Whitlock and D. J. Nagel, "Continuum x-ray emission spectra from laser produced plasmas at $10^{16}W/cm^2$," Phys. Rev. A 15, 1191 (1977).

[24] G. D. Enright, N. H. Burnett and M. C. Richardson, "X-ray emission characteristics of plasmas created by a high-intensity CO_2 laser," Appl. Phys. Lett 31, 494 (1977).

[25] D. G. Stearns, O. L. Landen, E. M. Campbell and J. H. Scofield, "Generation of ultrashort x-ray pulses," Phys. Rev. A 37, 1684 (1988).

[26] O. L. Landen, D. G. Stearns and E. M. Campbell, "Measurement of the expansion of picosecond laser-produced plasmas using resonance absorption profile spectroscopy," Phys. Rev. Lett. 63, 1475 (1989).

[27] S. P. Sarraf, "Effects of prepulse radiation on non-thermal (>10keV/Z) ions in laser produced plasmas," Ph. D Thesis, (University of Rochester, 1980).

[28] A. V. Gurevich, L. V. Pariĭskaya and L. P. Pitaevskiĭ, "Self-similar motion of rarefied plasma," Soviet Phys. JETP 22, 449 (1966).

[29] J. E. Crow, P. L. Auer and J. E. Allen, "The expansion of a plasma into a vacuum," J. Plasma Phys. 14, 65 (1975).

[30] L. M. Wickens and J. E. Allen, "Ion emission from laser-produced plasmas with two electron temperature," Phys. Rev. Lett. 41, 243 (1978).

[31] A. V. Gurevich, L. V. Pariĭskaya and L. P. Pitaevkiĭ, "Ion acceleration upon expansion of a rarefied plasma," Sov. Phys. JETP **36**, 274 (1973).

[32] R. A. London and M. D. Rosen, "Hydrodynamics of exploding foil x-ray laser," Phys. Fluids **29**, 3813 (1986).

CHAPTER III

Experiments

III-1 Laser system

The laser system used in the experiment is an Nd-glass laser using a CPAC (Chirped Pulse Amplification and Compression) scheme to produce picosecond high power laser pulses.[1-3] Glass lasers are suitable for high power applications because of their high energy storage capability. Using the CPAC scheme,[1] the system delivers >100 GW of laser power with a relatively compact configuration, shown in Fig. 3-1. The system is seeded by a mode-locked YLF oscillator that generates a 100-MHz, 55-ps pulse train. The pulse train goes through an 800-m singlemode optical fiber and expands its bandwidth from 0.3Å to approximately 40Å due to self-phase modulation. At this stage, each pulse is frequency chirped in time and further stretched to an approximately 300-ps duration by a double pass expanding grating pair. Since the resulting short-pulse characteristics strongly depend on the quality of the chirping, both compressed pulse shape and the bandwidth at this stage are monitored by a cw autocorrelator and a spectrometer, respectively. A single 300-ps pulse is selected and safely amplified up to a few hundreds mJ with the Nd:phosphate-glass amplifier chain. The pulse is compressed to a 1-ps duration by a compressing grating pair. Several additions and improvements to the system have been made to meet the picosecond laser-plasma interaction experiments[3] since its first construction.[1] A 16-mm rod amplifier (RA16) has been added to boost the maximum output power to 0.2 TW. Pockels cells and polarizers between the amplifiers function as isolators and reduce cavity generated pre- or post pulse (~10 ns separation) energy by ~1/1000 per Pockels cell.

Faraday rotator

Double-pass expanding
grating pair

SF1

Mechanical
shutter

Regen cavity

RA9

Spectrometer

YLF oscillator

SF2

cw autocorrelator

EWP

SF3

SF4

Optical fiber
(Self-phase modulator)

SF5

RA16

Polarizer

Pockels cell

Rod amplifier

Wave plate

Spatial filter

Double-pass Compressing
grating pair

Saturable absorber cell

Energy/intensity monitors
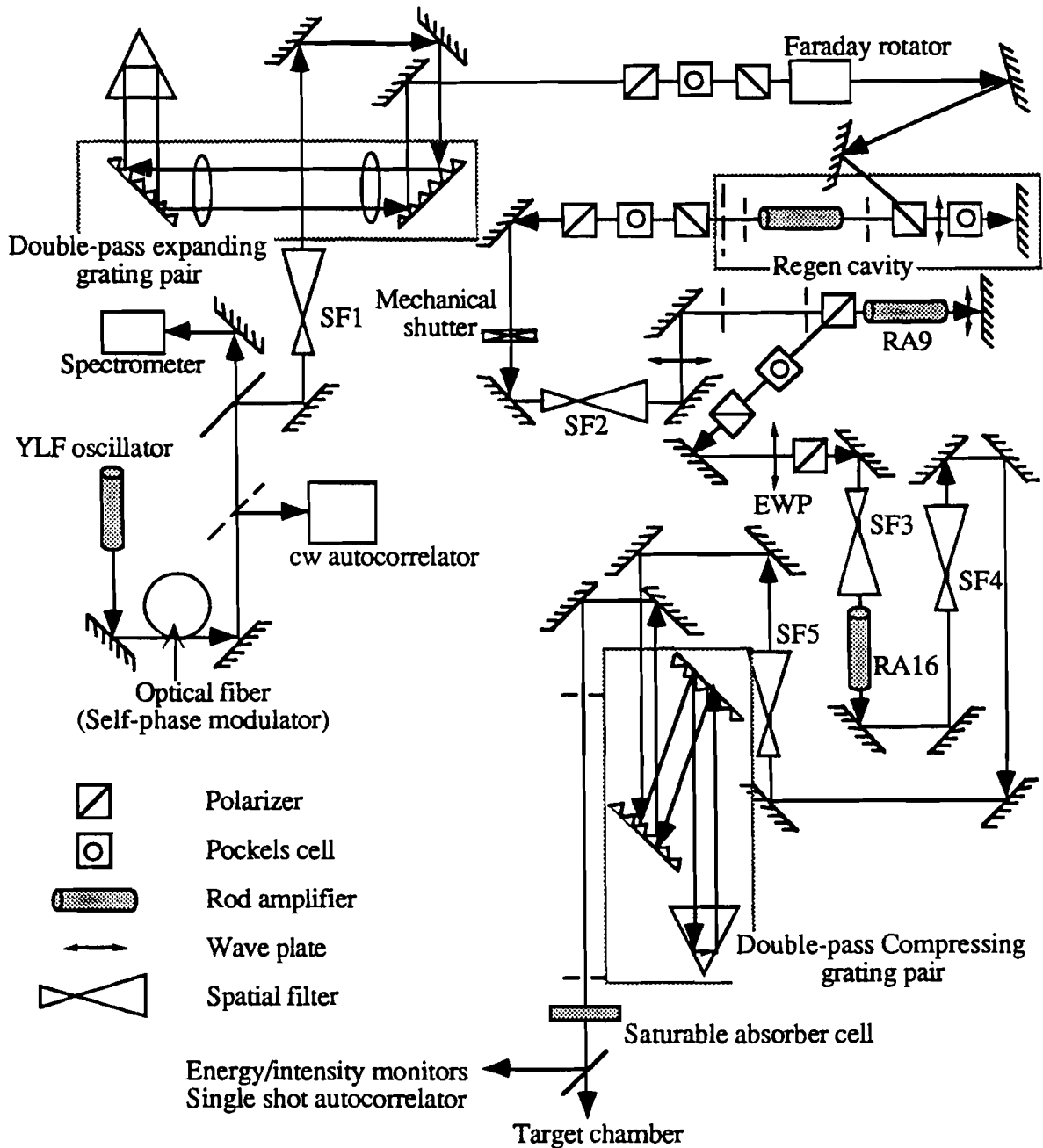Single shot autocorrelator

Target chamber

Fig. 3-1   Schematic of the glass laser system with CPAC used for the
experiments.   Various monitors and optical switches ensure that
desirable short pulses irradiate target.

There are inherent non-linearly chirped portions on both sides of the linear chirp

produced by the optical fiber resulting in satellite pulses accompanying the main

picosecond pulse. By matching the gain center of the regenerative amplifier to the center of the chirping, the gain narrowing in the amplifier shapes the pulse spectrum to a Gaussian and suppresses the non-linear chirping.[4] This gain matching can reduce the satellite pulse power 10^{-3} below the main pulse as well as the pulse wings that are caused by any deviations from the Gaussian spectrum. The satellite pulses are further suppressed by using a saturable absorber cell after the compression gratings. Two spatial filters have been added to eliminate hot spots and unfocusable energy by cutting off distorted wave fronts and to compensate for any de-collimating effects through the system. A pair of $\lambda/2$ plates and polarizer placed between the RA9 (9 mm rod amplifier) and RA16 (16 mm amplifier) are used to adjust the system output energy since optical filters might destroy the chirping or pulse duration. The grating expander and compressor have been converted to a double-pass configuration to compensate for the astigmatism introduced by a single-pass geometry. A single shot autocorrelator consisting of a $LiIO_3$ crystal and a linear photodiode array (Reticon RC105) measures the output pulse duration. These features are crucial for the reliability of the laser-plasma experiments as well as for laser system maintenance.

III-2 Target and irradiation system

Figure 3-2 shows schematically the target irradiation system and the vacuum target chamber. The focusing optics consist of four elements of an aspheric lens (combined thickness of about 6 cm) providing an effective f/# of 5.6 when a 3 cm diameter beam is used. The polarization of the laser is controlled by a $\lambda/2$ wave plate in front of the chamber. The alignment of targets and other diagnostics use the coaligned He-Ne laser. The pressure in the target chamber was kept below 10^{-5} Torr to avoid charge exchange between plasma ions and ambient gas atoms.

The targets used for the experiments are films of Al deposited on clean microscope glass plates. The thickness of the Al is 6000 Å thicker than the expected ablation depth,

~1000 Å, which was verified by the experiments. Targets are stored in a vacuum container to avoid any Al surface contamination and oxidization.

There are several reasons that make Al a favorable material for the target.

1) Al is the one of the materials that have been studied extensively in laser produced plasma research and related fields; thus a great deal of data is available.

2) Al has a moderate atomic number and serves as a good starting material for future material surveys of the same kind of investigations.

3) Al provides high optical quality targets when coated on a smooth surface that is a vital requirement for studying high contrast ultra-short laser-plasma interactions.

Additionally the use of pure Al targets excludes the complexity of the ion measurements that would have had to be done in the case of a multi-species ion target.

Targets are mounted on a translation stage and repositioned by twice the size of the laser crater after each shot so that every laser shot is on a fresh surface. The target support structure is isolated electrically from the ground. The size of the target accommodates ~100 shots when each shot is separated by approximately 1 mm. The incident angle of the laser (angle between target normal and laser axis) is 55° for most of the experiments.

One of the important experimental parameters is the polarization of the laser. To examine the effects of the polarization on the interaction, the $\lambda/2$ wave plate is adjusted to some intermediate settings between s- and p-polarization while the total laser energy is kept constant. A parameter, p-polarized intensity I_p, is defined corresponding to the p-polarized component of the laser electric field

$$I_p = I_0 \cos^2 \phi_{pol} \qquad\qquad 3\text{-}1$$

where ϕ_{pol} is an angle between the electric field vector and the pure p-polarized vector (in the plane of incidence).
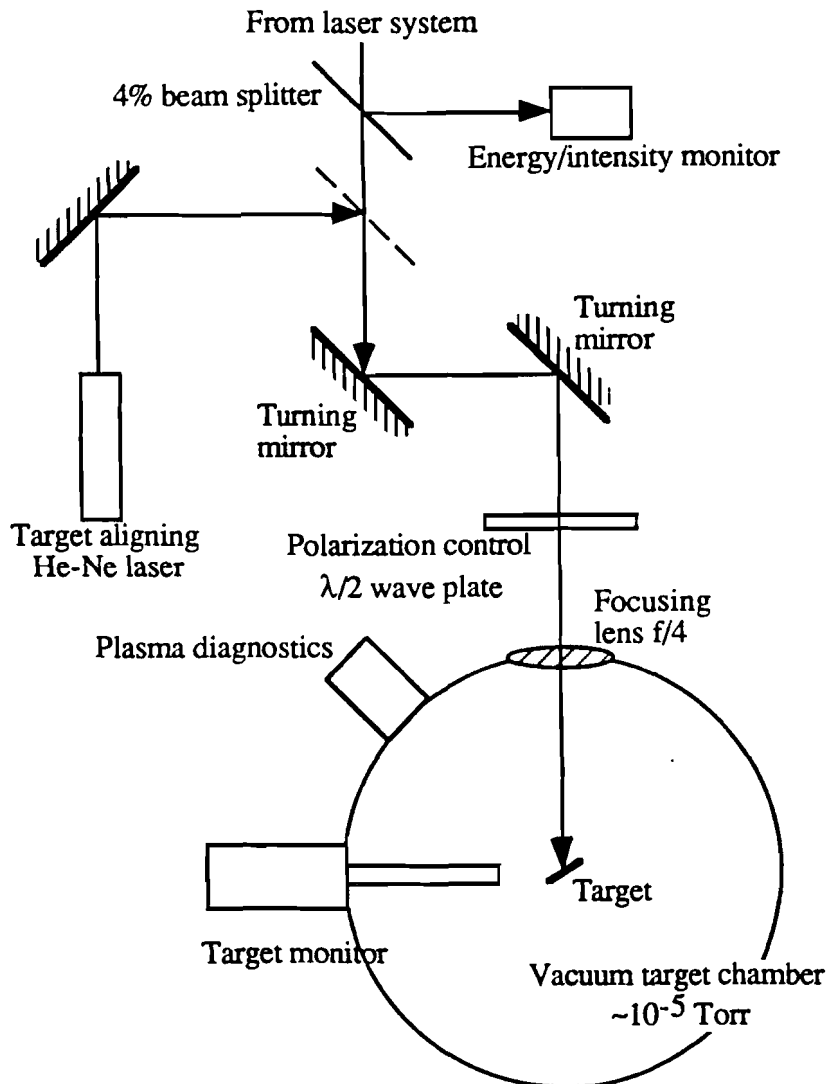
Fig. 3-2   Target alignment and irradiation system. The laser is focused into a
vacuum target chamber through f/5.6 optics. A coaligned He-Ne
laser and a target monitor align the targets at the focus of the laser.
The polarization of the laser is controlled by a $\lambda/2$ wave plate.

III-3 Pulse characteristics

Pulse characterization is classified into two kinds of measurements: off-line and on-line measurements. The off-line characterizations were performed in separate experiments before the plasma experiments and consist of two measurements: temporal

pulse shape and spatial profile of focused beam. The temporal pulse shapes with a dynamic range of 10^5 were measured with an autocorrelator,[3],[5] results of which are shown in Figs. 3-3. Figures 3-3-a and b show the pulse shape with and without the satellite emission. The measurements were done by sampling a part of the beam into an autocorrelator. Each data point is obtained by averaging ten laser shots.

When the gain center of the amplifier is matched to the chirped pulse center frequency, the system delivers a nearly Gaussian 1.6 ps pulse accompanied by prepulse and postpulse, satellite pulses, peaked at ± 100 ps from the main pulse with a 10^3 power contrast as shown in Fig. 3-3-a. The prepulse intensity is $10^{12} \sim 10^{13}$ W/cm^2 when focused on targets and exceeds the breakdown threshold of solids resulting in a preformed plasma before the main pulse arrives. This condition will be referred to as a "low intensity contrast case" in the following discussion. The satellite pulses are reduced by the saturable absorber (Kodak Q-switching dye #9860 with $\sim 5 \times 10^{-5}$ M in nitrobenzene solvent contained in a 1-cm thick cell) located after the compression grating pair for high contrast interaction experiments. With the saturable absorber, the intensity contrast increases to more than 10^5, the dynamic range of the measurement limited by a green light produced by a single beam in the autocorrelator (see Fig.3-3-b). The main pulse width is also shaped to 0.9 ps that is taken into account in intensity calculations. This high intensity contrast ensures that the prepulse intensity is, when focused, below the break down threshold of metals ($\sim 10^{11}$ W/cm^2).[6] This irradiation condition will be referred as a "high contrast case."

a Low contrast pulse
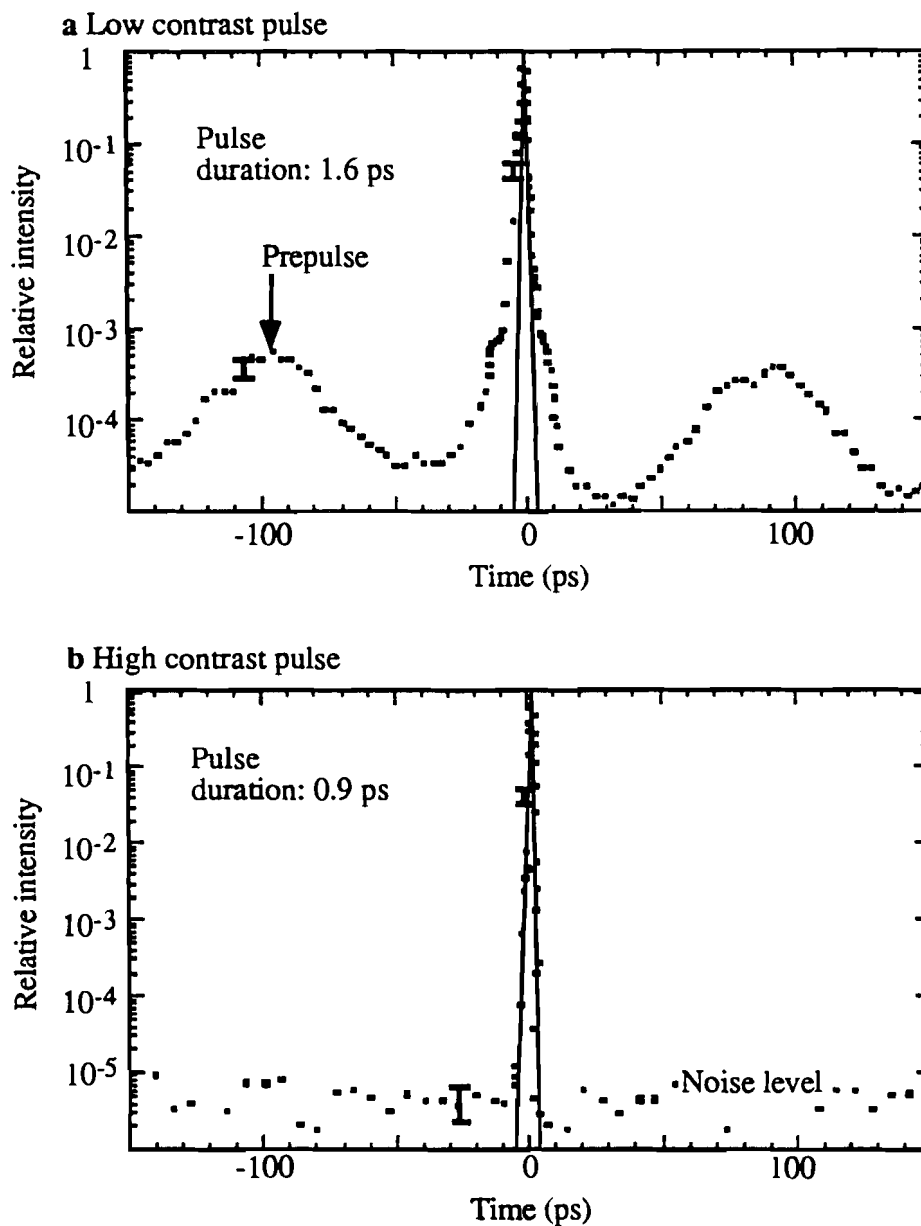

b High contrast pulse

Fig. 3-3   Laser pulse shape measured by an autocorrelator. a) Without saturable absorber the main picosecond pulse is accompanied by two satellite pulses. b) With saturable absorber the intensity contrast improves to greater than 10^5.

The focused spatial beam profile, the second off-line beam characterization, was measured at two places: far field and inside the target chamber. A far field pattern was obtained by a 200-cm focal length lens directly exposing infrared photographic films. The 200-cm lens yields a focused beam size much larger than the film resolution. The measured beam size was found to be about three times diffraction limited focus of Gaussian beam profile. The focused beam spot inside the target chamber is imaged with a certain magnification and compared with the far field pattern. Both measurements were found to agree to within 15%. A typical image of the focused spot is shown in Fig. 3-4, which was taken inside the target chamber. No hot spots in the focused beam have been observed from these measurements (see Fig. 3-4). Since the far field diagnostic can be executed relatively easily, once the comparison has been done the far field measurement was used as a primary beam spot diagnostic and conducted as necessary.

The magnification of the target chamber imaging system is measured with a reference target (10-μm diameter glass stalk). The measurement also gives the resolution of the system to be better than 3 μm. The beam spot size changes with and without the saturable absorber. The measurements obtained 30$\pm$4 and 24$\pm$3 μm beam diameters with (high contrast case) and without (low contrast case) the saturable absorber, respectively. This difference is probably due to the alteration of the beam divergence and wave front quality and/or the variation of the beam diameter. These dimensions were calculated by dividing the total energy on the spot by a peak energy density (areal density) on the film. These beam diameters thus correspond to an effective area, A_{eff} defined by

$$A_{eff} \equiv \{ \text{total laser power} \} / \{ \text{peak intensity} \}.$$

The effective area is used to calculate the laser intensity, by the formula $I_0 = E_L \cos\theta_{inc}/(A_{eff}\, \tau_L)$, where θ_{inc} is the angle of incidence. E_L and τ_L are the measured

laser energy and pulse width calculated by fitting a Gaussian to the autocorrelation traces (see Figs. 3-3).
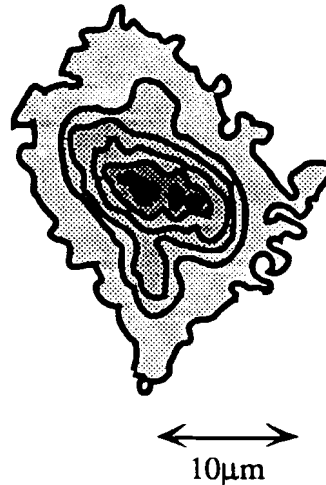

10μm

Fig. 3-4   Isoenergy contour of focused laser spot taken inside the target chamber.   The highest contour surrounding the black area corresponds to 85% of the peak value. The contours correspond to 15% step.

This measurement also found the beam Rayleigh range to be 200 μm. This long Rayleigh range is about five times longer than effective spot size of 42 μm (beam diameter/$\cos\theta_{inc}$) when the angle of incidence is 55° (see Fig. 3-5). This ensures that the targets are irradiated by nearly plane waves in spite of the fast optics (nominal f/#=5.6) on the chamber. Therefore polarization mixing and the ambiguity of incident angles are negligible. Imaging of the focused beam was also used to find the focusing position of the laser by locating the reference target at the object plane of the imaging system. It was also found that the focus position shifts by ~1 mm depending on whether the saturable absorber is used or not. Thus the target alignment was done accordingly.

The 6-cm total thickness of focusing optics and the maximum laser intensity of 10^{10} W/cm^2 at the lens correspond to a B integral of approximately 1 suggesting no significant distortion effects [7] present. Therefore, although the spot size measurements were done with reduced laser energies according to the film sensitivity, they represent the focusing characteristics of the full system operation.

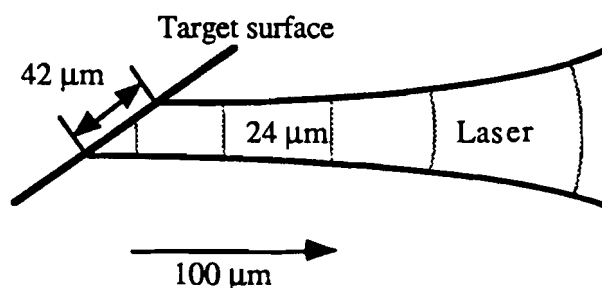Target surface

42 μm

24 μm   Laser

100 μm

Fig. 3-5   Target irradiation geometry at the best focus of the laser. The effective spot size 42 μm is short compared with the Rayleigh range of the beam and the target is expected to be irradiated by planar wave fronts.

The on-line pulse diagnostics include the single shot and cw autocorrelator [8, 9] for pulse width measurements, a spectrometer for pulse chirping monitoring and an energy/intensity monitor. The first three diagnostics are semi-on-line, that is, the laser pulses have to be intercepted by mirrors for those diagnostics to operate. However, these diagnostics are executed during the experiments as necessary. Both autocorrelators are based on the first order autocorrelation and thus any asymmetric structures of the pulse are lost in the measurement. In spite of this effect and poor dynamic range (of an order of magnitude), the diagnostics provide sufficient dynamic range of the main pulse shape during experiments. The spectrometer along with the cw autocorrelator monitor the characteristics of the chirped pulse out of the oscillator, since

any thermal drifts affecting the power output of the oscillator degrade the desirable spectral chirping. Two PIN photodiodes each filtered by an RG1000 (infrared light band-pass filter) and KG5 (green light band-pass filter), respectively, consist of the energy/intensity monitors which are fully on-line and operate on a shot by shot basis. The intensity monitor is based on the fact that the second harmonic efficiency is proportional to the fundamental intensity.[8, 9] The data is acquired by CAMAC system and integrated with other plasma data. The energy monitor is calibrated against an absolute energy measurement inside the target chamber.

III-4 Plasma diagnostics

Laser energy incident on a plasma is partially reflected and partially absorbed. The absorbed energy eventually dissipates in the form of electron, ion and x-ray energy. The characteristics of laser-plasma interactions reflect the ways in which the absorbed energy is carried away from the plasma by these mechanisms. Thus, the distribution of absorbed energy among the carriers provides a good measure of interaction characteristics. The measurements of the energy distribution use a number of diagnostics including an integrating sphere, charge collectors, magnetic electron analyzer, and K-edge filtered x-ray detectors. The integrating sphere measures the overall absorption of laser light. Charge collectors detect the ion current, which can be translated to the number of ions with the knowledge of ion charge distribution and thus used to estimate the energy absorbed by electrons that initially accelerated the ions. Absorbed energy converted to electrons can be measured also by either electrons directly or x-rays that are excited by electrons in the form of bremsstrahlung and K_α emissions. These diagnostics will be described in the following sections.

In short scale length plasmas, the resonantly enhanced laser electric field is expected to dominate the absorption process and generate high energy particles. In this process, electrons are accelerated directly and then quickly dissipate their energies into x-rays

through collisions and/or into ion kinetic motion through an ambipolar field (collisionless process). Furthermore the characteristics of electrons such as trajectory and energy distribution are subject to target potential [10] and self generated magnetic fields.[11] Therefore, even though it seems straightforward to measure electrons to characterize the interaction, the measurements are less reliable because the results are less direct and accurate interpretations are usually difficult. X-ray measurements have been proven to be a reliable diagnostic to characterize laser-plasma interactions in terms of electron spectrum and plasma parameters such as temperature and density. However, the conversion efficiency of x-rays from electrons is usually less than one tenth of one percent [12] in long-scale-length plasmas and has been found to be even smaller when ultra-short pulses are used.[13, 14] Ions, on the other hand, carry a large fraction of the absorbed energy [15] and their spectra have been proven to reflect the electron characteristics at the interaction region.[16] In fact it has been found, in the present investigation, that the ion emission exhibits a strong dependence on laser polarization and pulse contrast. Therefore, this investigation has used the ion measurements as a primary diagnostic and the other diagnostics as supporting ones. In particular, it has been found that, in a low contrast pulse interaction, more absorbed laser energy is converted to x-ray energy and thus serves as means for obtaining electron characteristics.

III-4-a Absorption (integrating sphere)

The overall energy absorption into the targets is measured by collecting the reflecting laser energy from the targets into 4π sr solid angle by an integrating sphere (or Ulbricht sphere).[17] The sphere's inside wall is coated with MgO_2 diffusive paint so that even the specularly reflecting light from targets eventually fills up the sphere volume uniformly (see Fig. 3-6). An array of four silicon PIN photodiodes filtered by RG1000s detects the averaged (integrated) reflected energy of 1-μm light. Each

detector is positioned about 45° from the laser optical axis equally spaced around laser entrance aperture and is screened by a baffle to prevent viewing direct light from the target. An RG1000 filter cuts off anything below 0.9 μm so that any harmonics, if any, are not detected and considered as an absorbed energy. Additional ND (Neutral Density) filtering (1% to 100% transmission) is provided to cover a laser intensity scan of two orders of magnitude. The sphere has four 1.5-cm diameter holes for target alignment and a 4-cm laser entrance aperture that together occupy 4.3% of the total area. Although the position of the target viewing holes is asymmetric, it was confirmed that the diffusiveness of the sphere is good enough that different target orientations, say 50° and -50° of incident angles, do not influence the measurements.

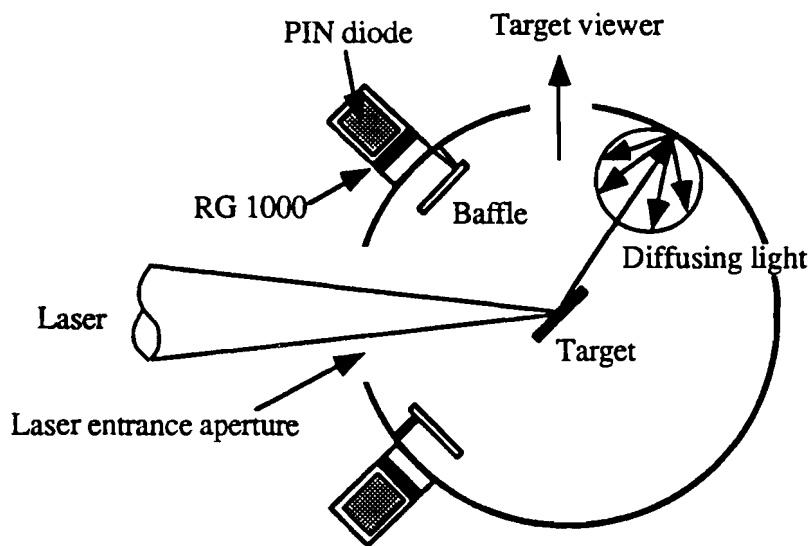Fig. 3-6   Horizontal view of the integrating sphere used in the absorption measurements. The sphere is equipped with four PIN photodiodes (only two of them are shown) which are shaded by baffles to prevent a direct exposure from target reflection.

Caution has been exercised in calibrating the energy/intensity monitor and the integrating sphere. First, a calibrated energy meter (Molectron J50 474) was placed

inside the chamber (placed right behind the focusing lens so that the laser intensity won't be too large) to include the energy loss at two turning mirrors and the focusing optics in the energy calibration on target. The integrating sphere is then calibrated according to the energy/intensity monitor. The calibration shots were executed in the evacuated chamber with a maximum laser intensity focused at the center of the sphere. It has been found that some energy reflected from the back wall of the sphere escapes through the laser entrance aperture (see Fig. 3-7). Reflection from the back wall of the sphere was measured by the back scattering (B.S.) detector (also in Fig. 3-7). The back wall reflection escaping through the sphere entrance aperture is collected by the focusing optics of the target chamber and re-focused on to the B.S. detector. After subtracting a background signal on the B.S. detector due to reflection from the focusing optics, ~8% of reflection from the back wall was obtained. The reflection from the back wall might not be completely collected by the focusing optics. Therefore, the 8% gives the lower limit of the back wall correction. This back wall correction is incorporated in the absorption calculation,

$$\text{Absorption} = 1 - \frac{\text{Scattered Energy}}{\text{Incident Energy}}$$

$$= 1 - \frac{S_{sph} \times C_{calib}}{E_L}, \qquad \qquad 3\text{-}2$$

where S_{sph} and E_L are the signal from the sphere and incident laser energy. C_{calib} is the calibration constant including the back wall correction. The integrating sphere does not collect the energies that reflect back to the entrance aperture. If there are significant amounts of laser energy reflecting back to the laser system, it has to be counted in the nonabsorbed energy and a back scattering monitor complements the integrating sphere. Back scattered energies from targets are collected by the focusing optics and transferred by the beam splitter and focusing lens to the back scattering monitor. The back scattering monitor consists of the identical PIN photodiode and is filtered by an

RG1000 and appropriate ND filters. The same energy meter used for integrating sphere calibrates the monitor including the reflections from the focusing optics. The signal from the PIN diodes is integrated and digitized by an A/D converter and interfaced by a CAMAC system to a PC.
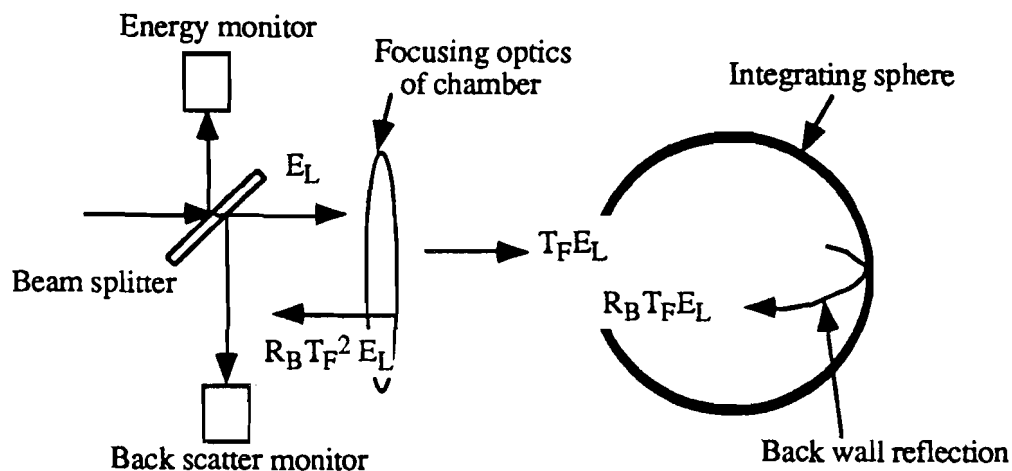

Fig. 3-7   Back wall correction of the integrating sphere. The integrating sphere does not collect all the incident laser energy even without a target in position and this effect has to be taken into account when it is calibrated.

III-4-b Ions (charge collectors)

Charge collector

Since a large fraction of the absorbed laser energy was expected to appear as plasma particle energy, charged particle measurement was chosen as a primary diagnostic. Among particle diagnostics, ion velocity distribution measurements have been widely used in laser-plasma studies [15, 16, 18-23] because of the ion's large mass that makes ions relatively insensitive to the ambient field condition surrounding target plasma. Electron energy and spatial distributions, on the other hand, are subject to the self

generated magnetic field and electric potential. There are several diagnostic schemes for ion measurements: 1) charge collectors, 2) film detectors,[24] and 3) Thomson parabola ion analyzer.[25] The properties of ion blow-off from the plasma needed to be measured include energy (velocity) distribution, ion charge state, and spatial distribution of blow-off. The selection of diagnostics must meet these requirements. The film detectors are suitable for spatial distribution and number measurements, however, data retrieval of energy distribution could be cumbersome and the results might not be accurate. Practical filtering for ions requires the minimum resolvable energy of larger than 1 MeV which is beyond the present experimental parameter range. A Thomson parabola analyzer can resolve ion species and velocity simultaneously, however, generally the size of the analyzer prohibits the detailed measurement of spatial ion distribution and makes total energy measurement difficult. Charge collectors, on the other hand, have a small size and relatively simple structure that allows a spatial ion distribution measurement in an array configuration. Coupled with an electrostatic deflector, the charge collectors can be used to determine the ion charge state Z as a function of velocity,[26] provided the ions consist of a single species that is the case in the present experiments. Charge collectors are also suitable for a multiple-parameter survey where a number of shots are required since their data acquisition is done by electrically contrary to the track based film detectors. An array of five-channel charge collectors is used in the experiments for angular (spatial) distribution measurement. The array consists of one charge collector on the axis of target normal and two on the plane of incidence and two on the plane perpendicular to it. Since the number of the detectors is limited (five detectors), they were relocated according to the target irradiation conditions where different ion angular spreads are expected to cover a wide range of detection angle. The detectors were located at 26 cm from the targets and have an angular resolution of 2.2° or a solid angle of 1.1×10^{-3} sr.
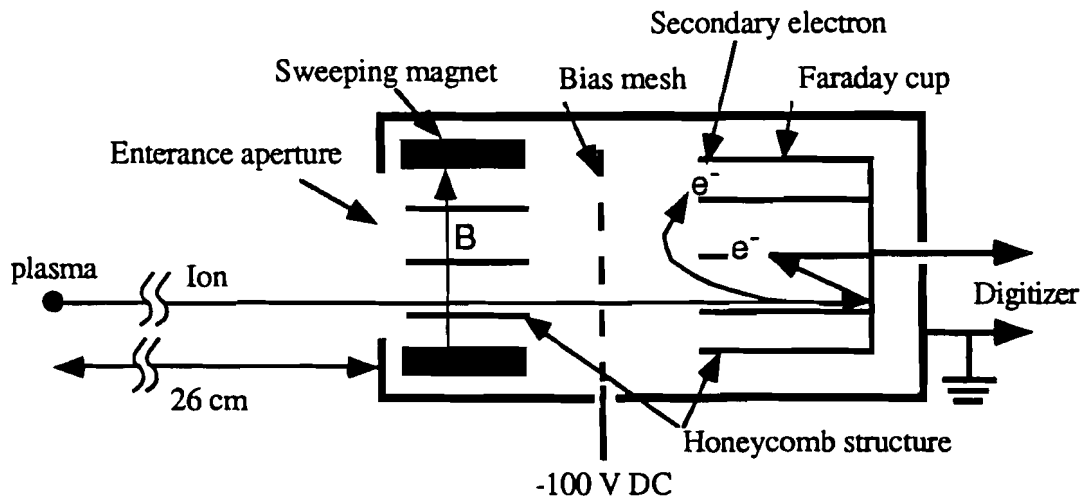
Fig. 3-8 Schematic of charge collector showing magnetic filter, bias mesh and honeycomb structure for reducing electron noises. The distance from the target to detectors is 26 cm through the experiment.

The structure of a charge collector is shown in Fig. 3-8. The important feature of charge collectors is the capability of reducing the noise from plasma electrons and secondary electrons emitting from the detector surface. A 1 kG magnetic field across the entrance aperture deflects the plasma electrons and lets only ions go through. The detector (Faraday cup) has a honeycomb structure so that the secondary electrons from the detector surface are recaptured. An additional reduction of secondary electron noise is provided by a negatively biased mesh in front of the detector. Ion currents are acquired by a 100 MHz temporal digitizer and stored in a PC where further data analyses are done. The noise from run away electrons and x-rays is used as a time fiducial.
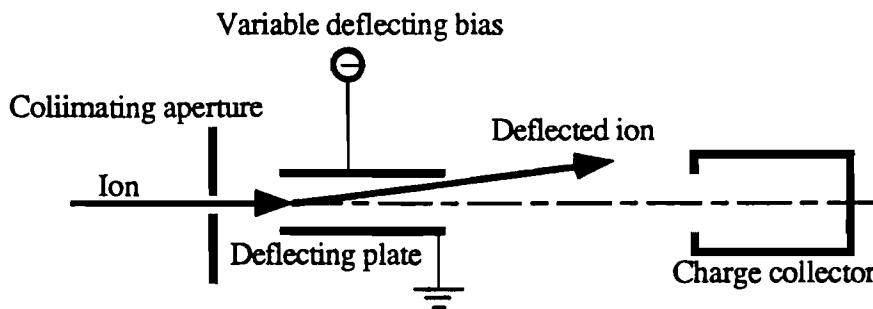
Ion charge state measurement

Fig. 3-9   Electrostatic ion charge analyzer. As the deflecting bias is increased, ion flux moves away from the charge collector aperture. The signal reduction due to deflection is a function of the ion velocity and charge.

To estimate the ion number from the ion current, the charge state of ion as a function of velocity must be known. For the present experiment, it suffices to obtain the average ion charge $Z(t)$ as a function of velocity instead of a detailed distribution of each charge state within the ion blowoff. A schematic of an electrostatic ion charge analyzer is shown in Fig. 3-9. $Z(t)$ is determined by measuring the reduction of ion signal while increasing the bias voltage across the deflecting plate. The signal reduction depends on the velocity and $Z(t)$. One example is shown in Figure 3-10 as a function of the bias voltage calculated for the ion velocity of 1×10^8 cm/sec. The calculations take the size of collimating aperture and charge collector entrance into account. The average ion charge for different velocities is determined by fitting the measured signal reduction to the closest curve. The measurements are done with ions emitted in target normal and used as a representative value of $Z(t)$. With the mapping of $Z(t)$, various quantities can be derived such as number of ions, ion kinetic energy, and the ion velocity distribution.
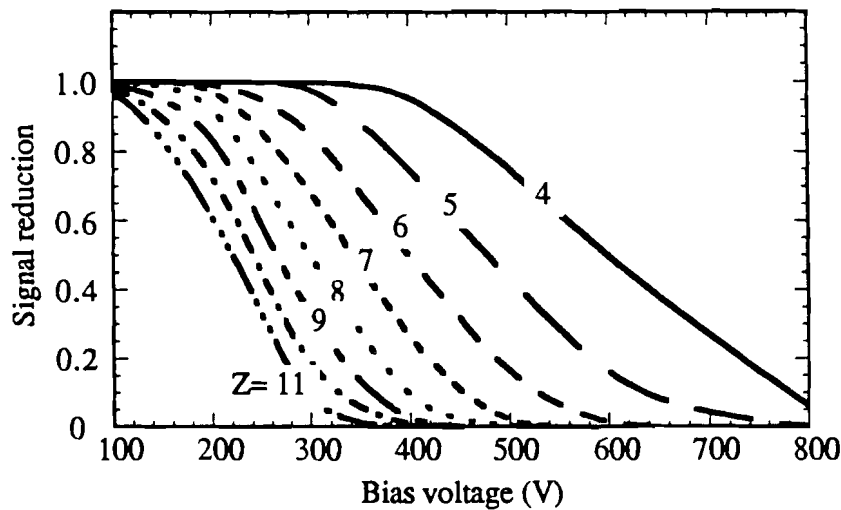
Fig 3-10 Calculated signal reduction on ion current trace as a function of bias voltage for ion velocity 1×10^8 cm/sec. The running parameter is the ion charge Z.

The ion current I(t) detected by a charge collector is expressed as

$$I(t) = Z(t)e\frac{dN_i}{dt},$$

where N_i is the number of ions entering the charge collector and a negligible secondary electron emission is assumed. The ion velocity distribution is then given by

$$\frac{dN_i}{dV_i} = \frac{dN_i}{dt}\frac{dt}{dV_i} = \frac{t^2 I(t)}{eL_D Z(t)}, \qquad\qquad 3\text{-}3$$

where V_i is assumed to be much less than the speed of light, that is, $V_i = L_D/t$, the distance between the target and the detector. Plotting the ion velocity distribution converted from measured ion currents in a semilog scale exhibit a straight line, slope from which an electron temperature is estimated according to Eq.2-34.

Calculation of ion number and energy

From the ion current I(t) measured by the detector normal to the target surface, the total number of ions produced during the interaction can be calculated by

$$N_{ion} = \int \frac{\frac{I(t)}{A_D}}{e\ Z(t)} \frac{\pi}{3} \left(L_D \times \tan\theta_p \right)^2 dt, \qquad 3\text{-}4$$

where $Z(t)$ and θ_p are measured ion charge and half angle of ion plume, respectively. A_D and L_D are the detector area and the distance from targets of the charge collectors, respectively. The factor of $\frac{\pi}{3} \left(L_D \times \tan\theta_p \right)^2$ approximates the ion plume to a cone shape. Uncertainty in the ion number comes from the fluctuation in I(t), errors in measuring $Z(t)$ and θ_p and the approximations in the shape of ion plume.

By assuming the neutrality of plasma blow-off, the total number of electrons also can be calculated by;

$$N_{electron} = \frac{\pi}{3\ A_D} L_D^2\ \tan^2\theta_p \int \frac{I(t)}{e} dt \ .$$

III-4-c Hot electrons (magnetic analyzer)

High energy electrons were measured by a 180° deflecting magnetic electron analyzer with three-channel PIN diode (Quantrad 100-PIN-250) array. (Fig. 3-11) The sensitive layer of the PIN diodes are 250 μm, which is thick enough to detect electron energies up to 700 keV. A permanent magnet provides a 600 G field which is uniform within a few percent over the entire deflection region. The magnet is contained in a high mu (μ) metal case so that stray field effects can be neglected. To reduce noise, a hole opposite to the entrance hole provides an escaping path for x-rays and ions keeping them from undergoing multiple scattering inside the analyzer. The back of PIN diodes is shielded by a 1-mm thick Al plate from direct exposure to target plasma emission.

The Larmor radius R_L of electrons with relativistic effects is given by

$$R_L = \frac{m_e \, v \, c}{e \, B} = \frac{m_0 \, c^2 \, \sqrt{\left(K_{er}/m_0 c^2 + 1\right) - 1}}{e \, B} \; .$$

Here m_e and m_0 are relativistic and rest mass of electron, and K_{er} is the relativistic electron kinetic energy. Energy bins of the electron analyzer as a function of detector position is shown in Fig. 3-12. The three PIN detectors are located at 45, 250, and 550 keV energy ranges. Each detector is filtered by a 12-μm Al foil as a light shield. The range of 45 keV electron in Al is 17 μm and approximately 70% of electrons can go through the foil while the foils for 250 and 550 keV channel provide 100% transmission to electrons.
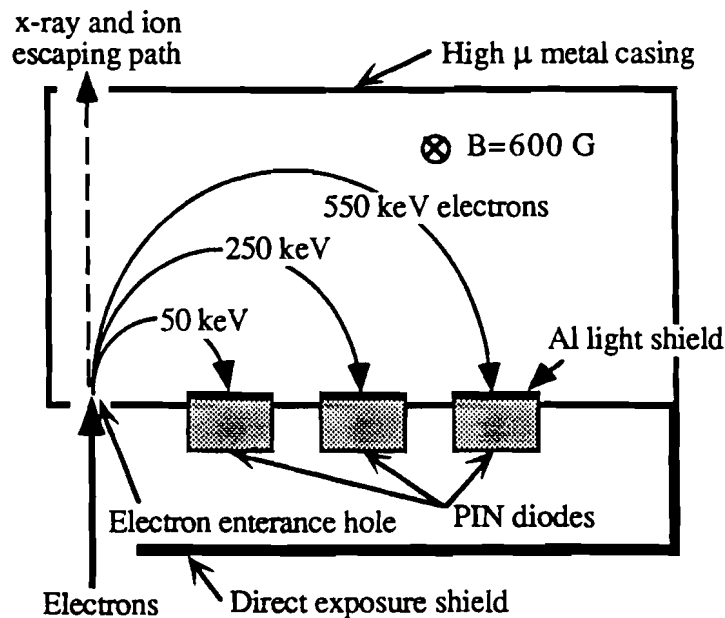

Fig. 3-11 The magnetic electron analyzer detects discrete electron energy distribution. A hole opposite to the entrance hole avoids x-rays and ions from producing noises due to scattering inside the analyzer. The detectors are shielded from direct exposure to emissions from plasma
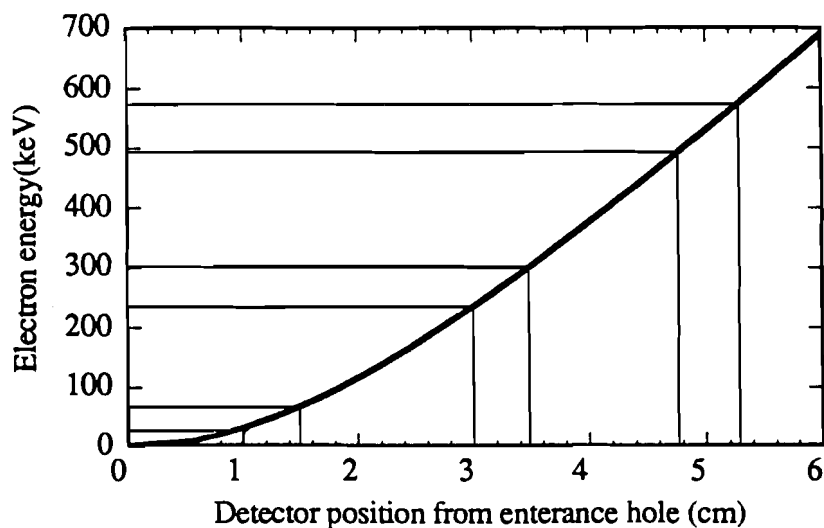
Fig. 3-12 The location of three detectors of the magnetic electron analyzer and
the corresponding electron energies. The separation of the two lines
for each detector corresponds to the size of the detector aperture and
thus energy resolution.

III-4-d X-rays (K-edge filtered PIN and PMT+scintillator)

Two kinds of x-ray radiation, continuum radiation and K_α emission, give the
characteristics of high energy free electrons in the plasma and both are used in the
experiments. Continuum radiation is emitted when a free electron is deflected from its
orbit in an ion field (bremsstrahlung) or absorbed by ions (recombination). The emitted
photon energy depends on the electron energy at a given ion species and impact
parameter,[27] therefore, the electron spectra can be deduced by observing the resulting
continuum spectra. K_α emission is produced when a high energy electrons collide with
a neutral atom and ionizes one of the K-shell electrons whose vacancy in turn is filled
by another electron from L-shell. Since K-shell ionization cross section and the K_α
fluorescence yield is the largest among similar processes, the K_α emission from a solid

target have been used as a diagnostic of hot electron characterization in laser-plasma interactions.[28-32]

In these experiments, the continuum measurement is used to estimate the temperature and total energy of electrons whereas the K_α emission was measured to estimate an electron kinetic energy. Both measurements use K-edge filtering to resolve x-ray spectrum. The method utilizes the fact that the transmission of a filter shows a gentle cutoff on low energy side and a very sharp cutoff on high energy side at the K-edge which together form a band-pass structure. The examples of the transmission of several filters used for the continuum measurements are shown in Fig. 3-13 By choosing an appropriate combination of filters according to plasma conditions, continuum emission can be distinguished from line emissions (desirable or undesirable).
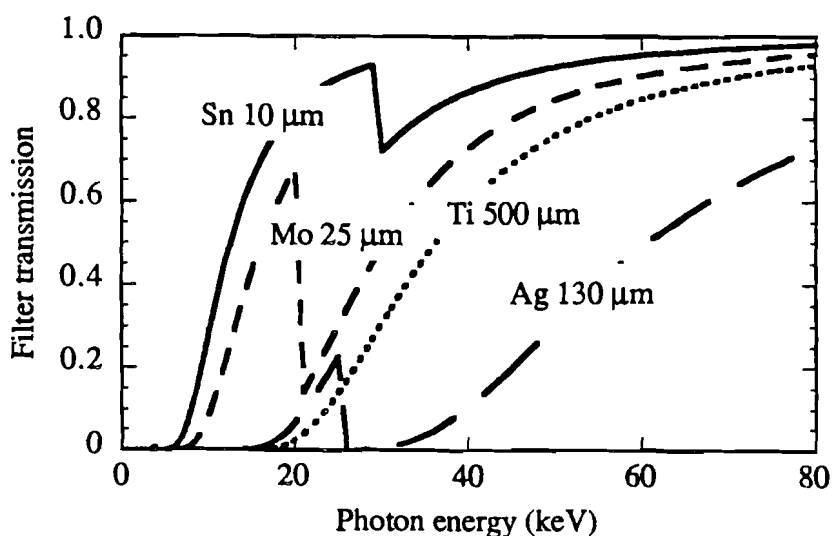

Fig 3-13 X-ray transmission of the filters used for continuum measurements. The transmission includes Be 25 μm (vacuum shield) and Al μm (light shield). Response of the Scintillator is assumed to be flat over the range.

The continuum measurement

A scintillator-photomultiplier tube (PMT) array consisting of four identical channels was used to measure the continuum emission (see Fig. 3-14, only one channel of the array is shown). The detectors are mounted concentrically on a single vacuum-chamber flange 35° to 45° from the target normal. The detectors are located at 46 cm away from the target and subtend a solid angle of 2.3×10^{-3} sr. This detector combination has been chosen because of its good quantum efficiency for high energy photons. The array uses Harshaw 8S8/2 detectors which consist of 2 inch by 2 inch cylindrical NaI scintillators mounted on RCA 6342A PMTs. In addition to the K-edge filters, each detector has a 25 μm Be vacuum window and a 25 μm Al light shield which have 100% transmission above 10 keV photons. Pb collimators provide high energy scattering photon shield. The detectors were calibrated *in situ*, by x-ray silicone PIN diodes. The calibration assumes an isotropic radiation distribution since the PMT array and PIN diodes view the target at different angles. The calibration was done by comparing the total signal from both detectors. The PIN diodes have a known spectral response based on the x-ray absorption of silicone.
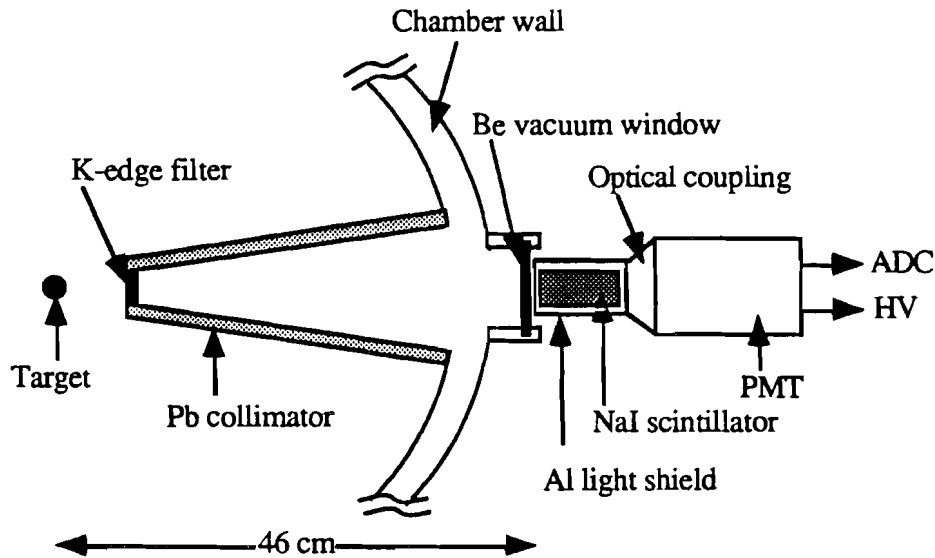
Fig. 3-14   One channel of k-edge filtered scintillator photomultiplier (PMT) x-ray detector is shown.

At the range of $E_{h\nu} > Z^2 E_H$ ($E_{h\nu}$ and E_H are photon energy and the ionization energy of hydrogen ~13.7 eV), the radiation spectrum (the summation of the recombination and bremsstrahlung) falls off as $\exp\left(-\dfrac{E_{h\nu}}{k_B T_e}\right)$.[27] Thus the ratio of continuum signals from two different channel with known spectral response (f_1 and f_2) is a function of the electron temperature, T_e;

$$\frac{S_1}{S_2} = \frac{\int f_1 \exp\left(-\dfrac{E_{h\nu}}{k_B T_e}\right) dE_{h\nu}}{\int f_2 \exp\left(-\dfrac{E_{h\nu}}{k_B T_e}\right) dE_{h\nu}} = R(T_e).$$ 3-5

The electron temperature can be determined in this manner. A set of filter combination (Sn 10 μm, Mo 25 μm, Ti 500 μm, and Ag 130 μm) is chosen so that a plasma temperature of approximately 10 keV, at which the emission power is maximum at $E_{h\nu}$ = 20 keV, is determined. Figure 3-15 show the spectral transmission of the k-edge filters. The spectral response includes the transmission of Be 25-μm vacuum window and Al 25-μm light shield. The spectral sensitivity of the scintillator (measured in

keV/Coulomb) is constant over the desirable spectral range. Since the response of each channel depends on the temperature (slope of the spectrum), the expected spectrum through each filter is also shown in Fig. 3-15 for T_e = 10 keV as an example.
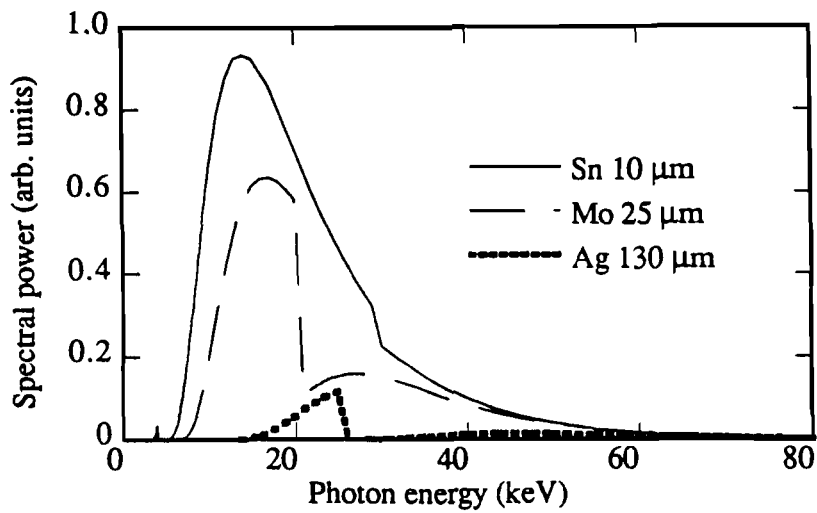
Fig 3-15   Expected x-ray spectrum calculated for each filter combination at T_e
= 10 keV.

The total energy of bremsstrahlung can be obtained, once the electron temperature is known. Let E_{det} be the energy of bremsstrahlung detected by a detector 1, then the total energy $E_{R\infty}$ is given by

$$E_{R\infty} = \frac{\int P_{(R+B)} \, dE_{hv}}{\int f_1 \, P_{(R+B)} \, dE_{hv}} E_{det}, \qquad 3\text{-}6$$

where $P_{(R+B)}(E_{hv})$ is the total spectral power (recombination and bremsstrahlung). The continuum emission originates from either recombination or bremsstrahlung and the present diagnostic doesn't distinguish between them. However, for electrons with a

Maxwellian velocity distribution, the ratio of recombination radiation to bremsstrahlung is given by [27]

$$\frac{P_R}{P_B} = 0.026\frac{Z^2}{T_e}$$

where Z is ion charge state and electron temperature T_e is given in keV. Since $P_R/P_B <$ 1 when $T_e > 1$ keV, only the contribution from the bremsstrahlung will be considered here. Bremsstrahlung then represents the total radiation power and is given by,

$$3.1\times10^{-12}n_in_eZ^2T_e^{1/2} \quad (eV/cm^3),$$

where T_e is expressed in keV. This expression can be used to estimate the total energy of hot electrons, E_{hot}, by comparing with measured radiation energy, that is,

$$E_{hot} = E_{R\infty}\frac{\frac{3}{2}n_eT_{hot}^{1/2}}{3.1\times10^{-12}n_in_eZ^2T_e^{1/2}\tau_{laser}}, \qquad 3\text{-}7$$

where radiation is assumed to last the duration of the laser pulse.

The K_α measurement

Al filtered PIN x-ray diodes (Quantrad 100-PIN-125 with 0.25 μm Si entrance window) are used for K_α emission measurements. Although, this scheme is capable of determining the electron spectrum when used with multilayered targets and high resolution spectroscopy, the determination depends on an assumed spectral shape. The present experiment uses this diagnostic only as a signature of the high energy electron generation, namely single layered targets and a low resolution K-edge filtered spectroscopy are used. By choosing a proper combination of K_α emitter and filter material, this method provides adequate information on high energy electron production. Since the Al target has a thickness of 6000Å, most of which (>60%)

remains solid during the interaction, Al K_α 1.48 keV can be used as the high energy electron signature.

The most important requirement for the diagnostic is the capability of distinguishing the K_α emission from resonance lines. The PIN diode is filtered by a 12-μm foil with the K-edge at 1.56 keV providing a cutoff ratio of 10^8 between Al K_α and He$_\alpha$ (1.59 keV) which is to be the strongest line emission from a few hundreds eV plasma. Figure.3-16 is a channel spectral response including the Al filter and detector sensitivity. The high energy sensitivity cut-off above $E_{h\nu}$ =20 keV is due to the finite thickness of the PIN diode's sensitive layer (125 μm). The detector is sensitive to the continuum emission between 4 keV and 20 keV, however, that energy is usually negligible compared to the line emission.
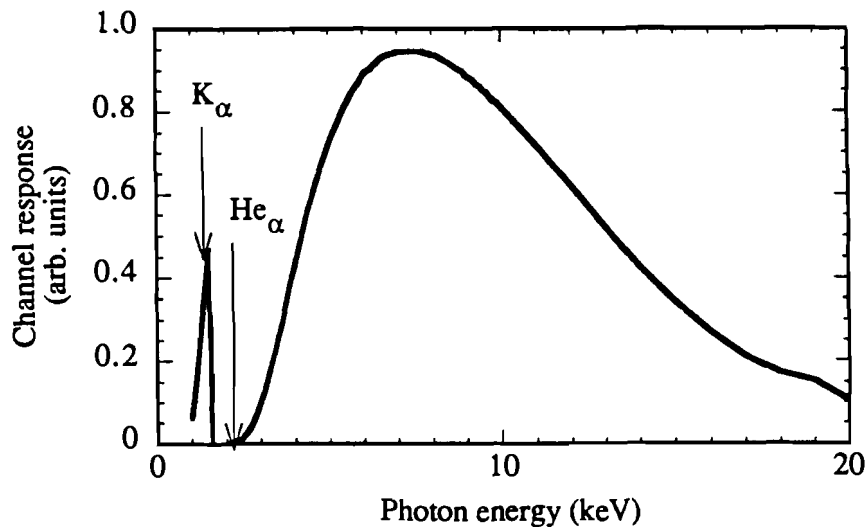

Fig 3-16 Spectral response of the K_α detector. The K-edge of 12-μm Al filter provide a 10^8 discrimination between the K_α and H_α lines.

REFERENCES

[1] D. Strickland and G. Mourou, "Compression of amplified chirped optical pulses," Optics Comm. **56**, 219 (1985).

[2] Y.-H. Chuang, D. D. Meyerhofer, S. Augst, H. Chen, J. Peatross and S. Uchida, "Suppression of the pedestal in a chirped-pulse-amplification laser," J. Opt. Soc. Am. B **8**, 1226 (1991).

[3] Y.-H. Chuang, "Amplification of broad-bandwidth phase-modulated laser pulses and application," Ph. D. Thesis, (University of Rochester, 1992).

[4] M. D. Perry, F. G. Patterson and J. Weston, "Spectral shaping in chirped-pulse amplification," Opt. Lett. **15**, 381 (1990).

[5] G. Albrecht, A. Antonetti and G. Mourou, "Temporal shape analysis of Nd^{+3}:YAG active passive mode-locked pulses," Optics Comm. **40**, 59 (1981).

[6] P. B. Corkum, F. Brunel, N. K. Sherman and T. Srinivasan-Rao, "Thermal response of metals to ultrashort-pulse laser excitation," Phys. Rev. Lett. **61**, 2886 (1988).

[7] A. E. Siegman, "chapter 10," in *Lasers*, edited University Science Books, Mill Valley, CA, 1986) p.382-386.

[8] S. J. Augst, "Tunneling Ionization of Noble Gas Atoms Using a High Intensity Laser at 1 μm Wavelength," Ph. D. Thesis, (University of Rochester, 1991).

[9] M. D. Perry, O. L. Landen, A. Szöke and E. M. Campbell, "Multiphoton ionization of the noble gases by an intense 10^{14}-W/cm^2 dye laser," Phys. Rev. A **37**, 747 (1988).

[10] N. A. Ebrahim and C. Joshi, "Electron heating in high intensity CO_2 laser-plasma interaction," Phys. Fluids **24**, 138 (1981).

[11] R. Decoste, J. Kieffer and H. Pépin, "Spatial characteristics of continuum x-ray emission from lateral energy transport in CO_2-laser-produced plasmas," Phys. Rev. Lett. **47**, 35 (1981).

[12] W. Priedhorsky, D. Lier, R. Day and D. Gerke, "Hard-x-ray measurements of 10.6-μm laser-irradiated targets," Phys. Rev. Lett. **47**, 1661 (1981).

[13] H. Chen, Y.-H. Chuang, J. A. Delettrez, S. Uchida and D. D. Meyerhofer, "Study of x-ray emission from picosecond laser-plasma interaction," in the Proceedings of *Short-pulse high-intensity lasers and applications*, (Los Angeles, CA, 1991).

[14] U. Teubner, G. Kühnle and F. P. Schäfer, "Soft x-ray spectra produced by subpicosecond laser-double-pulses," Appl. Phys. Lett. **59**, 2672 (1991).

[15] T. P. Donaldson, J. E. Balmer and P. Wägli, "Energy loss to resonantly accelerated ions in laser-plasma," Optics Comm. **31**, 61 (1979).

[16] P. Church, F. Martin, H. Pépin and R. Decoste, "Irradiance scaling of fast ion expansion for CO_2 laser produced plasmas," J. Appl. Phys. **53**, 874 (1982).

[17] R. P. Godwin, R. Sachsenmaier and R. Sigel, "Angle-dependent reflectance of laser-produced plasmas," Phys. Rev. Lett. **39**, 1198 (1977).

[18] P. D. Gupta, Y. Y. Tsui, R. Popil, R. Fedosejevs and A. A. Offenberger, "Ion expansion characteristics from a KrF-laser-produced plasma," Phys. Rev. A **33**, 3531 (1986).

[19] P. Wägli and T. P. Donaldson, "Fast-ion emission and resonance absorption in laser-generated plasma," Phys. Rev. Lett. **40**, 875 (1978).

[20] B. Luther-Davies, "X-ray bremsstrahlung and fast-ion measurements from picosecond laser-produced plasmas," Optics Comm. **23**, 98 (1977).

[21] P. Wägli, T. P. Donaldson and P. Lädrach, "Scaling of nonthermal ion energy in laser-generated plasma," Appl. Phys. Lett. **32**, 638 (1978).

[22] P. M. Campbell, R. R. Johnson, F. J. Mayer, L. V. Powers and D. C. Slater, "Fast-ion generation by ion-acoustic turbulence in spherical laser plasmas," Phys. Rev. Lett. **39**, 274 (1977).

[23] A. W. Ehler, "High-energy ions from a CO_2 laser-produced plasma," J. Appl. Phys. **46**, 2464 (1975).

[24] R. L. Fleischer, P. B. Price and R. M. Walker, *Nuclear Tracks in Solids*, (Univ. of California Press, Berkeley, 1975).

[25] C. Joshi, M. C. Richardson and G. D. Enright, "Quantitative measurements of fast ions from CO_2 laser produced plasmas," Appl. Phys. Lett **34**, 625 (1979).

[26] R. Decoste and B. H. Ripin, "High-energy ions from a Nd-laser-produced plasma," Appl. Phys. Lett. **31**, 68 (1977).

[27] J. Cooper, "Plasma spectroscopy," Rep. Prog. Phys. **24**, 35 (1966).

[28] K. Terai, H. Daido, M. Fujita, H. Nishimura, K. Mima, S. Nakai and C. Yamanaka, "Hot electron energy distribution in one-dimensional cannonball target at 10.6μm laser wavelength," Jpn. J. Appl. Phys. **23**, 445 (1984).

[29] B. Luther-Davies, A. Perry and K. A. Nugent, "K_α emission measurements and superthermal electron transport in layered laser-irradiated disk targets," Phys. Rev. A **35**, 4306 (1987).

[30] R. J. Harrach and R. E. Kidder, "Simple model of energy deposition by superthermal electrons in laser-irradiated targets," Phys. Rev. A **23**, 887 (1981).

[31] J. D. Hares, J. D. Kilkenny, M. H. Key and J. D. Lunney, "Measurement of fast-electron energy spectra and preheating in laser-irradiated targets," Phys. Rev. Lett. **42**, 1216 (1979).

[32] N. A. Ebrahim, C. Joshi and H. A. Baldis, "Energy deposition by hot electrons in CO_2-laser-irradiated targets," Phys. Rev. A **25**, 2440 (1982).

CHAPTER IV

Results

IV-1 Absorption measurements

The fractional absorption of laser energy to targets are shown in Fig. 4-1 as a function of the angle of incidence, θ_{inc}. Figures (a) and (b) correspond to the high (main/prepulse > 10^5) and low ($\approx 10^3$) contrast pulse interactions. The open and closed circles indicate s- and p-polarizations and each data point is an average of 10 laser shots. There is approximately 10% shot-to-shot fluctuation.

The absorption was measured with a nominal laser intensity of 3×10^{15} W/cm^2 calculated for normal incidence. The laser energy was kept constant for all the incident angles, thus, the effective intensity on target depends on θ_{inc}. For example, the effective intensity at $\theta_{inc} = 20°$ is 5.4 times larger than that of $\theta_{inc} = 80°$. The backscattered energy was only 2 to 4% in both the low and high contrast pulse interactions for all the angle of incidnece. In spite of the polarization and incident angle dependence of the integrating sphere measurement for the high intensity contrast case, the back scattering energy shows only a slight difference on incident angle, if any, and no polarization dependence. The values in Figs. 4-1 include the back scattering measurements.

The absorption characteristics in terms of the laser polarization and incident angle are dramatically altered between the two pulse contrasts. There is no polarization dependence for the absorption in the low contrast case while the absorption in the high contrast case exhibits a strong polarization dependence. The absorption of the low contrast pulse declines monotonically with increasing incident angle (see Fig. 4-1-a), a tendency similar to the absorption of s-polarized light interacting with long-scale length plasmas [1] where collisional absorption in underdense plasma is dominant. This observation is consistent with the existence of the prepulse (see Fig. 3-3-a) whose

intensity and energy both exceed the breakdown threshold of solids.[2] The polarization insensitivity indicates that there is a polarization mixing at the critical density or that the absorption due to resonance field does not play a very important role. In spite of these differences, both low contrast and high contrast (p-polarization) exhibit ~50% absorption. The balance of absorbed energy deposition to ions and x-rays will be discussed for high and low contrast pulse interactions in chapter V.

An interesting and important polarization dependence appears in the high contrast case where p-polarization absorption is always larger than that of s-polarization (see Fig. 4-1-b). This difference is approximately 30% when the incident angle is 55°. The difference is smaller towards the normal incidence indicating the contribution of p-polarized component of laser electric field to the difference because the distinction between the polarizations diminishes towards the normal incidence. It is shown, in the description of ion energy measurement, that most of the energy difference between the two polarizations appears as fast ion energy. It can be stated from the comparison of ions and absorption measurements that the absorption of p-polarized light in high contrast case consists of two mechanisms, one of which does not depends on the polarization and the other appears only for p-polarized light. Since the additional absorption due to p-polarized component seems to generate the fast ions, the characteristics of the absorption mechanism will be examined by the fast ions characteristic dependence on p-polarized component of laser.

a Low contrast pulse

b High contrast pulse

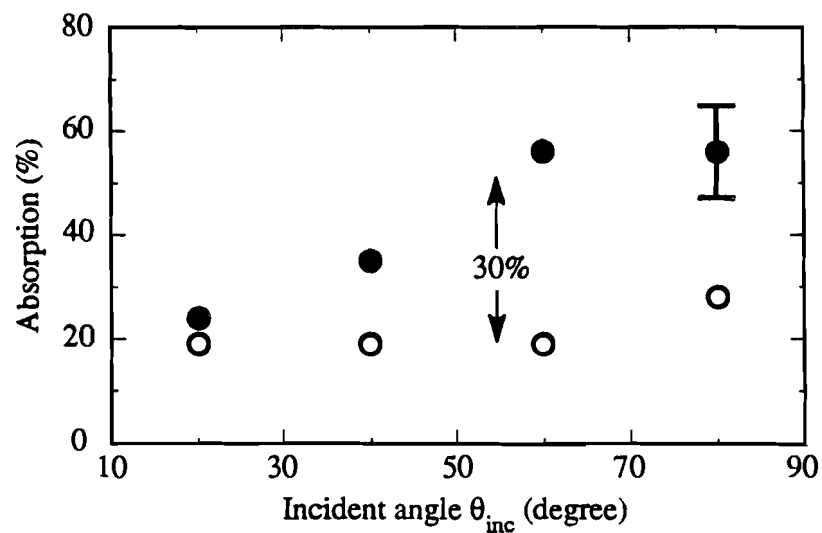Fig. 4-1   Incident angle dependence of laser energy absorption measured by the integrating sphere. The open and closed circles indicate s- and p-polarizations. The low contrast pulse absorption (a) exhibits no polarization dependence while the high contrast pulse absorption (b) shows a clear polarization dependence. The absorption difference between s- and p-polarization at 55° incident angle is 30%.

IV-2 X-ray emission

To provide a reference for the characteristics of the nonthermal electrons produced from the high contrast interactions, the characteristics of electrons produced from low contrast interaction or under the existence of preformed plasma were examined. With a preformed plasma more electron energy is converted to x-ray emission. This reflects the electrons characteristics such as temperature and total energy. Targets were irradiated with the same conditions as high intensity contrast interactions, that is, with an intensity of 1.6×10^{15} W/cm^2 at an incident angle of 55°. First, plasma electron temperature is deduced by comparing observed x-ray signals with calculated values assuming a Maxwellian electron distribution. The temperature and energy of the radiation are used to estimate the total energy deposited into the nonthermal electrons.

A K-edge filtered scintillator-PMT array is used to detect x-ray continuum emissions and estimate the nonthermal electron temperatures.[3, 4] Significant signals are detected only during the low contrast interactions. The high contrast interactions, on the other hand, did not produce any detectable signal. The reduction of the signal from the low contrast to the high contrast interactions is at least two orders of magnitude. Therefore, the x-ray measurements will be described only for the low contrast case. No significant polarization dependence of the electron temperature and x-ray yield was found in the low contrast interaction. This is consistent with the absorption measurements. The expected signal ratios between the four PMT channels as a function of electron temperature are calculated according to Eq.3-5 and are shown by the lines in Figs.4-2. The calculations assume a two-temperature (hot and cold electrons) Maxwellian distribution, however, the results are not sensitive to the choice of cold electron temperature and are obtained with 500 eV. In Figs.4-2 the horizontal arrows represent the experimental values which connect to vertical arrows indicating corresponding hot electron temperatures. Each experimental value represents seven-shot data average with an uncertainty of 20%. The detectors view targets 35°~45° away from the target

normal, however, no significant signal deviation within the array due to the detector location was found. The signal ratios include the sensitivity of an individual detector. Three figures agree on 3~7 keV hot electron temperature reasonably well.

a Signal ratio of Ag/Mo compared to theory (solid line)
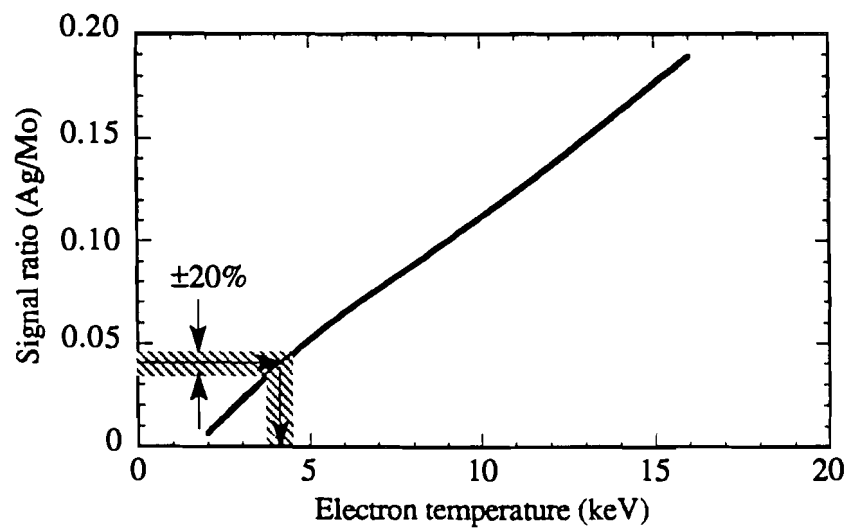
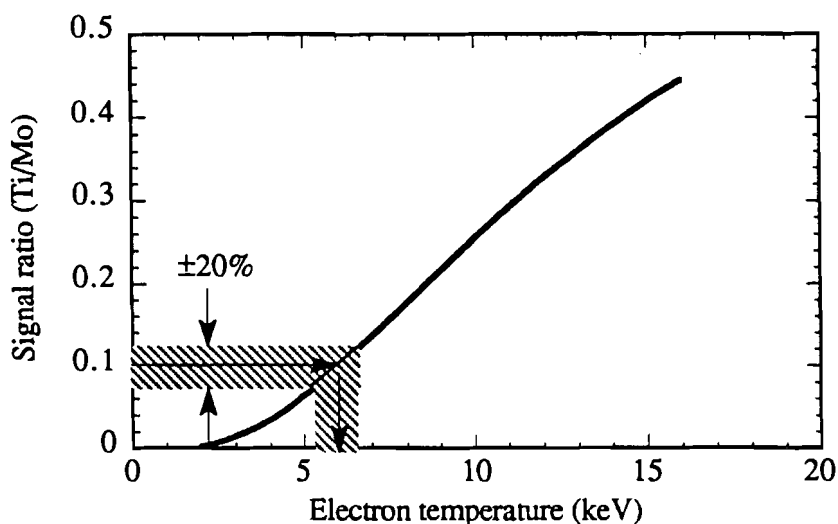b Signal ratio of Ti/Mo compared to theory (solid line)

Fig. 4-2   X-ray signal ratios as a function of hot electron temperature. The
experimental values of signal ratios between the filter combinations
are indicated by arrows. Uncertainty of the ratios are ±20% at most.
Three combinations agree with reasonably to a 5±2 keV of hot
electron temperature.

Assuming an isotropic radiation, total continuum radiation energy, $E_{R\infty}$, can be
estimated using Eq.3-6 and the measured temperature. Although, $E_{R\infty}$, when
expressed in terms of a fraction of the incident laser energy,varies from shot to shot and
from detector to another, they range from 0.004% to 0.022%. These fractional x-ray
yields are similar to the results of a previous experimental study on a hard x-ray
measurements of long pulse (750 ps) CO_2 laser-irradiated targets.[5] Taking $T_{hot} = 5$
keV, $n_i = 10^{20}$ cm^{-3}, and $Z = 11$ as the average values for underdense plasma, Eq.3-7
estimates the ratio of the electron energy to the radiation energy to be 150 which gives
0.5% to 3% of laser energy deposited into hot electron energy. If the x-ray emission is
directed toward the target normal, the estimated values might have given the lower limit

since the energy of the x-ray is obtained ~40° from the target and isotropic emission is assumed.

Assuming the hot electrons are generated by resonance absorption, the mean energy of heated electrons is related to the absorbed laser intensity ϕ_{abs} by, [6]

$$<\mathcal{E}> = (m_e \omega_0 \phi_{abs} L_n/n_c)^{1/2}.$$

This expression can be used to estimate the absorbed energy with $<\mathcal{E}> = 5$ keV and $L_n = 1$ μm (assuming 1×10^6 cm/sec thermal expansion in 100 ps, the duration of the prepulse) giving ~20% of absorption fraction. Precise determination of the energy fraction requires measurements of L_n and distribution of radiation.

IV-3 Ion measurements

This section will discuss the ion current measurements, the most important diagnostic of this study. To fully characterize the ion emission, extensive measurements have been conducted including p-polarized intensity dependence of ion blowoff, angular distribution, and ion charge distribution. These ion data are used to obtain the characteristics of the high energy electrons such as temperature, kinetic energy, and total number. Dramatic changes of the ion blowoff characteristics due to the interacting pulse contrasts are described. Then, the focus of attention is given to the ion emission from the high contrast pulse interaction where an strong dependence of p-polarized component has been found.

IV-3-a Intensity contrast dependence

Figures 4-3 show ion current traces detected along the target normal. The distance from the target to the detector was 26 cm. The targets were irradiated with an intensity of 1.6×10^{15} W/cm^2 at an incident angle of 55°. Each curve is obtained by averaging up to seven laser shots under similar conditions with a ~20% shot-to-shot fluctuation. All of the ion current traces with the exception of the high contrast s-polarized pulse exhibit two-ion-component feature; a fast ion component leading a thermal component as noted

in the figures. Although, the thermal component of the high contrast interactions is much more energetic than that of the low contrast interactions, the component is still called "thermal" because it exists with s-polarization where only gasdynamic processes (thermal effects) are expected to be involved. There are number of distinctive features between the two pulse contrast cases in terms of polarization dependence, amplitude of current, and ion kinetic energy (velocity) which are described below.

There is no polarization dependence to within the uncertainty of the measurement in the case of low contrast pulse interaction (Fig. 4-3-a). Both polarizations show the predominant thermal ion component. The polarization independence is consistent with the absorption measurement and suggests that the absorption process due to a resonantly oscillating field at the critical density is inoperative or that the mixing between the polarization occurs. Both polarizations also show a fast ion component indicative of resonance absorption and/or other processes which produce hot electrons (The small bursts at the time origin are due to high energy electrons and x-rays). However, the amount of fast ion is much smaller than that of the high contrast pulse interaction, an important distinction between the two conditions. The polarization independence of the hot electron generation has been related to the rippling of the critical surface due to a radiation pressure [7] which is likely to be taking place in the presence of the preformed plasma. This is consistent with the x-ray measurements. The ion current traces from the high contrast pulse interaction, on the other hand, exhibit a clear polarization dependence. The trace of p-polarization has both fast and thermal component while s-polarization has thermal component only (Fig. 4-3-b). This is consistent with the absorption measurements. The fast ion peak dominates the thermal component and has been found to carry 40% of the absorbed laser energy. This is in contrast to the low contrast case where less than a few percent of the laser energy goes to the fast component. The appearance of the large fast ion component indicates an important influence of the p-polarization component of the laser electric

field on the absorption process and has been further investigated in terms of the p-polarized intensity strength as is described in next section.

The second feature is that the ion current density from high contrast interaction is about fifty times larger than that of the low contrast interactions (note the units of the ordinate). A single charge collector only detect a part of the entire ion blowoff and the total ion current is supplemented by ion angular distribution measurements described in the following section. Therefore, the ion current density depends on the angular distribution ion blowoff. Since the strength of current depends also on the velocity of carrier, the strong ion current in the high contrast pulse is due to the high velocity of ions which is the third feature described below. In fact the total number of ions detected by the ion trace measurements has been found to be similar between the two contrast cases.

The third feature is the overall velocity shift towards higher velocity in the high contrast interactions. Even the thermal component from the high contrast case falls in the velocity range of the fast ion component of low contrast case. This suggests that a very high temperature is realized in the region of the thermal component production. The kinetic energy of the fast ion component at the peak of the current (at 0.35 μs) is approximately 80 keV. The ion charge state measurements confirmed that this component consists of Al ions.

a Low intensity contrast
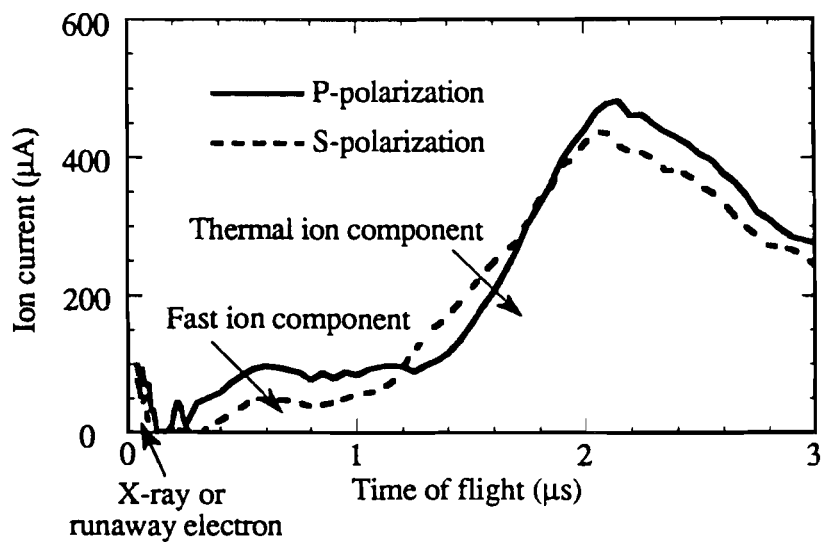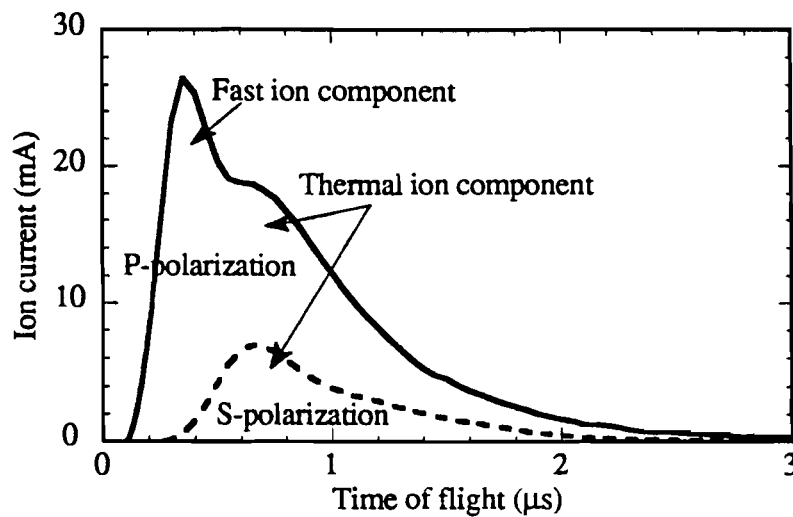

b High intensity contrast

Fig. 4-3   Ion current traces from low and high contrast pulse interactions
detected at the target normal. (a) Low contrast interactions and (b)
high contrast interactions. Solid lines and broken lines correspond
to s- and p-polarized light, respectively.

IV-3-b P-polarized intensity dependence

To examine the effects of laser polarization on the ion emission, total laser energy (intensity I_L) and p-polarized intensity I_p (defined in Eq.3-1 as $I_0\cos^2\phi_{pol}$) were altered independently. To alter I_p, the polarization-control $\lambda/2$ wave plate was set to intermediate positions between pure s- and p-polarizations with total energy being kept constant. Two total laser intensity settings were used; 1×10^{15} and 8×10^{15} W/cm^2. Three ion curves for different I_p were obtained for each total intensity and are shown in Fig 4-4-(a) and (b), respectively. The detector configuration is same as for Fig. 4-3. Each curve again represents a seven-shot average with a 20% uncertainty indicated by an error bar. In Fig. 4-4-a I_p's are 1×10^{15} (p-polarization), 3×10^{14}, and 0 (s-polarization) W/cm^2 indicated by solid, broken and dotted lines, respectively. Likewise, in Fig. 4-4-b $I_p = 8$ (dotted line), 5 (broken line), and 1 (solid line) $\times10^{15}$ W/cm^2. It appears in both figures that the amplitude and the balance between the two components depend on I_p. It is important to note that two traces indicated by the solid lines in Fig. 4-4-a and b were obtained with nearly identical I_p and show similar curves despite the difference in I_0 by a factor of eight (see Fig. 4-5). From these figures, it is clear that the ion current trace depends entirely on the p-polarized intensity and not the total laser energy or intensity.

Another interesting point is that the relative amplitude of the two components strongly depends on I_p. Between $I_p = 1\times10^{15}$ and 5×10^{15}W/cm^2 the dominant peak is reversed and the growth of the fast ion component seems to saturate while the thermal component keep growing at the highest intensities. This suggests the transition of interaction processes at that intensity.

a Ion current at low intensity < 10^{15} W/cm^2
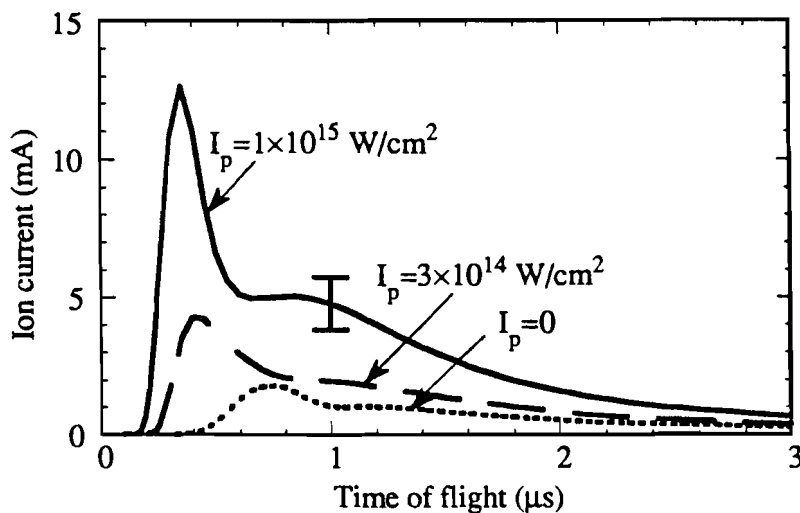
b Ion current at high intensity > 10^{15} W/cm^2

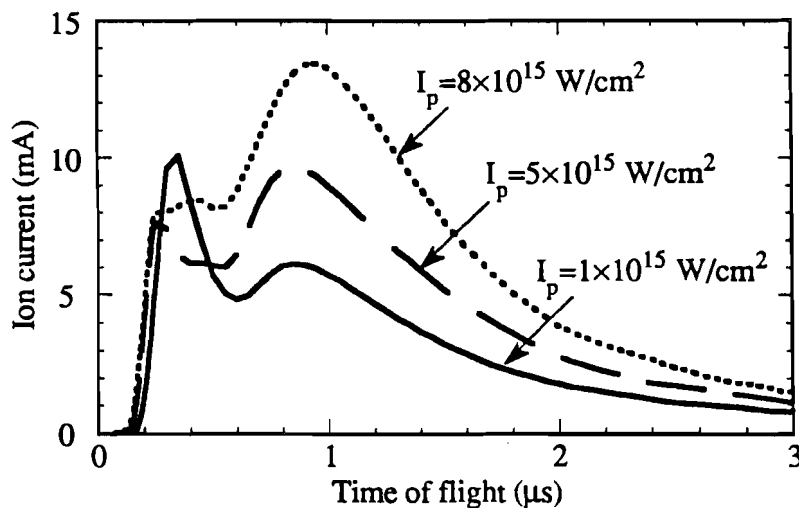Fig. 4-4   P-polarized intensity I_p dependence of ion current. (a) Ion current traces with $I_p \leq 10^{15}$ W/cm^2 (10, 3, 0×10^{14} W/cm^2 from top to bottom) and I_L is kept constant (1×10^{15} W/cm^2). (b) with I_p=8, 5, 1×10^{15} W/cm^2 while I_L is kept 8×10^{15} W/cm^2. The solid lines in both figures are similar despite of a factor of eight difference in I_L.
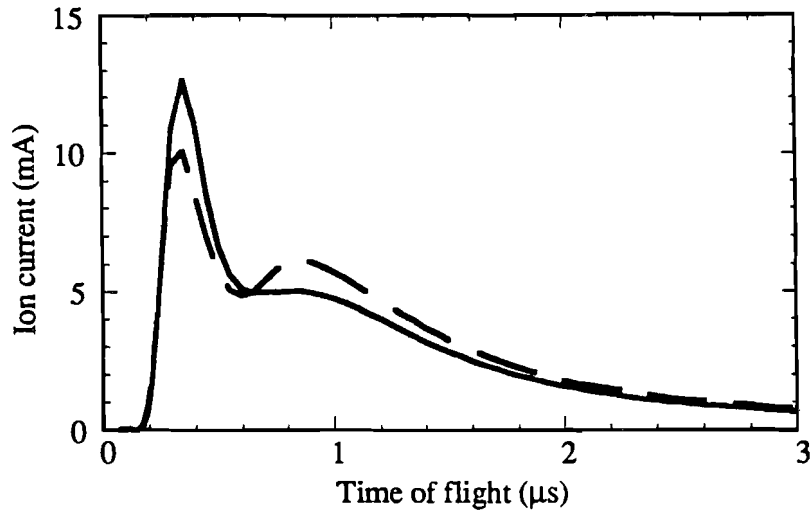
Fig. 4-5   Comparison of two ion current traces obtained from different total laser intensity but a similar p-polarized intensity ($I_p = 10^{15}$ W/cm^2). The solid and the broken lines correspond to $I_L = 8\times10^{15}$ and 1×10^{15} W/cm^2.

IV-3-c Ion velocity distribution and electron temperature

The ion current traces shown in Figs.4-4 are converted to velocity distribution by Eq. 3-3 and shown in Fig. 4-6 (only three representative curves are shown). Polarization and velocity dependent ion charge distribution described in the next section is taken into account in calculating the ion number. The velocity distribution clearly shows a high energy tail which consists of the fast ion component.

Fig. 4-6   Ion velocity distribution calculated from the ion current trace and ion charge measurement. Only three p-polarized intensities are chosen to represent the electron temperature dependence on I_p. The electron temperatures were obtained by fitting the isothermal expansion model (see section II-6) to the slope of fast ion distribution.
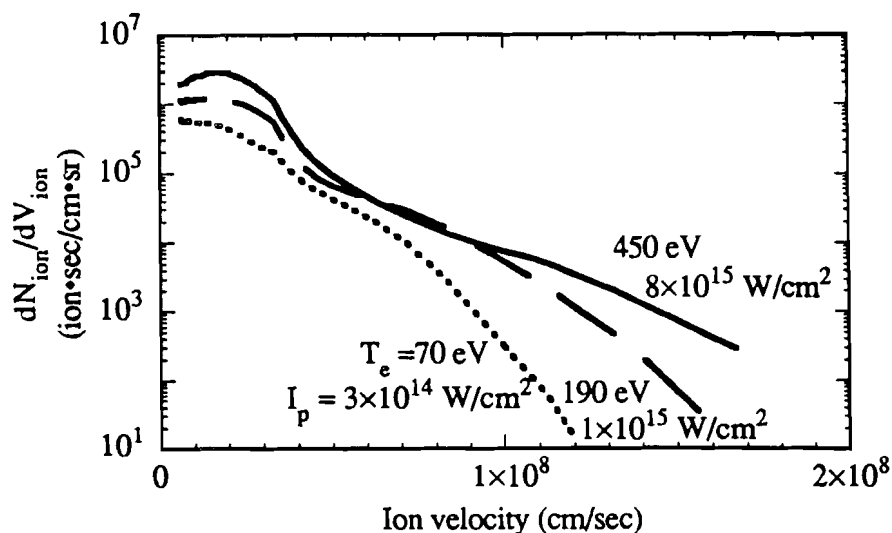
The high energy tail is fit by the isothermal expansion model to deduce the electron temperature which is plotted against I_p in Fig. 4-7. By fitting a straight line to the slope of the high energy tail of the distribution, electron temperature can be deduced through an expression which is derived in Eq. 2-34;

$$T_e = \frac{M_{Al}}{Z_{Al}\, slope^2} ,$$

where M_{Al} is the mass of Al ion. The isothermal expansion model seems to be plausible since the high energy ion tail of the velocity distribution extends a straight line which is expected from the model. The applicability of the isothermal expansion model to the present plasma condition depends on the assumption of plasma neutrality. This is verified by the fact that the additional absorption for p-polarized light due to the ponderomotive force appears as a fast ion energy entirely, therefore, the energy transfer

from electrons to ions is very efficient which suggests that the ion acceleration is done at the very beginning of the expansion and ions move with electrons keeping the charge neutrality. Note that the when ions and electrons expand together, almost entire energy is carried by ions assuming the electron thermal energy is not extremely high, $T_e/T_i<m_i/m_e$.

The open and closed circles in Fig. 4-7 correspond to the low and high total laser intensity, I_L (Fig. 4-4-a and b), respectively. It is apparent that electron temperature depends only on I_p and not I_p. The error bars on the figure come from the uncertainty of fitting a straight line to a slightly curved high energy tail. This temperature will be compared with the directed energy of accelerated electrons to explain the narrow angle of ion angular distribution and acceleration mechanism.
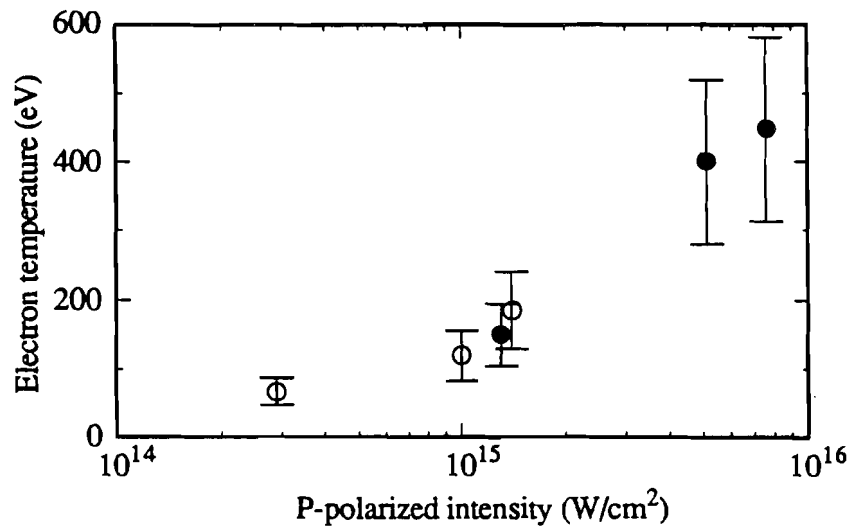

Fig. 4-7   Electron temperature as a function of p-polarized intensity, I_p deduced from the velocity distribution using an isothermal expansion model. The open and closed circles correspond to the low and high I_L (Fig. 4-4-a and b), respectively. The electron temperature depends only on I_p.

IV-3-d Ion charge measurements

The ion charge distribution detected by charge collectors is required to calculate both ion number and electron kinetic energy accelerating the fast ions as well as electron temperature. The velocity distribution of ion charge state is used to translate the ion current to the ion number. The ion charge measurements also give a measure of how much ion-electron recombination takes place during flight. Recombination has to be taken into account in calculating the kinetic energy of the electrons from the total ion energy.

The ion charge state from the high contrast interaction detected along the target normal is plotted against the ion velocity in Fig. 4-8. The target irradiation condition is same as for the ion current trace measurements. Although the electrostatic analyzer only distinguishes Z/A, ion charge per unit atomic mass, the targets consist of pure Al, therefore, A is fixed to be 27. There is a possibility of a contamination layer such as diffusion pump oil building up on the surface of targets and producing H^+ (hydrogen) ions. H^+ can be accelerated preferentially in the plasma potential and would obtain maximum velocity, resulting a fast ion peak if they exist. The analyzer can distinguish H^+ from other ions since only H^+ has Z/A=1 and, within the detector sensitivity, confirmed that there are no H^+ ions in current trace. The two polarizations exhibit different dependence on velocity, however, up to eleventh charge state (He-like) has been found in both polarizations which is consistent with the temperature measurement described later. In calculating the velocity distribution, it is assumed that charge state of the entire ion blowoff is represented by this measurement. The average ion charge $\overline{Z}$ is calculated by

$$\overline{Z} = \frac{\int\limits^{fast} Z(t)N_i(t)\, dt}{N_{total}} = \frac{\int\limits^{fast} \frac{Z(t)I(t)}{eV_i(t)}\, dt}{N_{total}},$$

where Z, I, V_i are charge state, current and velocity of ions, respectively. The integration was done over the fast ion peak and was $\overline{Z}$ = 5.6±1.

The ion charge state detected by the charge collectors may be affected by a three-body-recombination during flight. The estimate of the recombination is required to calculate the electron energy at birth. Since the degree of the recombination is a function of electron temperature and ion velocity, i.e. the p-polarized intensity I_p, the variation of the recombination due to different I_p was supplemented by a model calculation [8]. In their calculation, Goforth and Hammerling solved recombination rate equation and showed that the expected ion charge state at the detector depends on plasma electron temperature (see Fig. 4 of the reference 8). To compare their calculation and our experimental results, the electron temperature deduced from ion measurements as a function of p-polarized intensity, I_p, was used to map out the average ion charge against I_p and shown in Fig. 4-9. The model and the experiment are in good agreement and the calculated recombination is incorporated into the electron kinetic energy calculation described in the following section.
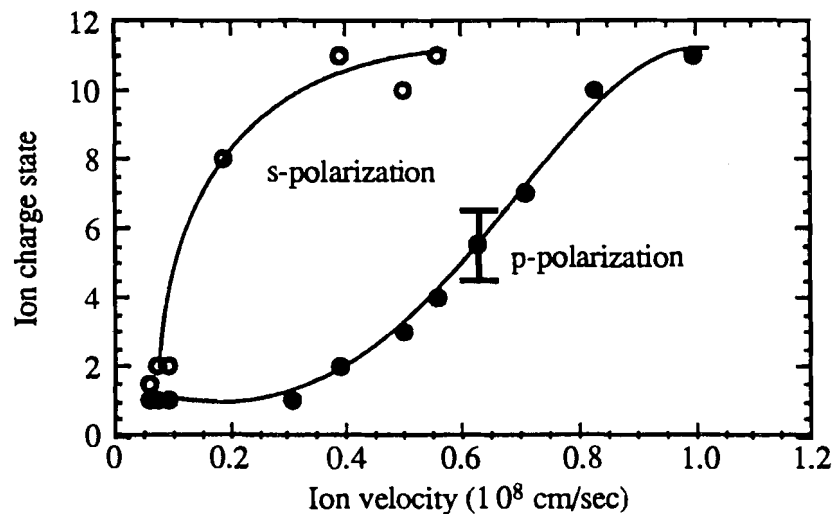

Fig. 4-8 Ion velocity distribution of ion charge state. The error bar corresponds to the uncertainty in fitting the experimental data to the theoretical curves (see Fig. 3-10).
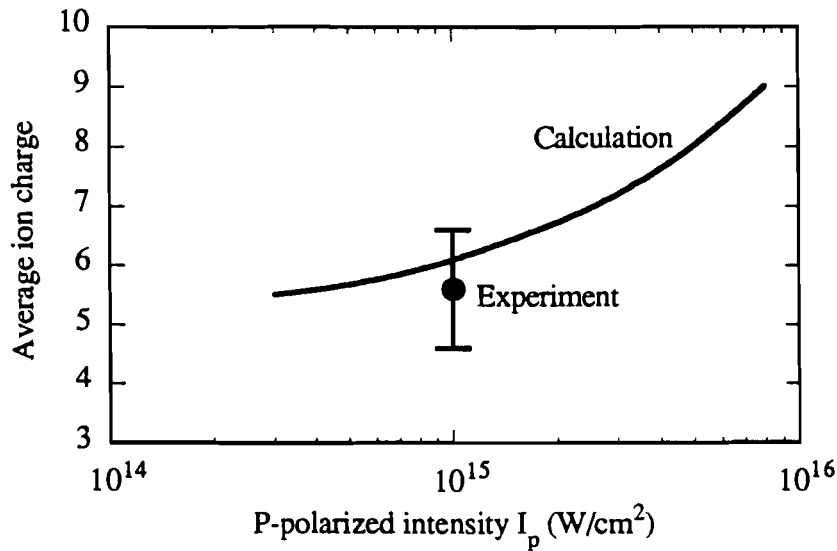
Fig. 4-9   Comparison of the experimental data and model calculation on measured ion charge states. The calculation is based on the three body recombination.

IV-3-e Polar angular distribution of ions

The angular distributions of the ion number measured by the charge collector array are shown in Fig. 4-10 for high (Fig. a) and low (Fig. b) contrast pulses. These distributions were obtained with $I_p = 1 \times 10^{15}$ W/cm^2 at 55° incident angle. Each data point corresponds to the position of detector and is determined by integrating the ion current over the time period for which relevant ion component is detected. The horizontal and vertical error bars correspond to the detector solid angle and uncertainty of multiple shot averaging, respectively. To deduce the number of ions, the velocity dependence of ion charge state shown in Fig. 4-9 is assumed to be valid over the angular distribution. The angular distributions of fast and thermal components are obtained separately for the high contrast pulse interaction. The figures show the polar angular distribution of the normalized number of ions emitted with respect to the target normal. No azimuthal dependence was found by the detectors in horizontal and vertical

a High intensity contrast
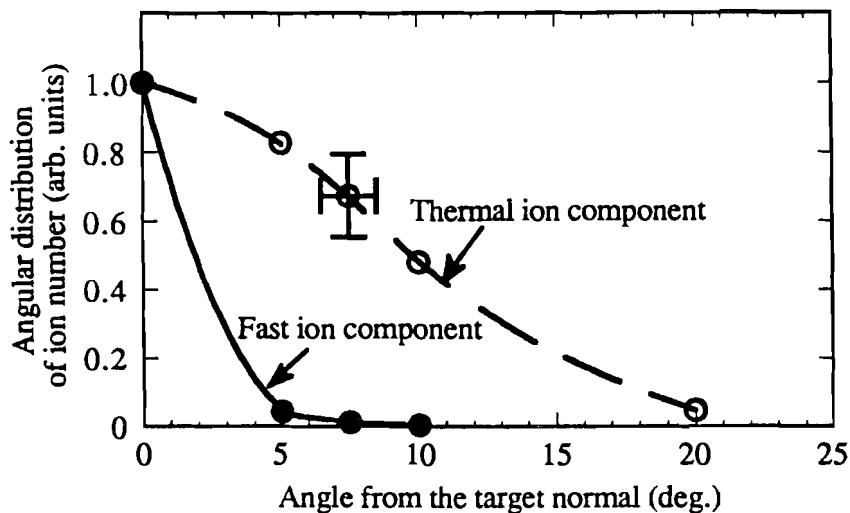
b Low intensity contrast

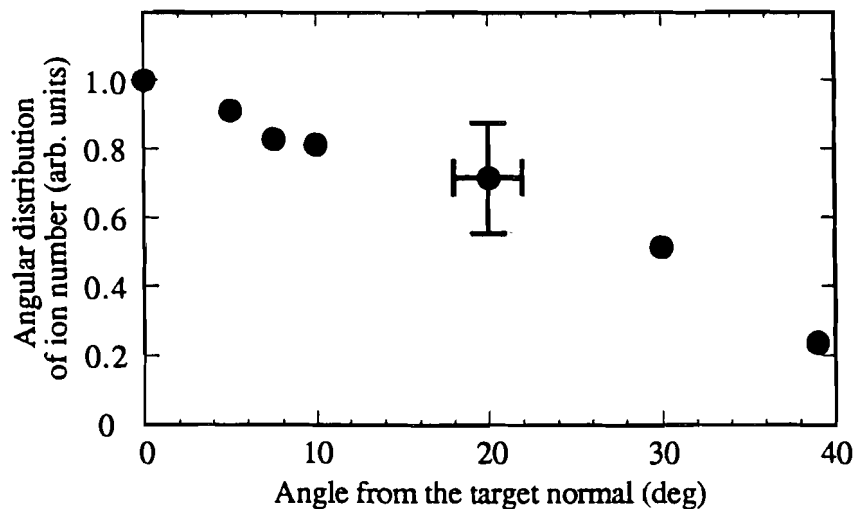Fig. 4-10 Angular distribution of ion blowoff shows interaction pulse contrast dependence. Ion blowoff of the high contrast pulse (Fig. a) forms much narrower plume than that of low contrast pulse (Fig. b). Each point corresponds to the position of detector. Two components from the high contrast pulse have distinctive distribution.

planes so that the target normal is the axis of the symmetry and total number of ions can be calculated from these data alone. The distribution is much narrower from the high contrast pulses and exhibits two distinctive cone angles between the fast (~5°) and thermal ion (~20°) components. The difference in the cone angle will be related to the temperature and directed (kinetic) energy of electrons which accelerate the ions.

IV-3-f Calculation of the electron kinetic energy

An important parameter to be estimated is the total ion (electron) kinetic energy. The ions carry a large fraction (~60%) of absorbed laser energy and reflect the field strength of the resonantly oscillating plasma wave in the high contrast case. The total energy of electrons accelerating the fast ions is calculated by integrating the ion kinetic energy over the fast ion peak in the ion current trace,

$$E_{total} = \int^{fast} \frac{m_i V_i^2(t) N_i(t)}{2} dt = \frac{m_i}{2e} \int^{fast} \frac{V_i(t) I(t)}{Z(t)} dt,$$

where $N_i = I_{eff}(t)/eZ(t)V_i(t)$ is the total ion flux and the effect of ion angular distribution is included in $I_{eff}(t)$. The total fast ion kinetic energy is approximately 20% of incident laser energy, while the difference in absorption between the polarizations appears 30% of incident energy which is about half the total absorption of p-polarization. The discrepancy between the ion and absorption measurements will be resolved by K_α measurements which will be described in the next section. Only a few percent of laser energy appears in the ion kinetic energy from s-polarized light.

The kinetic energy per electron, K_e, is estimated from E_{total} by

$$K_e = E_{total} \Big/ \frac{Z_{Al}}{\bar{Z}} \int^{fast} \frac{I_{eff}(t) dt}{eV_i(t)},$$

where the integration is over the duration of the fast ion component. The denominator is the total number of electrons accelerating the fast ions assuming charge neutrality. Recombination effects shown in Fig. 4-9 are taken into account in $\overline{Z}$. The results are plotted against I_p in Fig. 4-11.
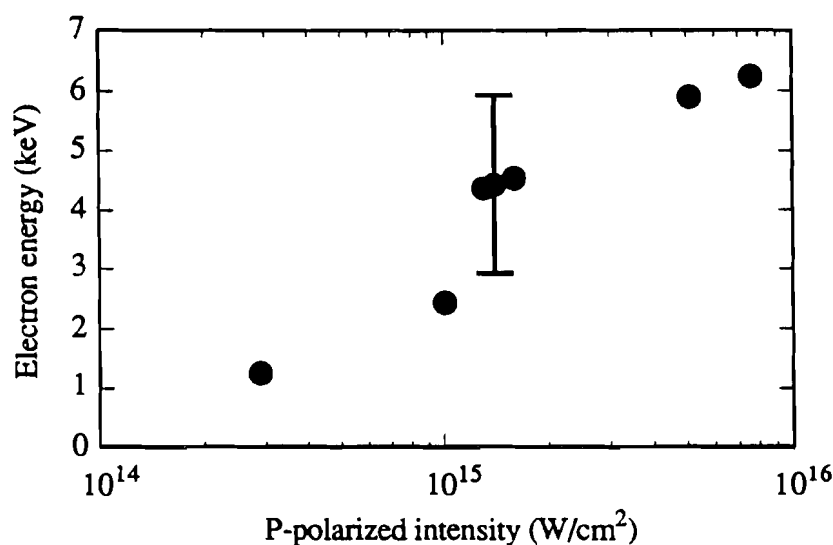
Fig. 4-11 Electron kinetic energy accelerated from the resonantly oscillating fields.

IV-3-g Factors affecting the estimation of electron energy at n_{cr}

There are several factors which lead to the errors in estimating the electron energy. If a fraction of electrons escape from the underdense region before giving their energies to ions then the energy calculated from the ions is underestimated. There is also a group of electrons penetrating into the overdense region and going further through the bulk target. However, these electrons do not contribute to the fast ion acceleration and thus won't affect the kinetic energy estimation. Furthermore, these electrons turn around due to the target potential and can be accelerated by the resonance field again. In other words, electrons accelerated into vacuum transfer their energy to plasma (ion)

expansion whereas electrons penetrating into the bulk target will turn around since plasma can not expand into solid material. An estimation of the energy deposition in the bulk target by the nonthermal electrons is given by the K_α emission measurement.

IV-4 K_α emission

A complementary measurement of the electron kinetic energy was obtained by the K_α emission. The detector was located 15 cm away from the targets and viewing ~30° above the plane of incidence. Figure. 4-12 shows x-ray emissions into all solid angles calculated from the PIN diode signals assuming an isotropic radiation. The error bar corresponds to the uncertainty of the shot-by-shot fluctuation of signal. The K_α emission increases as the p-polarized intensity increases which is consistent with the electron kinetic energy measurements by ions. When the p-polarized intensity is less than 1×10^{15} W/cm^2, the signal is dominated by continuum emission primarily between 3 and 20 keV photon energies (see Fig. 3-16 for detector response). This signal level determines the lowest detection level of the measurement. The dependence of the K_α emission on electron energy will be compared with the electron kinetic energy variation as a function of p-polarized intensity in next chapter.
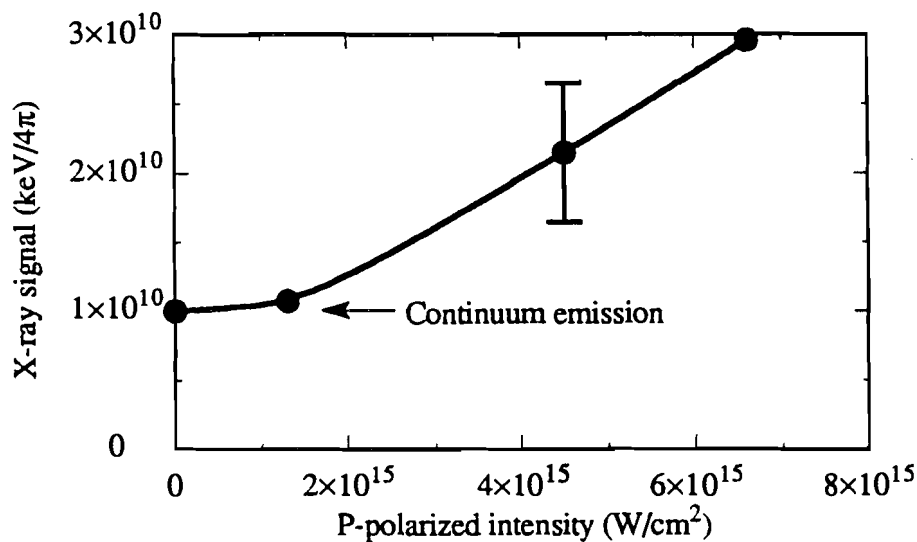
Fig. 4-12 X-ray signal in all solid angles measured by an Al-filtered K_α detector. The signal exhibit a dependence on the p-polarized intensity.

The energy deposition into the solid Al target can be estimated by total K_α emissions using the K_α fluorescence yield.[9] The calculations assume that 4000Å of Al remains solid behind the plasma and electrons consist of 6 keV monoenergetic electrons. In 4000Å thick solid Al, a single 6 keV electron can deposit 4.5 keV of its energy out of which 1×10^{-3} K_α photons are emitted. From Fig. 4-12, the measured total photon number is of the order of 10^{10} which would have been produced by 8×10^{12} electrons. Since each electron deposit 4.5 keV of its energy in the solid Al, the total energy deposition is 6 mJ which is approximately 11% of the incident laser energy and corresponds to the missing energy between the absorption and ion measurements. The estimated energy might have been underestimated since the assumed Al thickness (4000Å) gives the minimum remaining solid during the interaction.

IV-5 Super high energy electrons

Additional measurements has been done on very high energy electrons (>50 keV) using the magnetic electron analyzer (MEA). It is worth noting that this diagnostic is not to measure those electrons responsible to the fast ion acceleration, however, the results of the diagnostic are described since interesting observations have been obtained from the measurement. Out of three channels (50, 250 550 keV), only the 250-keV-channel yields significant amounts of signal. Figure 4-13 shows the signal of the high energy electrons as a function of p-polarized intensity. Detectable amounts of noise were present in the 50- and 550-keV channels when the 250-keV channel detected a significant amount of signal (>10 in the vertical scale) and are indicated as a noise level in the Figure. Since the 250 keV electron deposits more than 95% of its energy in the detector sensitive layer, the PIN diode's quantum efficiency (4×10^{-20} C/eV) [10] can be used to calculate the number of electrons detected. Assuming the detector's solid angle still can be calculated by the detector size and the electron path length and an isotropic distribution of electron, the total number of electrons emitted from the plasmas is calculated to be approximately 2×10^7. This number translates to the total energy of electron, ~8×10^{-4} mJ. This amount of energy can not be attributed to the fast ion acceleration.

Although, the effects of these very energetic electrons on ion acceleration is negligible, it is interesting to note that the onset of these energetic electrons coincides with the saturation of the growth of the fast ion peak (see Fig. 4-4-b). It is also interesting that the electron spectrum is highly monoenergetic. A large target potential due to the energetic electron emission [11] can not be accounted for the monoenergetic electron distribution since it would only shift the electron spectrum. Some speculation on the production of these electrons will be discussed in the next chapter in conjunction with the fast ion saturation.
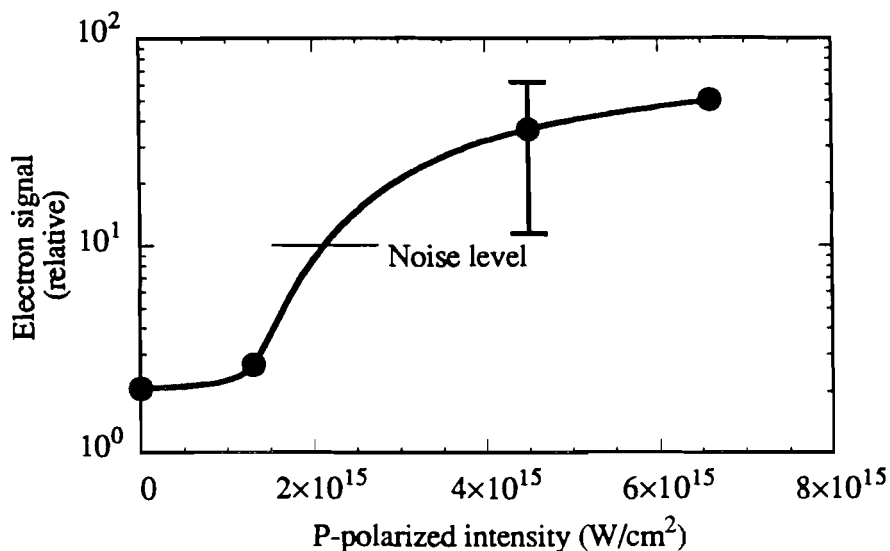
Fig. 4-13 P-polarized intensity dependence of 250 keV electron production.
The lowest level of detection is determined by continuum emissions.

REFERENCES

1 K. R. Manes, V. C. Rupert, J. M. Auerbach, P. Lee and J. E. Swain,
"Polarization and angular dependence of 1.06-μm laser-light absorption by
planar plasmas," Phys. Rev. Lett. 39, 281 (1977).

2 P. B. Corkum, F. Brunel, N. K. Sherman and T. Srinivasan-Rao, "Thermal
response of metals to ultrashort-pulse laser excitation," Phys. Rev. Lett. 61,
2886 (1988).

3 F. C. Young, "Measurements of energetic x rays from laser-produced
plasmas," Phys. Rev. Lett. 33, 747 (1974).

4 J. F. Kephart, R. P. Godwin and G. H. McCall, "Bremsstrahlung emission
from laser-produced plasmas," Appl. Phys. Lett. 25, 108 (1974).

5 W. Priedhorsky, D. Lier, R. Day and D. Gerke, "Hard-x-ray measurements of 10.6-μm laser-irradiated targets," Phys. Rev. Lett. **47**, 1661 (1981).

6 J. P. Freidberg, R. W. Mitchell, R. L. Morse and L. I. Rudsinski, "Resonant absorption of laser light by plasma targets," Phys. Rev. Lett. **28**, 795 (1972).

7 W. Woo and J. S. DeGroot, "Rippling of the critical surface by four-wave processes in a laser-irradiated plasma," Phys. Fluids **23**, 2291 (1980).

8 R. R. Goforth and P. Hammerling, "Recombination in an expanding laser-produced plasma," J. Appl. Phys. **47**, 3918 (1976).

9 M. O. Krause, "Atomic radiative and radiationless yields for K and L shells," J. Phys. Chem. Ref. Data **8**, 307 (1979).

10 Quantrad Co., PIN Si diode detector catalog (1989).

11 N. A. Ebrahim and C. Joshi, "Electron heating in high intensity CO_2 laser-plasma interaction," Phys. Fluids **24**, 138 (1981).

CHAPTER V

Analysis and discussion

V-1 Introduction

The primary experimental results are summarized as the following. The high intensity contrast interaction produces the fast ion blowoff whose flux strongly depends on the p-polarized intensity alone (not on the total laser intensity). This fast ion production and polarization dependence of ion blowoff characteristics appear only in the high contrast interactions. The plasma temperature and electron kinetic energy are calculated from the ion velocity distribution and the energy/number measurements of ions. These measurements show that the suprathermal electrons accelerating the fast ions consist of a fairly monoenergetic distribution (typically 6 keV kinetic and 500 eV thermal energy). Additional measurements on K_α emission estimate that about 10% of laser energy is absorbed by suprathermal electrons which go into the bulk of target. This estimation together with the total fast ion energy measurement reveal that the absorption difference between the s- and p-polarization can be accounted for by the suprathermal electrons.

In this chapter, the above experimental results are interpreted in terms of the ponderomotive acceleration of the suprathermal electrons in the resonantly enhanced laser field at the critical surface. In this model, the enhancement of the p-polarized laser field is determined by the plasma-wave dispersion. This spatially localized field accelerates the oscillating electrons to its potential energy (up to 6 keV) and expels them from the resonance region. These high energy electrons leave the immobile ions behind and build up a ambipolar field which then accelerates the ions. These ions eventually catch up with the electrons and appear as the fast ions. Most of the energy which initially resides in the electron fluid is transferred to the ion kinetic energy. These high

energy particles form an underdense plasma which determines the scale length and the enhancement of the resonance field.

Based on this picture, the amplitude of the resonantly oscillating electric fields of plasma wave at the critical surface is calculated from the ion kinetic energy measurement and compared with a theoretical calculation which includes plasma-wave coupling effects. The significance of the p-polarized laser electric field to the absorption is examined in terms of the thermal component of ions and incident angle dependence of absorption. The monoenergetic feature of the accelerated electrons by the ponderomotive force is confirmed by using energy and angular distribution of ion measurements and K_α emissions. The picture of the ponderomotive acceleration of electrons in the resonance region is then examined against the wavebreaking mechanism in cold plasma limit to show the it is consistent with the plasma conditions observed by various diagnostics. Finally plasma depletion condition is examined as a cause of the saturation of fast ion peak growth and some speculation on the mechanism of the super energetic electrons is given. To avoid confusion, it is noted that the experimental observations used in this chapter refer to those of the high contrast interaction unless otherwise mentioned.

V-2 Plasma density scale length

The density scale length of underdense plasma, $L_n \equiv (\nabla n_e/n_e)^{-1}$, an important parameter in determining the coupling between the incident laser and resonantly oscillating electric field at the critical surface, can be deduced from the the total number of fast ions. This assumes that the high energy electrons emitted from the critical surface accelerate ions through an ambipolar field and together form an underdense plasma. This assumption has been found to be a self-consistent picture of the present plasma condition. The total number of fast ions, N_{fast}, is calculated using the angular distribution and velocity dependent ion charge state,

$$N_{fast} = \int^{fast} \frac{I_{eff}(t)}{eZ(t)V_i(t)} dt \ .$$

Here $I_{eff}(t)$ is an integrated ion current which includes the angular distribution according to the results shown in Fig. 4-10-a. The integration is over the period of fast ion detection. The angular distribution is assumed to be independent of I_p. Using the spot area of the focused beam, A_{spot}, and assuming an exponential density profile, L_n is related, after an integration over space, to N_{fast} by;

$$N_{fast} = A_{spot}L_n n_{cr},$$

where n_{cr} is the electron density at the critical surface.

The I_p dependence of L_n shown in Fig. 5-1 saturates at $L_n \approx 2000\text{Å}$ or total ion number of 6.6×10^9 when $I_p > 10^{15}$ W/cm^2, indicating the upper limit of ion number which can be drawn from the plasmas during the interaction. One of the simplest interpretations for the cause of the saturation would be the depletion of plasma particles in the resonance region. This mechanism will be discussed later in conjunction with a density cavity formation. $L_n \approx 2000\text{Å}$ is consistent with the plasma expansion at the ion sound velocity calculated with $K_e = 6$ keV replacing electron temperature, that is,

$$L_n = \tau_{laser} \sqrt{\frac{Z_{Al} K_e}{M_{Al}}} \ .$$

The total number of ions is larger in low contrast case than in high contrast case by a factor of five. The larger ion number in the low contrast case is consistent with the polarization independence of absorption and ion emission characteristics, since the prepulse ($\approx 10^{13}$ W/cm^2) creates a relatively long scale underdense plasma which attenuates the EM waves before they reach the critical surface and obscures the polarization effects. The rippling of the critical surface developing during the prepulse also blurs the polarization effects. Assuming the underdense plasma produced by the prepulse is responsible to most of the absorption and appears as the thermal component

in the ion current, the scale length is estimated to be approximately 1 μm in the low

contrast case. Since the x-ray measurements estimate the hot electron energy to be 3%

at most and the incident angular dependence of absorption exhibits the trend similar to

that of long scale length plasmas where inverse bremsstrahlung prevails, collisional

absorption seems to be a dominant absorption mechanism for the low contrast

interactions. This explains why the low contrast pulse interaction exhibits no

polarization dependence.
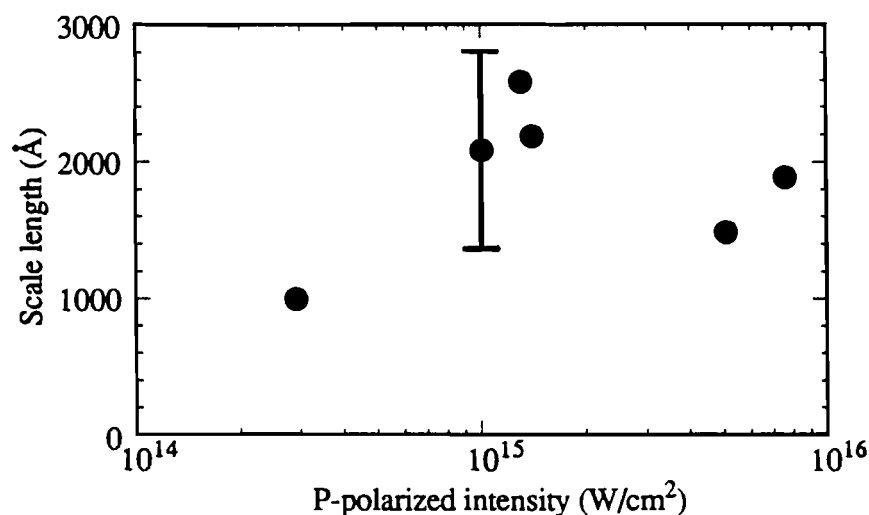
Fig. 5-1   Plasma density scale length, $L_n \equiv (\nabla n_e/n_e)^{-1}$, calculated from the total
number of fast ion component. An exponential density profile
which is consistent with an isothermal expansion is assumed.

V-3 Calculation of the intensity enhancement at the critical surface

Since the accelerated electron energy equals the ponderomotive potential which is

proportional to the laser intensity, the electric field strength of the resonantly oscillating

field can be calculated from the electron kinetic energy. The measured electron kinetic

energy, shown in Fig. 4-11, is converted to laser electric field (intensity) by Eq. 2-28 and shown, in terms of enhancement factor, in Fig. 5-2 indicated by closed circles.

The theoretical calculation of the enhancement of laser electric field at the critical point includes two factors; the plasma-wave coupling effects and the tunneling of the electric field from the turning point to the critical point. As the resonance field grows at the critical point, the pressure gradient associated with the plasma wave broadens the localization of electrons (the width of the resonance field), thus reduces the otherwise infinitely growing peak field. This effect, the plasma-wave dispersion effect, is expressed, in terms of the field enhancement fact, by $\left(\frac{L_n}{\lambda_D}\right)^{2/3}$ as first derived by

Ginzburg [1] (see Eq. 2-20). The EM wave decay from turning point to the critical surface is estimated to be ~20% by solving a wave equation numerically (see section II-1). Thus the intensity enhancement is estimated to be $\eta_t^2 \left(\frac{L_n}{\lambda_D}\right)^{4/3}$.

Using experimental values of L_n and T_e (for λ_D) (see Fig. 5-1 and 4-7, respectively), an I_p dependence of the intensity enhancement is obtained and shown by open circles in Fig. 5-2. The theoretical values are in a good agreement with the experimental values showing that, in the present experimental condition, the high energy electrons are accelerated by the ponderomotive potential in the resonance field at the critical region whose amplitude is determined by the plasma-wave dispersion effects. The enhancement due to the plasma-wave dispersion depends both on the scale length and the plasma temperature (the Debye length). The observed decline of the enhancement at the higher intensity can be accounted for by the higher temperature (the longer Debye length) and the saturation of the growth of the scale length (see Fig. 5-1).
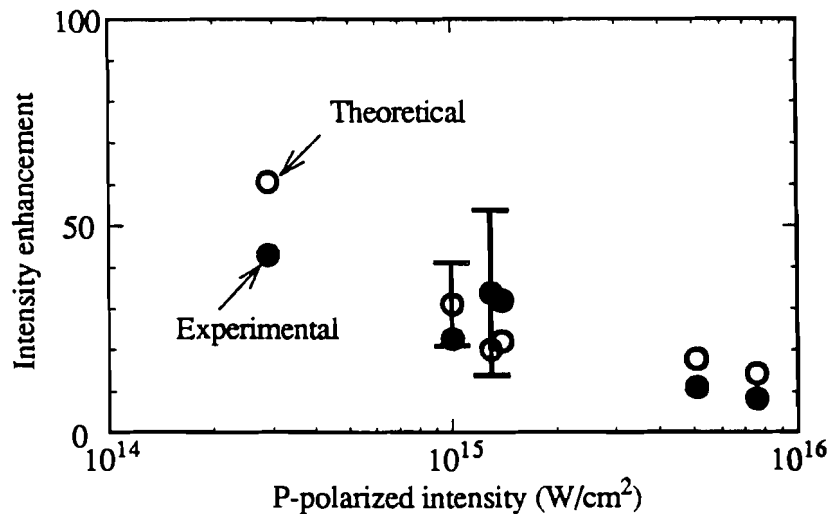
Fig. 5-2   Comparison of intensity enhancement factors estimated from experiments and calculated using plasma wave convection effects. Closed and opened circles represent the experiment and calculation, respectively.

V-4 Resonance field amplitude and p-polarized light absorption

The significance of the resonantly oscillating field and the concomitant particle acceleration on p-polarized absorption can be observed by comparing the absorption measurements and ion kinetic energy measurements as well as examining the incident angle dependence of p-polarized absorption. The absorption measurements show 10-40% higher absorption for p-polarization than for s-polarization depending on the incident angle, θ_{inc} (see Fig. 4-1-b). This difference is 30% for $\theta_{inc} = 55°$ and appears to be comparable to the total ion kinetic energy, approximately 20% of laser energy. A possible explanation of the 10% discrepancy is discussed in the next paragraph. It has been shown that the total ion energy is originally absorbed as an electron direct energy accelerated in the ponderomotive potential and thus should reflect the laser energy

absorption in the critical region. Thus, at least 20% of absorption is due to the ponderomotive acceleration.

The 10% discrepancy can be explained by the fact that the ion current measurement only counts the ions expanding toward the vacuum, therefore, the number of electrons deduced from this measurement is counted only for those electrons accelerated toward the vacuum. Because of the symmetrical structure of the ponderomotive potential, there is a group of electrons flowing into the bulk of target which is not to be detected by the charge collectors. In fact the K_α measurements estimate approximately 11% of energy deposited by the nonthermal electrons in the bulk target. The energy of these missing electrons can be attributed to the 10% discrepancy between the absorption and ion measurements. Combining this 10% energy and 20% ion energy obtains 30% of absorption due to the ponderomotive potential.

These electrons would deposit their energy in the overdense region and produce more thermal ions than s-polarization does. This effect is apparent in Fig. 5-3 where only the thermal ion component is extracted from the ion trace of p-polarization (see Fig. 4-3-b). The extraction is done by subtracting the extrapolated fast ion peak from the overall current trace. The thermal component from s-polarization is reproduced as a comparison (broken line). The figure clearly shows that p-polarization produces more thermal ions than s-polarization, suggesting an additional heating process in p-polarization, that is, heating by the slowing down of the electrons accelerated into the overdense region by the ponderomotive force. These undetectable (missing) electrons, however, do not affect the electron (the ponderomotive potential) energy measurement since only a specific energy is calculated. The 10% of missing energy out of 30% additional absorption in p-polarization indicates that one third (not a half) of electrons accelerated from the resonance region deposit their energy into bulk target. This asymmetry is due to the effects of the plasma pressure in the overdense region. The electrons flowing into the overdense region build up an ambipolar field, however, the

ions in the critical region do not follow them because of the higher pressure and pull the electrons back to the resonance region. On the other hand, the electron flowing opposite direction can escape from the plasma while dragging ions with them.
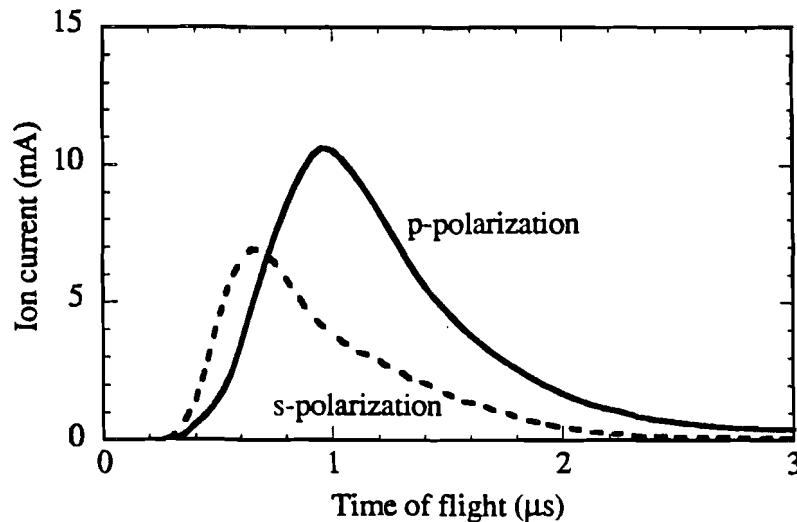

Fig. 5-3   Thermal component of ion current of p-polarization is extracted by
          subtracting the fast ion component from the ion current trace shown
          in Fig. 4-3. Ion trace of s-polarization (broken line) is shown as a
          comparison .

The effects of the p-polarized laser electric field component on the laser absorption can be seen by extracting the additional absorption due to p-polarization from the absorption measurements. The absorption measurements shown in Fig. 4-1-b exhibit a constant absorption for s-polarization and angle dependent absorption for p-polarization. The angle dependent absorption can be obtained by subtracting the s-polarization absorption from that of p-polarization. Since the enhanced p-polarized laser field accounts entirely for the differential absorption, the angle dependent absorption is related to the p-polarized intensity. The way the angle of incidence determines the intensity is two folds: 1) effects of focusing spot size which are

proportional to $\cos\theta$ and 2) a $\sin^2\theta$ dependence which comes from refraction of the light wave in plasma (see Eq. 2-11). Therefore the differential absorption can be compared with $\cos\theta\sin^2\theta$. Here electric field decay from the turning point to the critical surface is assumed to be constant over the angle of incidence because of the short density scale length. Fig. 5-4 shows the comparison of the differential absorption and $\cos\theta\sin^2\theta$ dependence. The discrepancy between the measurements and calculations is probably due to the variation of enhancement, i. e. a slight difference in η_t.
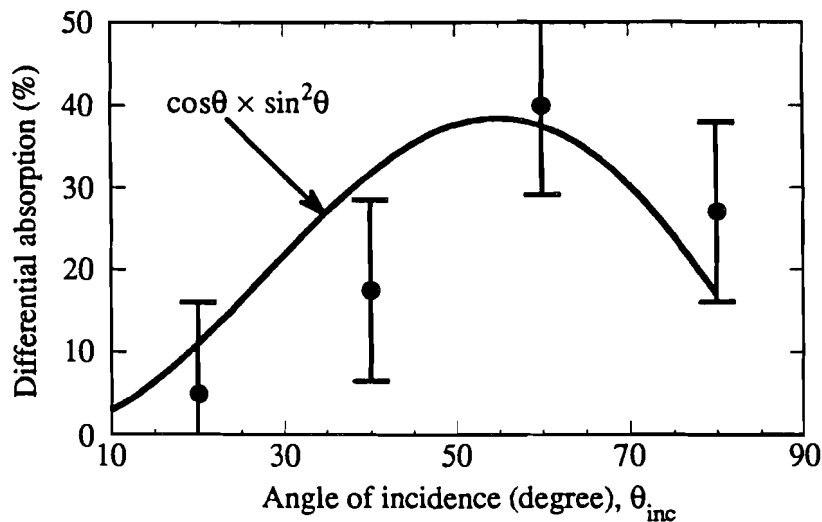
Fig. 5-4   Comparison of p-polarized intensity and the pure p-polarized absorption (p-polarization minus s-polarization). Since the spot size and p-polarized electric field are proportional to $1/\cos\theta$ and $\sin^2\theta$, the p-polarized intensity or the enhanced intensity is proportional to $\cos\theta\sin^2\theta$ assuming a constant enhancement. This figure is consistent with the picture that the additional absorption in p-polarized light appears as ion kinetic energy due to the enhanced intensity.

V-5 Monoenergetic feature of accelerated electrons

The unique feature of the nearly monoenergetic electron velocity distribution can be deduced from the ion measurements which are supported by several other experimental observations. The first experimental evidence is that ion kinetic energy measurements reveal the existence of high energy electrons of 1-6 keV (see Fig. 4-11) whereas ion velocity distribution indicates a relatively low temperature of 70-450 eV (see Fig. 4-7). A bulk of electrons with small thermal spread traveling at a few keV of energy is a consistent physical picture of the observation. This electron distribution can be described by a shifted Maxwellian distribution, shown in Fig. 5-5,

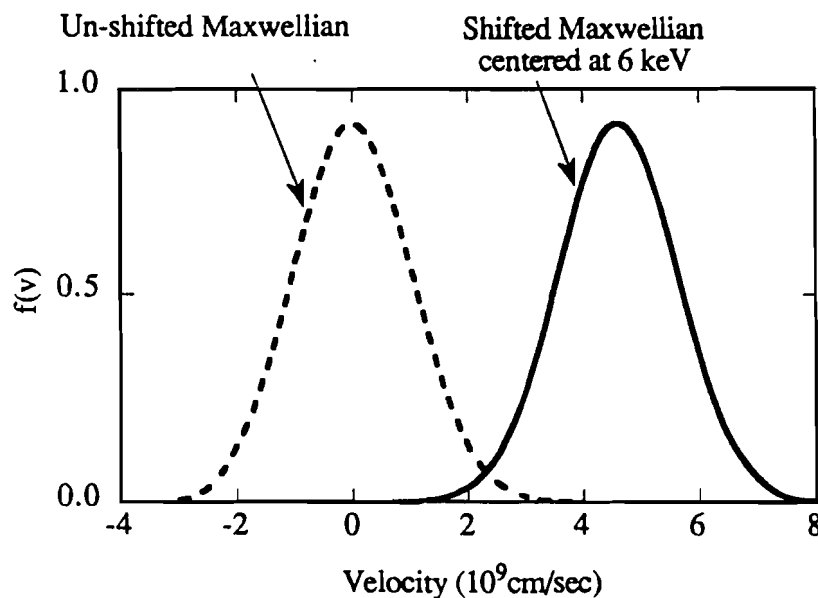$$f(v) \propto \exp(-m_e(v_e - v_{shift})^2/2k_BT_e).$$

Fig. 5-5   Shifted (the solid line) and unshifted Maxwellian (the broken line). Both distributions correspond to 500 eV temperature. The shifted Maxwellian is centered at the 6 keV electron energy.

The energy of the accelerated electron is confirmed by the K_α emission measurements. Figure 5-6 shows the comparison of K_α emission measured by PIN K_α detector (closed circle reproduced from Fig. 4-13) and calculated values (solid line) which are expected from monoenergetic electrons distribution. The calculation is based on an electron energy deposition in solid materials calculated by Spencer and Berger[2,3] and measured K_α fluorescence yields.[4] 4000Å thick solid Al is assumed as a K_α emitter. The p-polarized intensity dependence of electron energy is taken from Fig. 4-11. The K_α detection is limited by the continuum emission (value 3 in the ordinate) and only signals with intensities larger than 1×10^{15} W/cm^2 are compared.
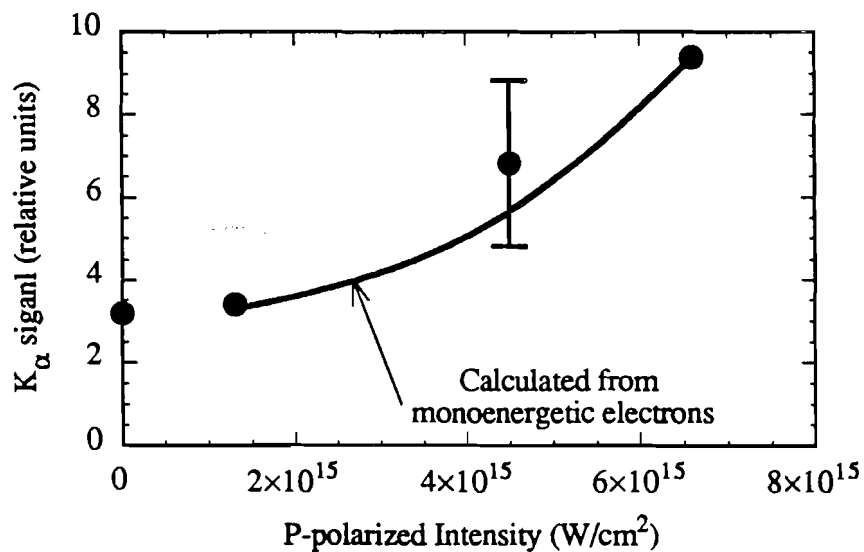
Fig. 5-6   Comparison of measured K_α signal and calculated signal using monoenergetic electron distribution. Data points (closed circle) are reproduced from Fig. 4-12. The solid line corresponds to the calculation based on monoenergetic electron distribution.

The second experimental evidence is the narrow cone angle of the fast ion angular distribution. The ratio of the thermal energy to the electron kinetic energy leads to an

angle $\theta_{cone} = \tan^{-1}\left(\frac{1}{2}\sqrt{\frac{T_e}{K_e}}\right) \approx 7°$, when $T_e = 0.45$ eV, $K_e = 6$ keV. The very low

thermal energy compared with the kinetic energy agrees with the measured cone angle of the fast ion component (see Fig. 4-10-a). This nearly monoenergetic electron distribution is used to identify the particle acceleration mechanism in the critical region in the next section.

Additional supporting evidence comes from the x-ray continuum measurements where a strong reduction of emission has been observed from low contrast to high contrast interactions. The cause of the reduction might be two fold. First, the reduction can be attributed to the absorption mechanism and the plasma cooling time. In the low contrast interaction the laser absorption takes place mainly in the underdense plasma through collisional absorption which uniformly heats the plasma. This may produce a large volume x-ray emitter. The spatially uniform absorption creates gentle temperature gradient which lowers the heat conduction and lengthens the plasma cooling time.[5] On the other hand, in the high contrast interaction, the laser absorption takes place in a very narrow region in the vicinity of the critical surface and the absorbed energy is converted to the electron kinetic energy. The high energy electrons quickly take the absorbed energy away from the absorption region without heating the plasma and transfer their energy to the ions. The experimental observation that the total absorption does not change from the low contrast interaction to the high contrast whereas emitted ion energy increases from a few percent to 20% of the laser energy is consistent with the above interpretation.

The difference in the characteristics of high energy electrons produced in the low and high contrast interactions can be compared by examining the electron energy dissipation processes. These processes are: 1) collision with other charged particles and resulting radiation, or 2) energy transfer to plasma expansion through an ambipolar electric field set by charge separation. The dominant process between the two is

determined by the electron velocity distribution since the cross section of bremsstrahlung is inversely proportional to velocity squared, that is, faster electrons lose more energy to plasma expansion and less by radiation.

The creation of high energy electrons has been substantiated by the co-incidence of x-ray continuum emission and fast ion blowoff.[6] However the present ion spectrum shows the existence of the energetic electrons while the x-ray measurements exhibit the reduction of x-rays from the low contrast interaction to the high contrast pulse interactions. These experimental observations can be examined to characterize the electrons produced in the present conditions by comparing x-ray emissions from electrons of 6 keV kinetic energy with a few hundreds eV temperature and electrons of 6 keV temperature yet the total electron energy kept same for both cases.

The reduction of x-ray emission in high intensity contrast interaction can be explained by the dependence of x-ray (continuum) emission on electron energy distribution. The power spectra of bremsstrahlung emitted by a single electron per unit length in an ion density n_i is expressed by a differential cross section $\dfrac{d\sigma}{d\omega}$,[7]

$$\omega \frac{d\sigma}{d\omega} = \frac{16}{3\sqrt{3}} \, n_i \, \alpha \, \frac{c^2}{v^2} \, \pi \, (Z r_e)^2,$$

where α, v_i, r_e are the fine structure constant, ion velocity and classical electron radius, respectively. As is seen in the expression, the emission is proportional to the ion density and inversely to the velocity squared. Thus if the accelerated electrons consist of monoenergetic energy distribution, the total number of photons is less than would be emitted from a Maxwellian distribution. This is because, in a Maxwellian distribution, there are more electrons with energies less than 6 keV which emit more photons than monoenergetic 6 keV electrons. Therefore, the simultaneous observation of fast ion acceleration and the reduction of x-ray emission is consistent with the ponderomotive acceleration of electron and resulting beam-like energy distribution. The difference in

emitted power depends on the detail of the electron distribution (total number and temperature). This argument is valid only when total number and energy of electron are comparable in both cases and the plasma is thin enough so that the monoenergetic electron won't thermalize before a substantial amount of energy converted to radiation or ion expansion.

V-6 The ponderomotive acceleration and wavebreaking for producing the energetic particles

The observed characteristics of high energy electrons can distinguish the ponderomotive acceleration from wavebreaking in two aspects. First the ponderomotive force accelerates electrons to its potential and generates monoenergetic electron emission in ∇E^2 direction, while the wavebreaking produces a high energy tail of Maxwellian distribution.[8, 9] As is described above, the observation of high energy electrons with relatively low temperature indicates a nearly monoenergetic electron distribution and suggest the ponderomotive force as a electron acceleration mechanism.

Second the number of electrons accelerated through the ponderomotive potential is larger than that from wavebreaking. The typical ratio of hot electrons to cold background electrons number in wavebreaking is a few percent [10], while the ponderomotive potential could deplete the electrons in the critical region.[9, 11] As will be discussed later, the number of ions measured in the experiments is comparable to the number of ion existing in the vicinity of the critical density and suggests that almost all of the particles participate in the acceleration process which contrasts to wavebreaking picture. Comparison of the number of fast ions between the low contrast and high contrast substantiates the difference of electron acceleration characteristics between wavebreaking process and the ponderomotive acceleration, that is, the ponderomotive acceleration (plasma-wave coupling limit) for high contrast interaction and wavebreaking electron heating for low contrast interaction.

The applicability of plasma-wave coupling effects in the high contrast interaction can be tested against the plasma conditions. The dominant mechanism between the cold plasma wavebreaking and the warm plasma-wave coupling limit (the ponderomotive acceleration) depends on plasma temperature. For instance, the plasma can be said to be cold if the convection of plasma wave energy is ignorable compared with the energy input from E_d. In this case highly localized resonance field can reach the wavebreaking condition described in section II-2. In Fig. 5-7, the experimental conditions are applied to the criteria for wavebreaking (Eq. 2-23) and plotted (indicated by open circles). The cross points are the ratio of the incident laser field in the form of electron oscillating velocity to the electron thermal velocity. η is calculated by integrating Eq. 2-9 and 10 with a measured scale length, L_n. Wavebreaking dominates the process when the plasma conditions fall below the solid line. All of the high-contrast experimental points fall in the region where plasma is warm and the amplitude of the resonantly oscillating field is determined by the plasma-wave coupling effects, that is, the ponderomotive acceleration is operative in the high contrast interaction.
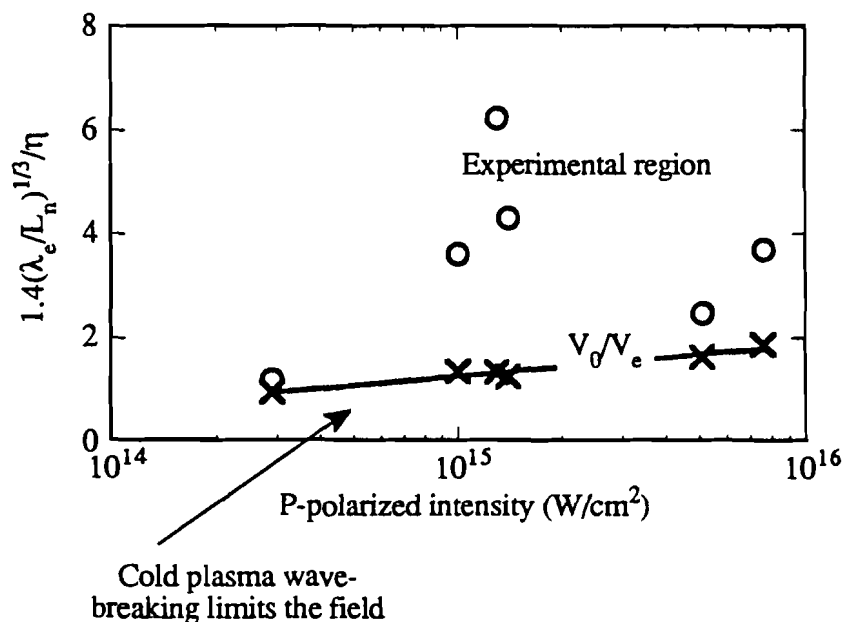
Fig. 5-7   Cold plasma wavebreaking region and warm plasma-wave coupling region determined by Eq. 2-23. The crosses indicate the ratio of incident laser field ($V_0 m_e \omega/e$) to the electron thermal velocity and the solid line bounds the two regions. The experimental points fall in the plasma-wave coupling region.

V-7 Thermal component of high contrast s-polarized light interaction

Although, the thermal peaks of the ion current are less prominent than the fast peaks, they give some useful insights on the energy transport and the plasma conditions. Here the thermal peaks are compared between two polarizations for the high contrast case and two intensity contrasts.

As is presented in Fig. 5-3, the thermal peak from p-polarized light is larger than that from s-polarization suggesting an additional heating of the overdense plasma by the nonthermal electrons accelerated from the resonance region. This additional heating

was also observed by K_α emission which is consistent with the existence of the nonthermal electrons and complemented the ion measurements. Thus the thermal peak from p-polarized light is produced by both thermal conduction and nonthermal electron conduction flowing toward the overdense region while, in s-polarized interaction, it is produced by thermal rarefaction wave. Only a few percent of the energy is accounted for by the ion energy whereas 20% overall absorption from s-polarization suggests that most of the absorbed energy is dissipated through thermal convection. This is expected to be very strong due to the steep density gradient in high contrast interactions.

It is interesting to note that the thermal component in s-polarization is much larger in current and energy, compared with that of low contrast interactions (see Figs.4-3), even in the absence of the ponderomotive acceleration. The ion acceleration in s-polarization with high contrast pulses can be attributed to the existence of a very steep pressure gradient. The gradient is expected to be even steeper than p-polarization case since no additional accelerating mechanism such as the ponderomotive force is present. The thermal rarefaction wave could lead to such high velocity expansion with extremely steep density gradient. It is calculated from the angular distribution and ion charge state measurements that the amount of ions consisting the thermal peak in s-polarization corresponds to a 100~200Å of solid target thickness, which is approximately one tenth of that of p-polarization. The thickness of the target from which ions are produced equals to the skin depth of metal suggesting that energy deposition takes place within a very limited region. However, because ions expand at such high velocities and current is proportional to the velocity, the ion current trace appears much larger than that from low contrast interactions.

V-8 The plasma depletion in the critical density and a density cavity

When I_p exceeds 5×10^{15} W/cm^2, the growth of the fast ion component saturates while the thermal component keeps growing (see Fig. 4-4). These observations

indicate the onset of new interaction mechanisms at that intensity. Plasma particle depletion and concomitant cavity formation would be one candidate for the interpretation of the fast ion saturation. Note that the ponderomotive acceleration is still operative in this intensity range and that the plasma depletion and cavity formation are additional. To examine these possibilities, the structure (spatial width) and number of particles in the region where the ponderomotive force is acting need to be determined.

The spatial width of the resonantly oscillating field, W_{peak} is determined by the largest of $(L_n \lambda_D{}^2)^{1/3}$, $v_c L_n/\omega$, and X_{osc}, [12] where v_c and X_{osc} are the collision frequency and electron quiver amplitude, respectively. For the present plasma condition, $(L_n \lambda_D{}^2)^{1/3}$, the plasma wave convection, determines W_{peak} entirely and, with $I_p = 5 \times 10^{15}$ W/cm^2, $(L_n \lambda_D{}^2)^{1/3} \approx 350$Å. The maximum ion number which can be drawn from the critical region is the sum of ions existing in the critical region and flowing from the overdense region. The former is estimated as $n_{cr} A_{spot} W_{peak}/Z_{Al}$ yielding 2×10^9 ions, while the latter is given by $n_{cr} A_{spot} C_s \tau_{laser}/Z_{Al} = 9 \times 10^9$ ions with $T_e = 250$ eV. Thus the saturation of the number of fast ion component takes place approximately at 1×10^{10} ions which is reasonably close to the observed value of 8×10^9 ions. Once plasma particles are depleted from the resonance region, the density cavity forms there and traps incident laser electric field since it is surrounded by the critical density. The trapped fields accumulate their energy and the enhancement further grows if the inertia of ions holds the field pressure. This extremely high electric fields in the cavity accelerate electrons to even higher energy than resonantly oscillating field.

From the electron energy observed by the MEA, one can calculate the enhanced field strength and examine if this picture is consistent with the experimental condition. Once density cavity forms and EM wave begins to accumulate its energy, the ponderomotive picture is no longer valid because the width of the oscillating field is determined by the cavity width which has been set up by resonantly oscillating field,

$W_c = X_{osc}$ at the enhancement of ≈ 10 and any further enhancement due to the cavity formation expels electron out of the cavity region instantaneously.

The energy of electrons accelerated by the strong electric field in the cavity well exceeds the classical limit and requires a relativistic treatment. The electron acceleration with relativistic mass correction is

$$F = m_0 \alpha \gamma^3,$$

where $\gamma = \left\{ 1 - (v/c)^2 \right\}^{-1/2}$ is the relativistic factor. The acceleration of electrons in an electric field, $E(t)$, is given by,

$$\alpha = \frac{dv}{dt} = \frac{eE(t)}{m_0} \{(1 - (v/c)^2)\}^{3/2}.$$

This equation is numerically integrated assuming that spatially uniform $E(t)$ depends on time like $E_c \cos \omega t$ where E_c is the electric field in the cavity and that electron acceleration takes place only within the cavity. The intensity enhancement in the cavity, η_c is defined as $E_c^2 = \eta_c E_0^2$, where E_0 is the vacuum laser electric field. The final electron velocity from the cavity is calculated as a function of η_c and plotted in terms of corresponding relativistic energy in Fig. 5-8.

The figure shows that the production of the 250-keV electrons observed in the experiments requires a cavity enhancement of 1800. Balancing the incident laser energy and the accumulating electric field energy density gives the time required for such field development,

$$c\frac{E_0^2 \tau_{ac}}{4\pi W_c} = \frac{E_0^2}{8\pi} \eta_{enhance.}$$

where W_c is the width of cavity and τ_{ac} is the accumulating time. It takes 100 fs to build up 1800 times intensity enhancement in cavity which is only a fraction of the pulse duration and thus there is enough time for the laser to build up such a field strength. This additional absorption process further deposit laser energy into the

overdense region and increases the thermal ion production which may explain the ion current traces with $I_p > 5 \times 10^{15}$ W/cm^2.

The cavity formation at the critical surface seems to be a reasonable interpretation for the saturation of fast ion peak. The trapped EM wave in the cavity accumulates its energy and enhances the field amplitude. This extremely enhanced field (~2000 times) produces highly relativistic electrons which are consistent with the observations of 250-keV electrons. The formation of a cavity has been observed by both numerical simulation [9] and microwave experiments.[13, 14] Using an ion probe in microwave plasma, Wong et.al.[11] have simultaneously observed 700 times intensity enhancement and $\Delta n/n = 30\%$ density depression. The enhanced field amplitude can be estimated by the electron energy produced after a cavity forms.
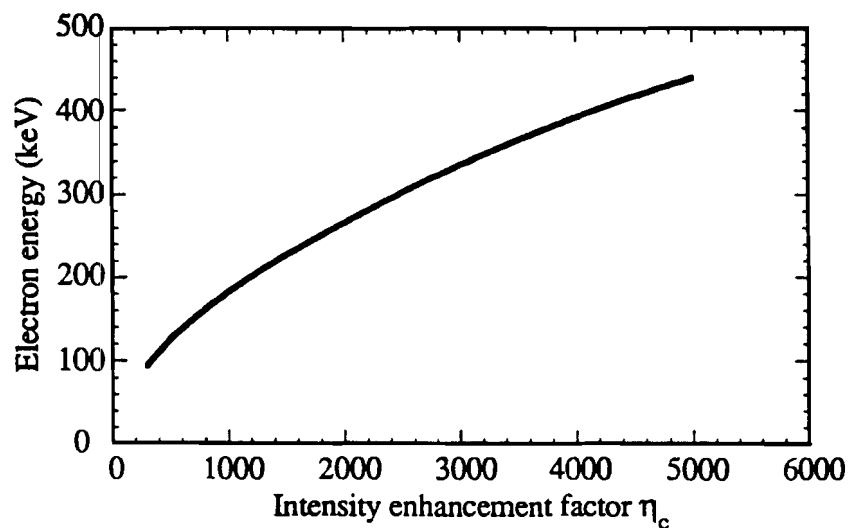

Fig. 5-8   Relativistic electron energy accelerated in the cavity enhanced field
as a function of the cavity enhancement factor.

REFERENCES

[1] V. L. Ginzburg, *Propagation of Electromagnetic Waves in Plasma*, (Gordon and Breach, 1961).

[2] L. V. Spencer, "Energy Dissipation by Fast Electrons," (United States Department of Commerce, National Bureau of Standards, 1959).

[3] M. J. Berger and S. M. Seltzer, "Tables of energy losses and ranges of electrons and positrons," (NASA, 1964).

[4] M. O. Krause, "Atomic radiative and radiationless yields for K and L shells," J. Phys. Chem. Ref. Data **8**, 307 (1979).

[5] M. M. Murnane, H. C. Kapteyn and R. W. Falcone, "Sub-picosecond laser produced plasmas," Nucl. Instr. and Meth. B **43**, 463 (1989).

[6] C. Joshi, M. C. Richardson and G. D. Enright, "Quantitative measurements of fast ions from CO_2 laser produced plasmas," Appl. Phys. Lett **34**, 625 (1979).

[7] I. H. Hutchinson, *Principles of plasma diagnostics*, (Cambridge university Press, Cambridge, 1987).

[8] B. Bezzerides, S. J. Gitomer and D. W. Forslund, "Randomness, Maxwellian distribution, and resonance absorption," Phys. Rev. Lett. **44**, 651 (1980).

[9] K. G. Estabrook, E. J. Valeo and W. L. Kruer, "Two-dimensional relativistic simulations of resonance absorption," Phys. Fluids **18**, 1151 (1975).

[10] L. M. Wickens and J. E. Allen, "Ion emission from laser-produced plasmas with two electron temperature," Phys. Rev. Lett. **41**, 243 (1978).

[11] A. Y. Wong and R. L. Stenzel, "Ion acceleration in strong electromagnetic interactions with plasmas," Phys. Rev. Lett. **34**, 727 (1975).

[12] D. D. Meyerhofer, "The interaction of high intensity lasers with short scale-length plasmas," in the Abstructs of *21st Annual Anomalous Absorption Conference*, (Banff, Alberta, Canada, 1991).

[13] H. C. Kim, R. L. Stenzel and A. Y. Wong, "Development of "Cavitons" and Trapping of rf Field," Phys. Rev. Lett. **33**, 886 (1974).

[14] R. L. Stenzel, A. Y. Wong and H. C. Kim, "Conversion of electromagnetic waves to electrostatic waves in inhomogeneous plasmas," Phys. Rev. Lett. **32**, 654 (1974).

Concluding remarks

VI-1 Summary

Picosecond laser-plasma interaction was studied experimentally using a 1-ps, 1-μm laser pulse with intensity range from 10^{14} to 10^{16} W/cm^2 irradiating solid Al targets. It was found that the intensity contrast of interacting pulse strongly affects the interactions. Two intensity contrasts were used in the experiments: 1) low contrast pulse interaction where the picosecond pulse interacts with a preformed plasma, and 2) high contrast ($>10^5$) pulse interaction where the picosecond pulse interacts with a solid target directly and a subsequent short-density-scale length plasma. The low contrast pulse interactions exhibit characteristics similar to those of long pulse plasma interactions. On the other hand, the high contrast interactions exhibit a clear laser polarization dependence and produce high energy electrons and ions. Therefore, the primary attention of the investigation has been paid to the high contrast interaction.

A number of plasma diagnostics have been used to characterize the interaction extensively. They include ion charge collectors, an integrating sphere (absorption), and a K-edge filtered x-ray spectrometer. The charge collectors were chosen as a primary plasma diagnostic since they can provide important plasma parameters such as electron temperature, total number and energy of ions (electrons). These data were obtained by characterizing the ion blowoff in terms of the ion velocity distribution, the angular distribution of ions, and the velocity dependence of ion charge state. The absorption and x-ray measurements supplemented the ion diagnostics.

The ion blowoff diagnostics and the comparison with other diagnostics in the high contrast interaction give the following observations.

1) the strong emission of fast ions with ~100 keV of kinetic energy.

2) the emission of the fast ion depends entirely on the p-polarized component of laser electric field and not the laser energy.

3) the fast ion component carries approximately 40% of the absorbed laser energy.

4) initial kinetic energy of the electron that accelerates the fast ion is as high as 6 keV.

5) the electron distribution is fairly monoenergetic with temperature up to 450 eV, relatively cold compared to the kinetic energy (ion velocity distribution).

6) the total energy initially borne by the electrons can be entirely accounted for by the difference in the absorption between the polarizations (ion and K_α measurements).

7) while both pulse contrast cases show similar absorption fraction, the high contrast interaction exhibits the ion energy ~10 times larger and the continuum radiation energy ~100 times smaller than the low contrast one.

These observations were interpreted by the physical picture of the ponderomotive acceleration of electrons due to the resonantly enhanced p-polarized laser electric field at the critical surface. The production of the large flux of the fast ion and the reduction of the continuum radiation are consistent with the monoenergetic feature of electron accelerated by the ponderomotive potential. Based on the interpretation, the laser field enhancement and the plasma density scale length were calculated from the ion measurements. The scale length was incorporated into solving Maxwell's equations and used to estimate the enhanced field with the plasma wave coupling model. The model calculation was found to be in good agreement with the experimental results.

The ponderomotive acceleration picture was examined against the cold plasma wave breaking model as a high energy electron production mechanism. The comparison was made on the maximum electric field each mechanism can sustain and the experimentally observed parameters were found to fall in the region where the ponderomotive acceleration dominate the process.

VI-2 Future investigation

The laser system used for the experiments has been up graded to be capable of delivering more energy and thus operating at higher on-target intensities. It has been already observed that as the p-polarized intensity exceeds 10^{15} W/cm^2, the growth of the fast ion peak saturates and the production of the super high energy (~250 keV) electron begins. Quantitative characterization on the electrons should be performed to clarify the relation between the two phenomena and the mechanisms of the process.

These high energy electrons could be the promising source of an ultra-short x-ray burst with a very small spatial dimension. In fact it has been reported that x-ray photons in MeV range are generated from a femtosecond laser irradiated plasma with the laser intensity of 10^{18} W/cm^2.[1] Development of such x-ray sources with a high conversion efficiency requires the understanding of the interaction mechanisms.

Particular caution has to be taken on the prepulse level so that it does not exceed the solid damage threshold when the intensity is orders of magnitude higher than present experiment. For instance, the pulse contrast has to be $>10^7$ when the main pulse intensity is 10^{18} W/cm^2.

REFERENCE

[1] J. D. Kmetec, C. L. Gordon, I. J. J. Macklin, B. E. Lemoff, G. S. Brown and S. E. Harris, "MeV x-ray generation with a femtosecond laser," Phys. Rev. Lett. **68**, 1527 (1992).